UCLA
UCLA Electronic Theses and Dissertations

Title
Wavelength Conversion through Plasmon-Coupled Surface States

Permalink
https://escholarship.org/uc/item/9dk3v54f

Author
Turan, Deniz

Publication Date
2021

Peer reviewed|Thesis/dissertation

eScholarship.org
Powered by the California Digital Library
University of California

UNIVERSITY OF CALIFORNIA
Los Angeles

Wavelength Conversion through Plasmon-Coupled Surface States

A dissertation submitted in partial satisfaction
of the requirements for the degree
Doctor of Philosophy in Electrical and Computer Engineering

by

Deniz Turan

2021

© Copyright by
Deniz Turan
2021

ABSTRACT OF THE DISSERTATION

Wavelength Conversion through Plasmon-Coupled Surface States

by Deniz Turan

Doctor of Philosophy in Electrical and Computer Engineering

University of California, Los Angeles, 2021

Professor Mona Jarrahi, Chair

Surface states generally degrade semiconductor device performance by raising the charge injection barrier height, introducing localized trap states, inducing surface leakage current, and altering the electric potential. Therefore, there has been an endless effort to use various surface passivation treatments to suppress the undesirable impacts of the surface states. During my doctoral studies, I have investigated the unique electrochemical characteristics of semiconductor surface states and showed that the giant built-in electric field created by the surface states can be harnessed to enable passive wavelength conversion with unprecedented efficiencies without utilizing any nonlinear optical phenomena. Photo-excited surface plasmons are coupled to the surface states to generate an electron gas, which is routed to a nanoantenna array through the giant electric field created by the surface states. The induced current on the nanoantennas, which contains mixing product of different optical frequency components, generates radiation at the beat frequencies of the incident photons. We utilize the unprecedented functionalities of plasmon-coupled surface states to demonstrate passive wavelength conversion of nano-joule optical pulses at a 1550 nm center wavelength to terahertz regime with record-high efficiencies that exceed nonlinear optical methods by 4-orders of magnitude. The presented scheme can be used for optical wavelength conversion to different parts of the electromagnetic spectrum ranging from microwave to far-infrared regimes by using appropriate optical beat frequencies.

The dissertation of Deniz Turan is approved.

Pietro Musumeci

Chee-Wei Wong

Benjamin S. Williams

Mona Jarrahi, Committee Chair

University of California, Los Angeles

2021

To my parents, Gursevil and Rasit Turan

To my wife, Eylul Simsek

Table of Contents

Chapter 1: Introduction 1

1.1. Terahertz Science and Technology 1

1.2. Time-Domain Terahertz Spectroscopy Systems 2

1.3. Optical-to-Terahertz Converters for THz-TDS Systems 3

1.3.1. Optical-to-Terahertz Conversion through Nonlinear Optical Processes 3

1.3.2. Optical-to-Terahertz Conversion through Photo-Dember Effect 4

1.3.3. Optical-to-Terahertz Conversion through Spintronics 5

1.3.4. Optical-to-Terahertz Conversion through Photoconduction 6

1.4. Femtosecond Lasers for THz-TDS Systems 9

1.5. Thesis Outline 10

Chapter 2: Wavelength Conversion Through Plasmon-Coupled Surface States 12

2.1. Introduction 12

2.2. Impact of InAs Epilayer Thickness 15

2.3. Nanoantenna Design 17

2.4. Results and Discussions 29

2.4.1. Terahertz Radiation Dependence to Optical Pump Power 29

2.4.2. Fiber-Coupled Optical-to-Terahertz Wavelength Converter 34

2.4.3. Optical Beam Size, Position, and Polarization Requirements 36

2.4.4. Continuous Wave Operation 37

2.4.5. Operation under Smaller Optical Pulsewidth 38

2.5. Methods 40

2.5.1. Semiconductor Growth 40

2.5.2. Device Fabrication 40

Chapter 3: Plasmonics-Enhanced Photoconductive Terahertz Detector Pumped by Ytterbium-Doped Fiber Laser 41

3.1. Introduction 41

3.2. Design and Fabrication 42

3.3. Experimental Results and Discussion 48

Chapter 4: Impact of Metal Adhesion Layers on the Performance of Plasmonic Photoconductive Terahertz Sources 55

4.1. Introduction 55

4.2. Device Design 56

4.3. Experimental Results and Discussion 61

Chapter 5: Conclusion 65

Bibliography 67

LIST OF TABLES AND FIGURES

Fig. 1.1: Schematic of a terahertz time-domain spectroscopy system 2

Fig. 1.2: Schematic of a photoconductive terahertz source. 6

Fig. 1.3: Schematic of a photoconductive terahertz detector. 7

Fig.1.4: Schematic of photoconductive terahertz sources utilizing (a) plasmonic contact electrodes, (b) plasmonic nanoantennas. 9

Fig. 2.1. a, Energy band diagram of a highly p-doped InAs substrate in contact with Ti/Au. The energy level at which the surface state density of InAs peaks is located above its direct bandgap because there is a large difference between the direct (0.36 eV) and indirect bandgap energies (1.21 eV) of InAs. Electrons in these surface states recombine with the holes in the valence band and occupy a part of the conduction band to minimize their total energy. As a result, the Fermi energy level (E_F) is pinned above the conduction band minimum (E_C). Free electrons in the conduction band then migrate to the p-doped InAs layer to minimize their energy further, resulting in a steep band bending and a giant built-in electric field induced at the InAs surface. **b,** Schematic of the InAs lattice in contact with a nanoantenna that couples photo-excited surface plasmons to the surface states……………………………………………………………………………..13

Fig. 2.2. Schematic of a nanoantenna array on an InAs semiconductor substrate, which is designed to couple photo-excited surface plasmons to the surface states where a built-in electric field drifts the photo-induced electron gas to the nanoantennas to generate radiation at the optical beat frequencies. The nanoantenna geometry and semiconductor structure are chosen to maximize the spatial overlap between the built-in electric field and photoabsorption profiles. 14

Fig. 2.3. a, Band diagram of the p-doped InAs layer below the Ti/Au nanoantenna contact at different p-type doping concentrations are shown in white. The color map shows the strength of the built-in electric field. Sentaurus device simulator is used to generate the band diagram and built-in electric field plots. The built-in electric field drifts the high-mobility photo-generated electrons to the Ti/Au contact without any barrier height and sweeps away the low-mobility photo-generated holes from the Ti/Au contact. **b**, The measured terahertz radiation spectra from identical nanoantenna arrays fabricated on three InAs substrates with p-type doping concentrations of 10^{17}, 10^{18}, and 10^{19} cm^{-3} in response to the same optical pump beam. The radiation spectra are shown in a linear scale to clearly show the wavelength conversion efficiency variations**.** **c**, Band diagram and the built-in electric field profiles when an undoped InAs layer is incorporated between the p-doped InAs epilayer and the Ti/Au contact. **d**, The measured terahertz radiation spectra from identical nanoantenna arrays fabricated on four InAs substrates with undoped InAs layer thicknesses of 0, 100, 200, and 350 nm grown on an InAs epilayer with a p-type doping of 10^{19} cm^{-3}. 16

Fig. 2.4. a, Surface plasmon dispersion curve and the momentum provided by nanoantennas with a periodicity of $\Lambda = 440$ nm. Optical absorption profile inside the InAs layer when a 1550 nm TM-polarized optical excitation is incident on the nanoantennas (inset). **b,** Surface plasmon dispersion curve and the momentum provided by nanoantennas with a periodicity of $\Lambda = 160$ nm. Optical absorption profile inside the InAs layer when a 1550 nm TM-polarized optical excitation is incident on the nanoantennas (inset). Optical transmission spectrum to the InAs layer, optical absorption spectrum within a 100 nm depth in the InAs layer, and the overlap integral calculated as a function of depth in the substrate for both nanoantenna designs are shown in **c**, **d**, and **e** respectively. All of the optical simulations are performed using a finite-difference time-domain solver (Lumerical)........ 18

Fig. 2.5: Coordinate axis orientation used in the theoretical analysis 19

Fig. 2.6. Optical pump terahertz probe measurement of the p-type InAs ($p = 10^{19}$ cm^{-3}) layer grown on a semi-insulating GaAs substrate. 21

Fig. 2.7 Impulse response current of the nanoantenna array and its Fourier transform amplitude are shown in **a** and **b**, respectively. 22

Fig. 2.8 a-f Top: The induced current on the nanoantennas as a function of frequency when the nanoantenna length (L_a) is varied from 1 μm to 9 μm. The ground line width (L_b) and the gap between the nanoantenna array rows (L_g) are chosen as 2 μm and 0.5 μm. The ground line is located between -2 μm and 0 positions and the nanoantenna is located between 0 and 1-9 μm positions along the z-axis. **a-f Bottom:** Decomposition of the total induced current on the nanoantennas (teal lines) to the individual contributions of the injected currents from different positions of the nanoantennas (white lines) at 0.2 THz. The background color maps show the electron generation profiles averaged over the nanoantenna width 23

Fig. 2.9 a, Top view and side view of the simulated nanoantenna array to investigate the induced current on each nanoantenna. The induced current on the shaded nanoantenna when **b,** the neighboring nanoantennas are not excited, **c,** the two neighboring nanoantennas are excited, and **d,** six neighboring nanoantennas are excited. 25

Fig. 2.10. a-c Top: The induced current on the nanoantennas as a function of frequency when the ground line width (L_b) is varied from 1 μm to 3 μm. The nanoantenna length (L_a) and the gap between the nanoantenna array rows (L_g) are chosen as 2 μm and 0.5 μm, respectively. The ground line junction with the nanoantenna is located at the 0 position and the nanoantenna is located between 0 and 2 μm positions along the z-axis. **d-f Top** The induced current on the nanoantennas as a function of frequency when the gap between the nanoantenna array rows (L_g) is varied from 0.5 μm to 3 μm. The nanoantenna length (L_a) and the ground line width (L_b) are chosen as 2 μm and 2 μm, respectively The ground line is located between -2 μm and 0 positions and the nanoantenna is located between 0 and 2 μm positions along the z-axis.**a-f Bottom**: Decomposition of the total induced current on the nanoantennas (teal lines) to the individual contributions of the injected currents from different positions of the nanoantennas (white lines) at 0.2 THz. The background color maps show the electron generation profiles averaged over the nanoantenna width. 26

Fig. 2.11. Predicted and measured terahertz radiation power from fabricated nanoantenna arrays with different nanoantenna lengths, ground line widths, and gaps sizes between the nanoantenna rows are shown in **a, b,** and **c** respectively. All the fabricated nanoantenna arrays have a 1×1 mm^2 area and are characterized using the same optical pulses with 120 fs pulse width, 2.63 nJ pulse energy, and 76 MHz repetition rate. 29

Fig. 2.12, a, The measured terahertz radiation spectrum (shown in red) along with the noise spectrum (shown in gray) when the nanoantenna array is excited by optical pulses with a 1550 nm center wavelength, 900 mW power, 120 fs pulsewidth, and 76 MHz repetition rate. 650 time-domain traces are captured and averaged to resolve this terahertz spectrum. Dependence of the radiation spectrum on the optical power level is shown in the inset.**b,**Measured terahertz pulse energy/power from the fabricated nanoantenna array as a function of the optical pulse energy/power (inset) in comparison with other passive optical-to-terahertz converters reported in the literature. 30

Fig. 2.13, Comparison of **a,** The radiated terahertz power as a function of optical power, **b,** The optical-to-terahertz conversion efficiency as a function of the bias voltage. between the fabricated passive nanoantenna array with the reported *active* optical-to-terahertz converters operating at 1550 nm wavelength. 32

Fig. 2.14. Measured terahertz power at different optical pump powers in quadratic regime and linear regime is shown in **a** and **b** respectively**,** Dashed lines show the calculated converted power. **c**, The calculated total radiated power, Pfdf, indicating a linear dependence on the optical power level beyond 50 mW, when the optical beam size incident on the nanoantennas is linearly increased as a function of the optical power level (inset). 33

Fig. 2.15, a, Photograph, microscopy, and scanning electron microscopy images of a fabricated nanoantenna array on a substrate consisting of a 100-nm-thick undoped InAs layer grown on a 500-nm-thick InAs epilayer with a p-type doping of 10^{19} cm^{-3} grown on a semi-insulating GaAs substrate. **b,** Measured terahertz radiation (in blue) and noise (in red) spectra generated from the nanoantenna array when pumped by 3.68 nanojoule optical pulses at a 1550 nm center wavelength. The time-domain radiated terahertz pulse is shown in the inset. 3200 time-domain traces are captured and averaged to resolve this spectrum. 35

Fig. 2.16, a, The measured terahertz radiation power from the nanoantenna array for different optical beam sizes and beam positions. **b,** The measured terahertz radiation power from the nanoantenna array as a function of optical polarization. 36

Fig. 2.17, a Top: Experimental setup used to measure CW radiation from the nanoantenna array. **a Bottom:** Measured IF signal for each optical beat frequency. **b,** The measured radiation power from the nanoantenna array over the 0.23-2.3 THz frequency range using a pyroelectric detector. 38

Fig. 2.18, The measured terahertz radiation spectrum (shown in blue) along with the noise spectrum (shown in gray) when the nanoantenna array is excited by optical pulses with a 1560 nm center wavelength, 100 mW power, and 23 fs pulsewidth. 1000 time-domain traces are captured and averaged to resolve this terahertz spectrum. Comparison between the calculated (red) and measured (blue) radiated field is shown in the inset. 39

Fig. 3.1: Schematic of the designed plasmonic photoconductive terahertz detector 38

Fig. 3.2: Optical absorption spectra inside the $In_{0.24}Ga_{0.76}As$ layer for the optimized nanoantenna geometries for different $In_{0.24}Ga_{0.76}As$ thicknesses (left) and the color plot of the optical absorption profile inside the $In_{0.24}Ga_{0.76}As$ layer at a 1.04 μm pump wavelength (right). Nanoantennas with a 225 nm width, 305 nm periodicity, and 3/77 nm Ti/Au thickness, covered with a 370-nm-thick Si_3N_4 anti-reflection coating are designed for the detector fabricated on the substrates with a 50 nm $In_{0.24}Ga_{0.76}As$ layer thicknesses. Nanoantennas with a 200 nm width, 280 nm periodicity, and 3/77 nm Ti/Au thickness, covered with a 380-nm-thick Si_3N_4 anti-reflection coating are designed for the detector fabricated on the substrates with a 200 nm $In_{0.24}Ga_{0.76}As$ layer thicknesses 40

Fig. 3.3: Color map of the optical absorption inside the $In_{0.24}Ga_{0.76}As$ layer at a 1.04 μm wavelength (top) and the optical absorption at a 1 nm depth below the surface of the substrate (bottom) plotted at a *yz*-cross section passing through the middle of a nanoantenna for different tip-to-tip gap sizes. 41

Fig. 3.4: (a) Color map of the electric field enhancement factor inside the $In_{0.24}Ga_{0.76}As$ layer at 1 THz (top) and the electric field enhancement factor at a 1 nm depth below the surface of the substrate (bottom) plotted at a *yz*-cross section passing through the middle of a nanoantenna for different tip-to-tip gap sizes. (b) The electric field enhancement factor in the middle of the nanoantenna tips at a 1 nm depth below the surface of the substrate as a function of frequency for different tip-to-tip gap sizes. 42

Fig. 3.5: (a) Photoluminescence measurements of a 200-nm-thick $In_{0.24}Ga_{0.76}As$ layer epitaxially grown on a 200-nm-thick AlAs layer on an SI-GaAs substrate. (b) Atomic force microscopy scan of the grown $In_{0.24}Ga_{0.76}As$/AlAs epilayer. (c) Microscopy image of the fabricated detector on this substrate and the scanning electron microscopy image of the plasmonic nanoantennas............. 43

Fig. 3.6: Measured electric field as a function of (a) the tip-to-tip gap size between the nanoantenna terminals, (b) the nanoantenna array size, (c) the $In_{0.24}Ga_{0.76}As$ layer thickness and their corresponding radiation spectra are shown in (d), (e), and (f), respectively. 45

Fig. 3.7: Measured electric field profiles and their corresponding radiation spectra at different optical pump powers for the detector fabricated on a 200-nm-thick $In_{0.24}Ga_{0.76}As$ layer with a 0.5 μm tip-to-tip gap size and a 0.5×0.5 mm^2 active area are shown in (a) and (b), respectively. Dependence of the peak time-domain electric field and the noise current level to the optical pump power is shown in (c). The red dotted line shows the square root of the optical pump power..... 46

Fig. 3.8: Impact of increasing number of averaged time-domain traces in the resolved radiation spectrum. Dashed lines indicate the noise level of the acquired spectrums with different number of traces.. 48

Fig. 4. 1: Comparison between the energy band diagram of an ideal metal–semiconductor Schottky junction (a) and a metal–semiconductor Schottky junction with interface states (b)……………52

Fig. 4.2: Schematic diagram of the large-area plasmonic photoconductive terahertz source architecture used in our study. 54

Fig. 4. 3: (a) Optical transmission spectra of the Ti/Au and Cr/Au plasmonic gratings. (b) Optical power lost within the Ti and Cr layers in both cases. (c) Absorbed optical power near the gratings for both grating metallization schemes. 55

Fig. 4.4: Scanning electron microscopy images of a fabricated plasmonic photoconductive sources. 56

Fig. 4.5: The measured photocurrent (a) and radiation power (b) of the fabricated plasmonic photoconductive sources with different Au adhesion layers under different optical pump powers. (c) The ratio between the terahertz radiation power of the plasmonic photoconductive sources with Cr/Au and Ti/Au contact electrodes. (d) The measured radiation spectra of the fabricated plasmonic photoconductive sources with different Au adhesion layers at an optical pump power of 200 mW. 57

Fig. 4.6: The measured terahertz radiation power of the Cr/Au plasmonic photoconductive source under different optical pump powers and bias voltages.. 58

ACKNOWLEDGEMENTS

First, I would like to thank my advisor, Prof. Mona Jarrahi, for her endless support, mentorship throughout my PhD. Her boundless optimism and energy will inspire me for the rest of my life. I will always admire her perseverance, resourcefulness, and patience in research and life.

Second, I would like to thank my PhD committee members Prof. Benjamin Williams, Prof. Chee Wei Wong, and Prof. Pietro Musumeci for their guidance during my PhD. I would also like to thank our collaborators, Prof. Jigang Wang, from Iowa State University for their support during the experiments we did at Iowa State University and Prof. Sascha Preu from Technical University Darmstadt for providing the terahertz detector that I used throughout my research.

I would also like to thank Dr. Nezih Tolga Yardimci for years of support, hours of discussions, and his friendship inside and outside of the laboratory. It is a privilege to work with him and get to know him. I cannot thank him enough. I would also like to thank all the former and current members of Terahertz Electronics Laboratory including, Shang-Hua Yang, Ning Wang, Ping-Keng Lu, Yen-Ju Lin, Semih Cakmakyapan, Xurong Li, Yifan Zhao, Joseph Hwang, and Ruixuan Zhao. Especially, I would like to thank Prof. Mehmet Unlu for his support during my application to UCLA.

I would like to thank my wife, Eylul Simsek for her unconditional support even when we were separated by continents. I would like to thank my brother Baris Turan for his support as well. Finally, I am eternally grateful to my parents Gursevil Turan and Rasit Turan for their decades-long support, help, and guidance. They have inspired me to pursue science and they will always be Nobel Laurates of my heart.

VITA

2009 – 2014	B.Sc. in Electrical and Electronics Engineering, Middle East Technical University, Ankara.
2010 – 2011	Education abroad student at the University of California – Los Angeles.
2014 – 2016	M.Sc. in Electrical Engineering, University of California – Los Angeles.
2014 – 2021	Graduate Student Research Assistant under Professor Mona Jarrahi, University of California – Los Angeles.

PUBLICATIONS

Journal Papers

- D. Turan, P. K. Lu, N. T. Yardimci, Z. Liu, L. Luo, J. M. Park, U. Nandi, J. Wang, S. Preu, M. Jarrahi, "Wavelength conversion through plasmon-coupled surface states," 2021 (Under review) (https://arxiv.org/ftp/arxiv/papers/2012/2012.03179.pdf).
- N. T. Yardimci**,** D. Turan, M. Jarrahi, "Extremely Efficient Photoconductive Terahertz Detection Realized by Plasmonic Nanocavities", 2021 (Under review).
- J. Wang, R. Kim, C. Huang, Y. Luan, L.L. Wang, Z. Liu, J-M. Park, L. Luo, Z. Fei, P. Lozano, G. Gu, D. Turan, N. T. Yardimci, M. Jarrahi, I. Peraskis, and Q. Li, "Terahertz Nano-Imaging of Electronic Strip Heterogeneity in a Dirac Semimetal", doi:10.1021/acsphotonics.1c00216, ACS Photonics, 2021.
- P.-K. Lu, D. Turan, and M. Jarrahi, "High-sensitivity telecommunication-compatible photoconductive terahertz detection through carrier transit time reduction," Opt. Express, 28, 26324-26335, 2020.

- D. Turan, N. T. Yardimci, and M. Jarrahi, "Plasmonics-enhanced photoconductive terahertz detector pumped by Ytterbium-doped fiber laser," Opt. Express 28, 3835-3845, 2020.
- N. T. Yardimci, D. Turan, S. Cakmakyapan, M. Jarrahi, “A high-responsivity and broadband photoconductive terahertz detector based on a plasmonic nanocavity”, Appl. Phys. Lett., 113, 251102, 2018.
- D. Turan, S. C. C. Garcia, E. Castro-Camus, M. Jarrahi, "Impact of the Metal Adhesion Layer on the Radiation Power of Plasmonic Photoconductive Terahertz Emitters", Journal of Infrared, Millimeter and Terahertz Waves, 38, 2017.

Chapter 1: Introduction

1.1. Terahertz Science and Technology

Terahertz waves are loosely defined as electromagnetic radiation with frequencies between 0.1 THz and 10 THz. Because of the challenges in the generation and detection of terahertz waves [1], this portion of the electromagnetic spectrum is also called the "Terahertz Gap". This so called terahertz gap has started to narrow down in recent years thanks to numerous scientific breakthroughs.

Terahertz science has been an active research area for the last 30 years because of the unique applications of terahertz radiation for basic science as well as imaging, sensing, and communication. Since many optically opaque materials are more transparent to terahertz waves, imaging inside visually inaccessible environments can be enabled by terahertz waves [2], [3]. Additionally, since many molecules have unique spectral signatures at terahertz frequencies, standoff identification of many unknown substances such as illicit drugs and explosives can be enabled by terahertz waves [4], [5], [6], [7]. Furthermore, terahertz waves are non-ionizing and non-destructive to human tissue and, therefore, can be used for medical imaging to detect skin, colon, and breast cancer tumors [8], [9]. In a more fundamental scientific setting, terahertz waves can be used for studying ultrafast dynamics of complex materials [10]**.** Also, the detection of faint terahertz radiation from distant corners of the universe can provide crucial information for many astrophysical studies [11], [12].

Despite many advances in the terahertz field, the use of terahertz waves is still mostly limited to research laboratories due to the lack of high-performance terahertz sources and detectors.

Therefore, the quest to build more efficient, high-power terahertz sources and more sensitive terahertz detectors is still ongoing.

1.2. Time-Domain Terahertz Spectroscopy Systems

One of the major breakthroughs in the terahertz technology has been the invention of Time-Domain Terahertz Spectroscopy (THz-TDS) systems by David Auston at Bell Laboratories and Dan Grischowski at IBM [13], [14]. THz-TDS systems have expanded the accessibility of the terahertz technology by researchers and enabled the demonstration of many different applications of terahertz waves.

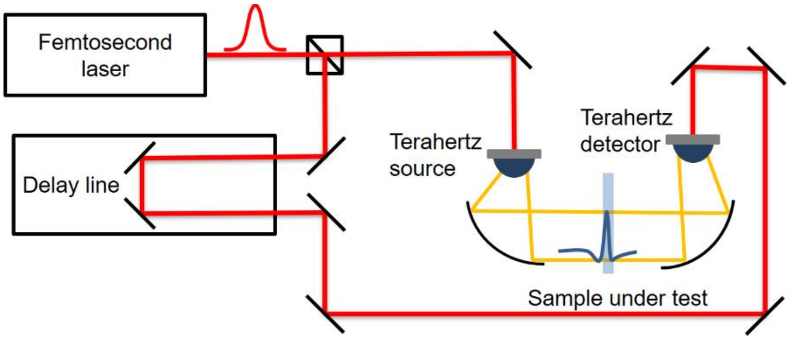

Fig. 1.1: Schematic of a terahertz time-domain spectroscopy system

Figure 1.1 shows the schematic of a typical THz-TDS system empowered by a femtosecond laser. The femtosecond laser pulse is first split into two beams to pump a terahertz source and probe a terahertz detector. The terahertz source excited by the pump beam converts the optical pulse to a terahertz pulse. The terahertz pulse interacts with any object placed along its propagation direction before arriving at the terahertz detector, which samples the incident terahertz field when probed by the femtosecond optical pulse. In order to capture a time-domain scan of the terahertz pulse, a time-delay is introduced between the pump and probe beams. This time delay is generally introduced by a mechanical delay stage with a limited data acquisition speed. However, more sophisticated sampling methods such as asynchronous optical sampling (ASOPS) [15] and electronically controlled optical sampling (ECOPS) [16] can be used to increase the data acquisition speed.

Since the terahertz electric field is detected in THz-TDS systems instead of power, both amplitude and phase information of the terahertz electric field is preserved. This enables extracting both refractive index and absorption coefficient of the materials under test simultaneously. Furthermore, the interaction of the terahertz pulses with multi-layered objects creates pulse echoes, revealing characteristics of each layer separately. Also, the time-delay of each pulse relative to the others enables the extraction of the thickness of each layer, making THz-TDS systems promising candidates for 3D imaging [17].

1.3. Optical-to-Terahertz Converters for THz-TDS Systems

THz-TDS systems require a source to convert femtosecond optical pulses to sub-picosecod terahertz pulsse. There are four common ways to realize optical-to-terahertz conversion in THz-TDS systems through nonlinear optical processes, spintronics, photo-Dember effect, and photoconduction. Details of these methods are discussed in the following sections.

1.3.1. Optical-to-Terahertz Conversion through Nonlinear Optical Processes

When a femtosecond laser pulse is incident on a crystal that exhibits optical nonlinearity, a terahertz pulse can be generated by the difference-frequency generation process of multiple wavelength components within the optical pulse. This optical-to-terahertz conversion method, known as optical rectification, is better suited for generating terahertz pulses with high peak electric fields (~MV/cm) under high-energy optical pulse energies. Lithium Niobate and Zinc Telluride are common nonlinear crystals used for optical rectification, thanks to their high nonlinear optical susceptibility, high damage threshold, and low terahertz loss [18], [19]. Organic nonlinear crystals with higher second-order nonlinear susceptibility such as DAST [20], and OH1 [21] have also been introduced recently for more efficient optical-to-terahertz conversion.

Optical-to-terahertz conversion through nonlinear optical processes is inherently inefficient due to the Manley-Rowe limit and the difficulty in matching the phases of the optical and terahertz waves inside nonlinear crystals. Guided wave nonlinear media, quasi phase matching in periodically poled media, and the use of tilted-wavefront pump waves have been employed to offer better phase-matching control resulting in longer field interaction lengths [18], [19]. However, because of the material absorption, the active length in which terahertz waves are generated is limited to centimeter-ranges. Because of the field interaction length limitations, the use of high-power optical pumps has been necessary to provide ultra-high peak power levels for generating meaningful terahertz powers.

1.3.2. Optical-to-Terahertz Conversion through Photo-Dember Effect

When a photo-absorbing semiconductor is illuminated with a femtosecond optical pulse, the photogenerated electrons and holes diffuse from the semiconductor surface toward the bulk due to the presence of a concentration gradient. Electrons and holes diffuse with different rates within the semiconductor due to the difference between their mobilities and start to separate from each other as they move. As a result, a time-varying dipole inside the semiconductor is formed and terahertz radiation is generated through this so called photo-Dember effect. InAs and InSb are the preferred semiconductors for optical-to-terahertz converters based on the photo-Dember effect due to the large difference between their electron and hole mobilities [22], [23].

When the femtosecond laser pulse is incident on the semiconductor perpendicularly, the terahertz radiation generated as a result of the photo-Dember effect propagates parallel to the semiconductor. Therefore, only a small fraction of the generated terahertz radiation can be coupled out of the device, reducing the optical to terahertz conversion efficiency significantly [24]. Therefore, the photo-Dember optical-to-terahertz converters are usually excited with femtosecond laser pulses incident with an oblique angle, which increases the complexity of terahertz systems [22], [23], [25], [26]. To address this limitation lateral photo-Dember sources are introduced that can generate time-varying dipoles parallel to the semiconductor surface. However, the reported optical-to-terahertz conversion efficiencies of these sources are still low because the utilized metal layers shadows a significant portion of the incident optical pulse [27].

1.3.3. Optical-to-Terahertz Conversion through Spintronics

A spintronic terahertz source consists of a stack of ferromagnetic and nonferromagnetic thin films. When a femtosecond laser pulse excites the material, a spin current is injected from the ferromagnetic layer to the nonferromagnetic layer. After arrival to the nonferromagnetic layer, this spin current density is transferred to a charge current density due to the inverse spin Hall effect, generating terahertz radiation [28], [29].

Spintronic sources reported so far show limited optical-to-terahertz conversion efficiencies possibly due to the lack of efficient optical coupling from free space to the ferromagnet [30], [31]. Furthermore, spintronic emitters require permanent magnets to operate, which introduces further complexity to the terahertz systems.

1.3.4. Optical-to-Terahertz Conversion through Photoconduction

A conventional photoconductive terahertz source consists of an antenna fabricated on a photoconductive material (Fig. 1.2). When a femtosecond optical pulse is incident on the photoconductor, photo-generated carriers are swept to the antenna contacts by a bias electric field applied across the antenna terminals. The carriers that arrive at the antenna contacts feed the antenna with an ultrafast current that generates terahertz radiation. Photoconductive terahertz sources are the preferred optical-to-terahertz converters in compact THz-TDS systems with lower pulse energies because they offer higher optical-to-terahertz conversion efficiencies when compared with nonlinear optical processes, photo-Dember effect, and spintronics.

Yet the efficiency of photoconductive terahertz sources is still low. This is because the photo-generated carriers must reach the antenna contacts within a fraction of a terahertz oscillation cycle (a sub-picosecond time scale) to efficiently contribute to the generation of a terahertz-radiating ultrafast current. In a conventional photoconductive terahertz source, only a fraction of the photo-generated carriers arrive at the antenna contacts within a sub-picosecond time scale because of the long carrier transit times. These ‘late carriers’ do not contribute to the terahertz generation process. Instead, they increase the total device current, which introduces an additional thermal load, degrades the device reliability, and screens the bias electric field inside the photoconductor.

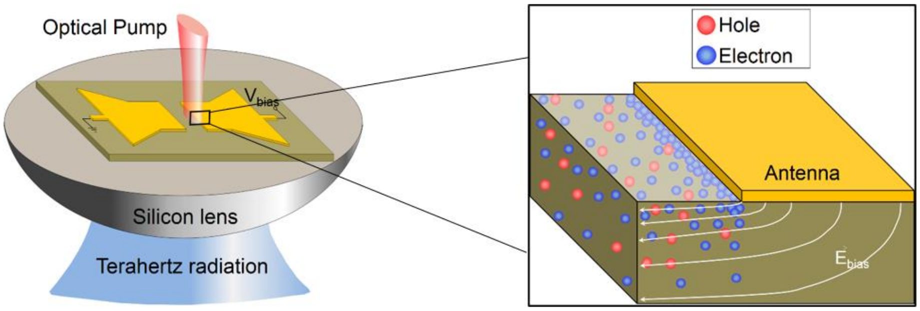

Fig. 1.2: Schematic of a photoconductive terahertz source.

Photoconductive antennas can be also used to detect terahertz radiation in THz-TDS systems (Fig. 1.3). In detection mode, photocarriers generated by the femtosecond laser pulse are drifted toward the antenna contacts by the incident terahertz electric field. When the carriers arrive at the antenna contacts, they induce a photocurrent proportional to the incident terahertz electric field.

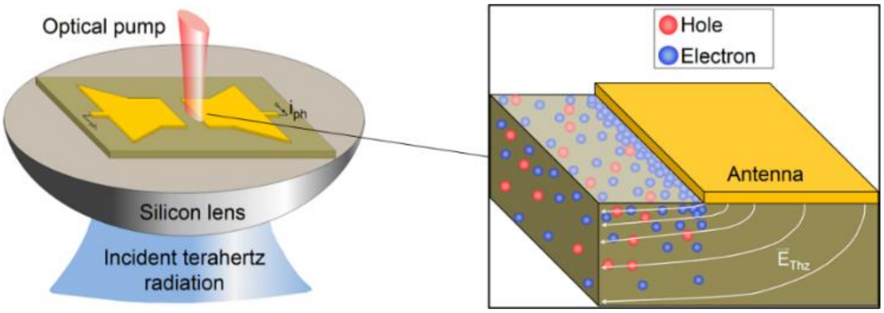

Fig. 1.3: Schematic of a photoconductive terahertz detector.

Photoconductive detectors should have a sub-picosecond response time in order to detect terahertz radiation with a high signal-to-noise ratio (SNR) [32], [33]. To provide the required sub-picosecond response time, conventional photoconductive terahertz detectors utilize short-carrier-lifetime semiconductors with a high concentration of defects. The defects in the semiconductor lattice are introduced through semiconductor growth at low temperatures [34]–[39], incorporating rare-earth elements during the semiconductor growth [40]–[42], or high-energy ion implantation [43], [44]. The introduced defects in the semiconductor lattice enable ultrafast operation by recombining the photocarriers that cannot drift to the antenna terminals in a sub-picosecond time scale. However, the responsivity of the photoconductive detectors based on short-carrier-lifetime semiconductors is limited since most of the photo-generated carriers get recombined in the substrate before reaching the antenna terminals. Moreover, the introduced defects reduce the carrier mobility and drift velocity significantly, which further reduces the number of the photocarriers that reach the antenna terminals in a sub-picosecond timescale. In addition, short-carrier-lifetime substrates are often not scalable to many photoconductive semiconductors, limiting the types of semiconductors and pump lasers that can be used for developing photoconductive terahertz detectors.

Quantum efficiency of photoconductive terahertz sources and detectors can be significantly enhanced by incorporating contact electrode structures that excite surface plasmon waves along the metal photoconductor interface [45]–[50]. Plasmonic structures can either be connected to the terahertz antenna as the contact electrodes (Fig. 1.4a) [46], [47], [51] or serve as the terahertz nanoantennas of the photoconductive terahertz source (Fig. 1.4b) [49], [50]. The periodicity of plasmonic structures is chosen to provide the necessary momentum to excite surface plasmon waves at the semiconductor-metal interface. As surface plasmon waves are tightly confined to the metal-semiconductor interface, the photocarrier generation occurs very close to the antenna contacts. As a result, a significantly higher fraction of the photo-generated carriers arrive at the antenna contacts in a sub-picosecond time scale to contribute to terahertz generation and detection. By utilizing plasmonic contact electrodes, radiation power enhancements over 3 orders of magnitude have been demonstrated compared to conventional photoconductive terahertz sources [44], [45].

After the seminal work published in 2013 by Berry et. al. [47], there has been numerous additional demonstrations on the effectiveness of plasmonic contact electrodes for improving the radiation performance of the photoconductive terahertz sources and detection sensitivity of photoconductive terahertz detectors [47], [52]. Record-high optical-to-terahertz conversion efficiencies up to 7.5% [46] and record-high radiation powers up to 3.8 mW [50] have been demonstrated with photoconductive sources that incorporate plasmonic structures. Furthermore, the use of plasmonic contact electrodes can eliminate the need for short-carrier-lifetime

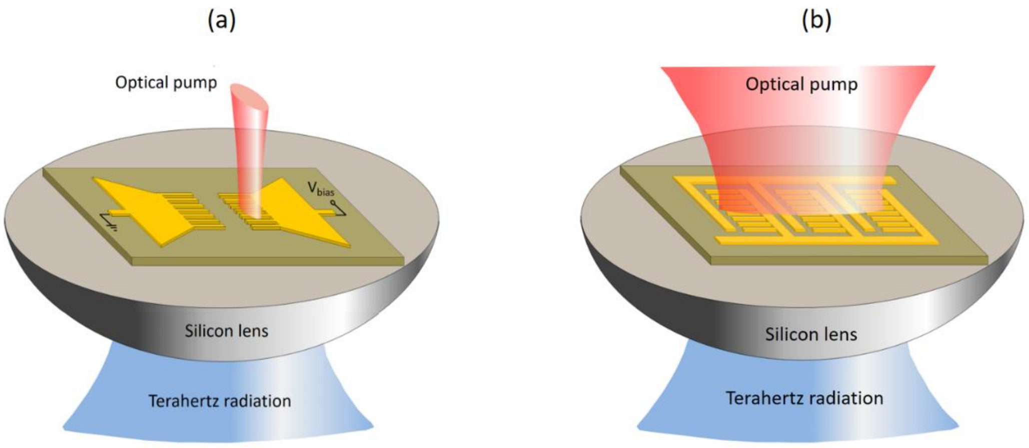

Fig. 1.4: Schematic of photoconductive terahertz sources utilizing (a) plasmonic contact electrodes, (b) plasmonic nanoantennas.

semiconductors by significantly reducing the photocarrier transit time to the antenna contacts, expanding the potential use of new materials and lasers for developing photoconductive terahertz sources and detectors [53].

1.4. Femtosecond Lasers for THz-TDS Systems

Ti-Sapphire mode-locked lasers became available in the 1990s and emerged as very popular pulsed laser sources thanks to their ease of operation and stable output powers. Despite their advantages, Ti-Sapphire lasers are very bulky, therefore, they are not suitable for commercial applications where compactness and portability are essential. Compact Er-doped fiber laser sources operating at telecommunication optical wavelengths (~1550 nm) offer an alternative to achieve compact THz-TDS systems. Therefore, there has been considerable effort to develop high-performance optical-to-terahertz converters and terahertz detectors compatible with telecommunication optical wavelengths [3], [42], [54], [55].

The optical-to-terahertz conversion efficiency of nonlinear optical processes drops significantly at pulse energies that can be provided by Er-doped fiber lasers (~nJ). Therefore, photoconductive terahertz sources are the preferred optical-to-terahertz converters for THz-TDS systems that work with telecommunication lasers. However, performance of previously demonstrated photoconductive terahertz sources operating at telecommunication wavelengths has been limited by low resistivity of photo-absorbing semiconductor substrates at these wavelengths (e.g. InGaAs). This is because efficient operation of photoconductive terahertz emitters requires accelerating photo-generated carriers by high bias electric fields, which results in high dark currents and thermal breakdown when using low resistivity substrates.

Various semiconductor structures such as ErAs:In(Al)GaAs [54], [56], InAlAs/InGaAs superlattices [57], and Fe-doped InGaAs [55] have been developed to improve the performance and reliability of the photoconductive terahertz sources at telecommunication optical wavelengths. These materials offer short carrier lifetimes and high resistivities to suppress the unwanted photocurrent and dark current, respectively. However, they reduce the carrier mobility and device quantum efficiency, consequently. Furthermore, photoconductive devices fabricated on some of these substrates require high bias voltages (~100-200V) to generate high terahertz radiation powers [43], [54], [55], [57]–[60].

1.5. Thesis Outline

In this dissertation, the use of plasmonic nanostructures in photoconductive terahertz devices is extended to provide unprecedented functionalities at terahertz frequencies. First, a passive optical-to-terahertz conversion scheme is demonstrated by exciting plasmon-coupled surface states in Chapter 2. This passive optical-to-terahertz converter is specifically designed to operate at telecommunication optical wavelengths, offering a highly reliable operation by eliminating the background device current. Moreover, the presented passive optical-to-terahertz conversion scheme offers orders of magnitude higher conversion efficiencies compared to other passive optical-to-terahertz converters operating with femtosecond fiber lasers.

Next, a high-sensitivity broadband photoconductive terahertz detector operating at ~1 μm optical pump wavelength range is demonstrated in Chapter 3. Parts of this chapter appeared in Optics Express [61]. The impact of the metal adhesion layer on terahertz generation performance of plasmonic photoconductive terahertz sources is investigated in Chapter 4. Parts of this chapter are published in the Journal of Infrared Millimeter and Terahertz Waves [62]. Chapter 5 of the dissertation includes a summary and conclusion of the thesis along with the future work.

Chapter 2: Wavelength Conversion Through Plasmon-Coupled Surface States

2.1. Introduction

When a semiconductor lattice is terminated on the surface, the periodicity of the lattice is broken since the surface atoms do not have sufficient number of atoms that they can bond to, leaving behind incomplete chemical bonds. These so called dangling bonds produce localized surface states with energy levels that are located within the bandgap of the semiconductor [63]–[66]. The Fermi energy level at the surface of a semiconductor is pinned to the energy level at which the surface state density peaks, while the Fermi energy level away from the semiconductor surface is determined by the semiconductor doping. Therefore, the presence of the surface states takes away a very important degree of freedom for engineering semiconductor devices by altering the electric potential profile and is generally a major source of degradation in semiconductor devices.

Despite the endless efforts to suppress the surface semiconductor states, they have unique electrochemical properties that are not provided by bulk semiconductors and could enable unprecedented device functionalities. Figure 2.1 illustrates how the presence of surface states induces a giant built-in electric field at the surface of a p-doped InAs semiconductor, which exceeds the breakdown field of bulk InAs. The energy level at which the surface state density of InAs peaks is located above its direct bandgap because there is a large difference between the direct and indirect bandgap energies of InAs [64], [65]. Since the electrons that occupy the surface states have an average total energy higher than the bulk InAs, they migrate from the surface states to the bulk InAs to reach equilibrium, leaving behind immobile charge of uncompensated donor ions, which produces a giant built-in electric field. Ideally, wavelength conversion can be achieved by accelerating photoabsorbed charges through this giant built-in electric field with very high mobility. However, efficient wavelength conversion was not possible before due to the very shallow band bending at the surface of the semiconductor, which severely limits the interaction between the giant built-in electric field and optical beam. Instead, photo-Dember effect and nonlinear optical processes were the dominant mechanisms for passive wavelength conversion [23], [67]–[69].

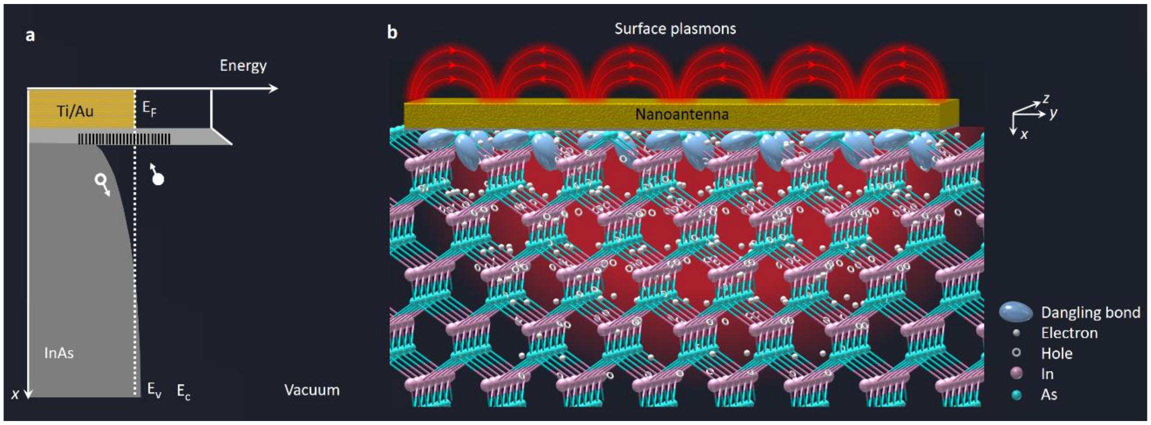

Fig. 2.1. a, Energy band diagram of a highly p-doped InAs substrate in contact with Ti/Au. The energy level at which the surface state density of InAs peaks is located above its direct bandgap because there is a large difference between the direct (0.36 eV) and indirect bandgap energies (1.21 eV) of InAs. Electrons in these surface states recombine with the holes in the valence band and occupy a part of the conduction band to minimize their total energy. As a result, the Fermi energy level (E_F) is pinned above the conduction band minimum (E_C). Free electrons in the conduction band then migrate to the p-doped InAs layer to minimize their energy further, resulting in a steep band bending and a giant built-in electric field induced at the InAs surface. **b,** Schematic of the InAs lattice in contact with a nanoantenna that couples photo-excited surface plasmons to the surface states.

To effectively utilize this built-in electric field for optical wavelength conversion, optical photons excite a nanoantenna array to couple photo-excited surface plasmons to the surface states (Fig. 2.1b). Excitation of surface plasmons enhances the optical intensity and photoabsorption near the InAs surface [11], [45], [61]–[80], where the strength of the built-in electric field is maximized.

The absorbed photons generate a tightly confined electron gas under the nanoantenna contacts with an electron concentration that resonates at the mixing product of different optical frequency components. This electron gas swiftly drifts to the nanoantennas through the built-in electric field. The induced current on the nanoantennas generates radiation at the beat frequencies of the optical photons

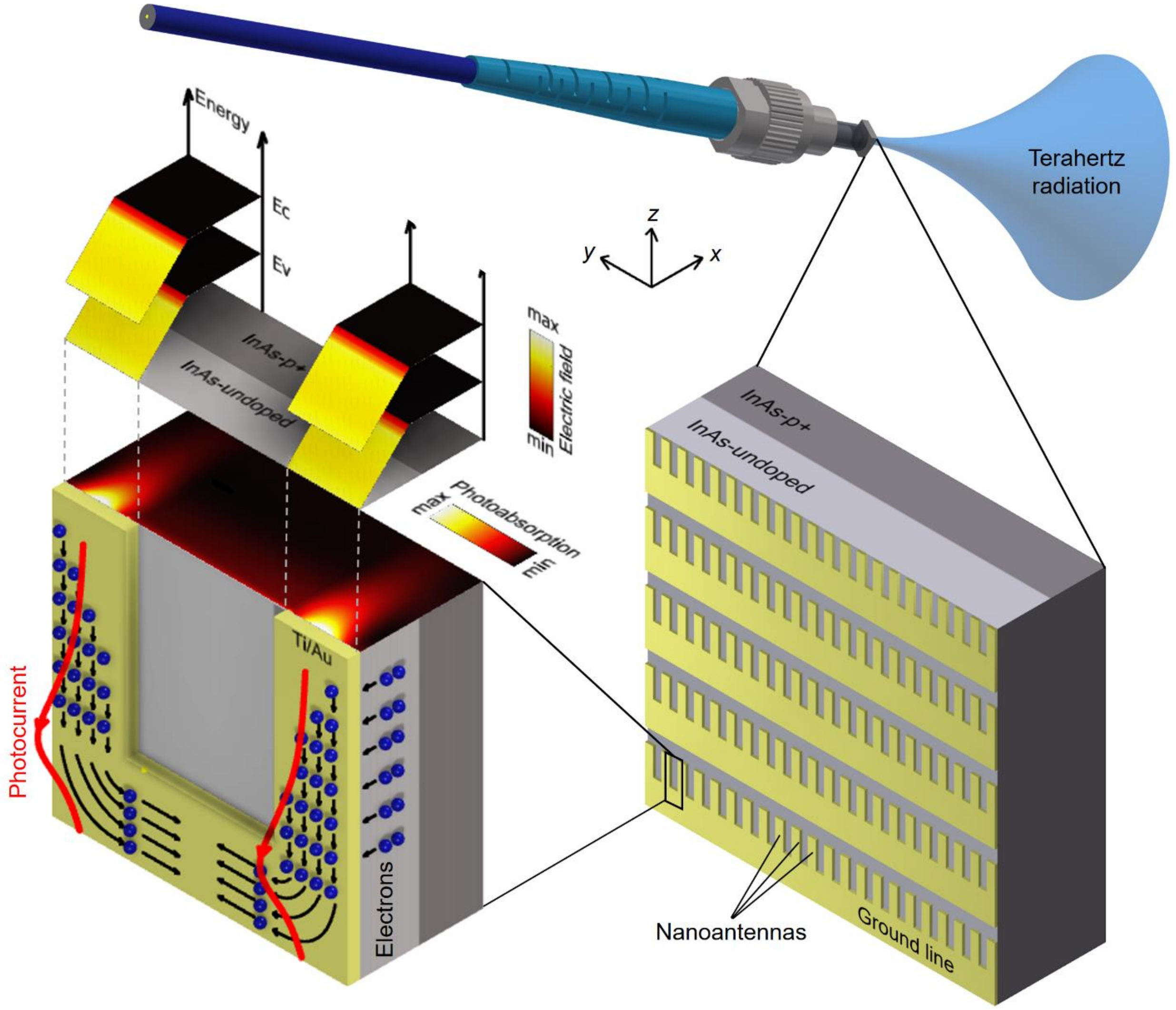
Energy
Ec
Ev
InAs-p+
InAs-undoped
max
min
Electric field
max
Photoabsorption
min
Ti/Au
Photocurrent
Electrons
z
y
x
Terahertz
radiation
InAs-p+
InAs-undoped
Nanoantennas
Ground line

Fig. 2.2. Schematic of a nanoantenna array on an InAs semiconductor substrate, which is designed to couple photo-excited surface plasmons to the surface states where a built-in electric field drifts the photo-induced electron gas to the nanoantennas to generate radiation at the optical beat frequencies. The nanoantenna geometry and semiconductor structure are chosen to maximize the spatial overlap between the built-in electric field and photoabsorption profiles.

Figure 2.2a shows a nanoantenna array designed to couple photo-excited surface plasmons to the InAs surface states where a built-in electric field drifts the photo-induced electron gas to the nanoantennas to generate radiation at the optical beat frequencies. Unlike the bulky and complex nonlinear optical setups that require high-energy lasers, tight optical focus, and/or tilted beam to provide high optical pump intensity and phase matching for efficient wavelength conversion, wavelength conversion through plasmon-coupled surface states does not require a complex optical setup and is not sensitive to optical focus and alignment.

2.2. Impact of InAs Epilayer Thickness

In order to achieve high wavelength conversion efficiencies, the semiconductor structure and nanoantenna geometry are chosen to maximize the spatial overlap between the built-in electric field and photoabsorption profiles. The strength and extent of the built-in electric field below the InAs surface can be controlled by the doping profile of the InAs substrate. As illustrated in Fig. 2.3a, since the Fermi energy level at the surface of InAs is pinned above the conduction band minimum, increasing the p-type doping of the bulk results in a steeper band bending and, therefore, a stronger built-in electric field near the InAs surface. To better show the impact of the substrate doping, identical nanoantenna arrays are fabricated on three InAs substrates with p-type doping concentrations of 10^{17}, 10^{18}, and 10^{19} cm^{-3} and their optical-to-terahertz conversion performance is characterized under the same optical pump beam. As predicted by the energy band diagrams illustrated in Fig. 2.3a, the nanoantenna array fabricated on the InAs substrate with a p-type doping concentration of 10^{19} cm^{-3} offers the highest wavelength conversion efficiency among the three as it benefits from the highest built-in electric field near the InAs surface (Fig. 2.3b).

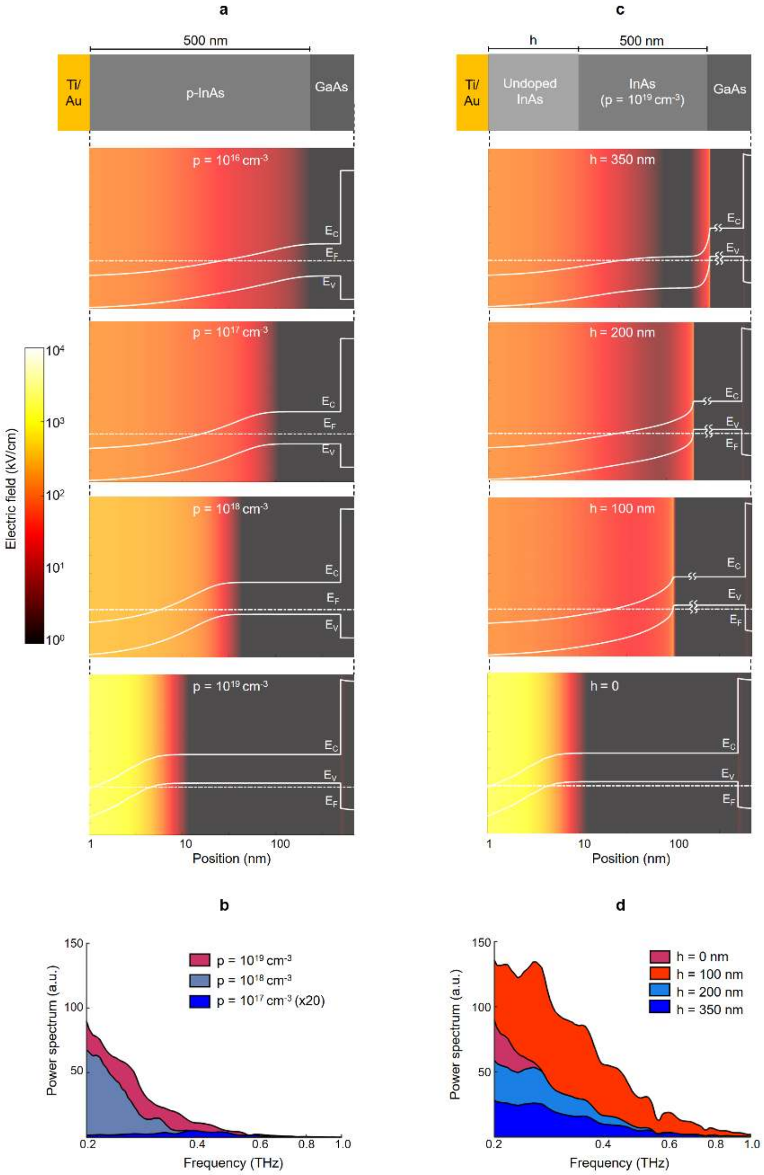

Fig. 2.3. a, Band diagram of the p-doped InAs layer below the Ti/Au nanoantenna contact at different p-type doping concentrations are shown in white. The color map shows the strength of the built-in electric field. Sentaurus device simulator is used to generate the band diagram and built-in electric field plots. The built-in electric field drifts the high-mobility photo-generated electrons to the Ti/Au contact without any barrier height and sweeps away the low-mobility photo-generated holes from the Ti/Au contact. **b**, The measured terahertz radiation spectra from identical nanoantenna arrays fabricated on three InAs substrates with p-type doping concentrations of 10^{17}, 10^{18}, and 10^{19} cm^{-3} in response to the same optical pump beam. The radiation spectra are shown in a linear scale to clearly show the wavelength conversion efficiency variations**. c**, Band diagram and the built-in electric field profiles when an undoped InAs layer is incorporated between the p-doped InAs epilayer and the Ti/Au contact. **d**, The measured terahertz radiation spectra from identical nanoantenna arrays fabricated on four InAs substrates with undoped InAs layer thicknesses of 0, 100, 200, and 350 nm grown on an InAs epilayer with a p-type doping of 10^{19} cm^{-3}.

However, increasing the p-type doping reduces the extent of the built-in electric field below the InAs surface and lowers the spatial overlap between the built-in electric field and photoabsorption profiles. One way to extend the built-in electric field below the InAs surface is incorporating an undoped InAs layer between the p-doped InAs epilayer and the nanoantenna contact. As illustrated in Fig. 2.3c, increasing the thickness of the undoped InAs layer further extends the band bending below the InAs surface while reducing the band bending slope, indicating a tradeoff between the strength and extent of the built-in electric field in the substrate. To better show the impact of this tradeoff, identical nanoantenna arrays are fabricated on four InAs substrates with undoped InAs layer thicknesses of 0, 100, 200, and 350 nm grown on an InAs epilayer with a p-type doping of 10^{19} cm^{-3} and their optical-to-terahertz conversion performance is characterized under the same optical pump beam. As demonstrated in Fig. 2.3d, the use of a 100-nm-thick undoped InAs layer increases the wavelength conversion efficiency by extending the built-in electric field in the semiconductor and increasing its spatial overlap with the photoabsorption profile. However, further increase in the thickness of the undoped InAs layer lowers the wavelength conversion efficiency due to the reduction in the built-in electric field strength. Because of its high wavelength conversion efficiency, the nanoantenna array fabricated on a 100-nm-thick undoped InAs layer grown on an InAs epilayer with a p-type doping of 10^{19} cm^{-3} is used in subsequent analysis

2.3. Nanoantenna Design

Periodicity of the nanoantennas in the y-direction is chosen as 440 nm to provide the necessary momentum to couple the photo-excited surface plasmon waves to the interface between the nanoantennas and the InAs substrate when excited by a TM-polarized optical beam at a 1550 nm wavelength (Fig. 2.4a). A 240-nm-thick Si_3N_4 anti-reflection coating, a 360-nm-thick nanoantenna width, and a 3/97-nm-thick Ti/Au nanoantenna height are used to increase the coupling efficiency of surface plasmon waves. To illustrate the impact of the excited surface plasmon waves, an alternative nanoantenna geometry is analyzed, which has a periodicity of 160 nm in the y-direction. The momentum provided by this periodicity is larger than the momentum required for the excitation of surface plasmon waves (Fig. 2.4b). Although the optical transmission to the InAs layer provided by this nanoantenna (Fig. 2.4c) is much higher than that of the plasmonic nanoantenna, the plasmonic nanoantenna provides 7 times higher optical absorption within a 100 nm depth inside the InAs layer, where the built-in electric field strength is maximized (Fig. 2.4d).

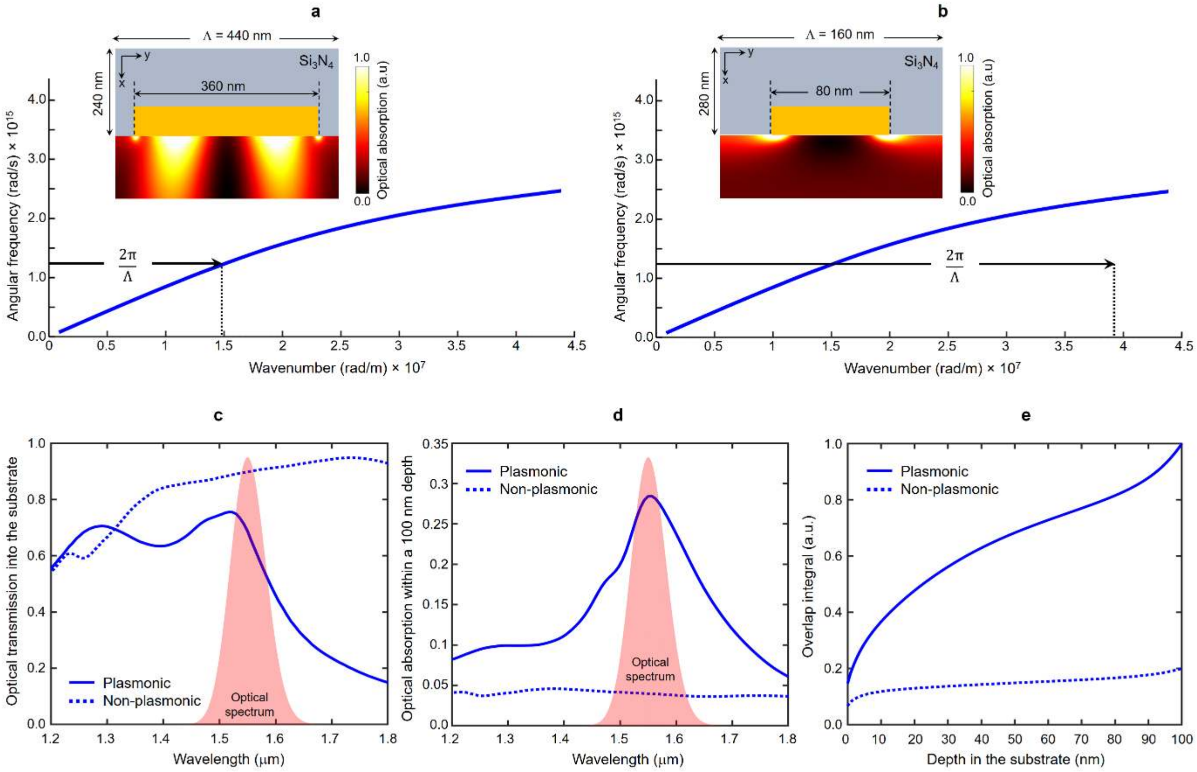

Fig. 2.4. a, Surface plasmon dispersion curve and the momentum provided by nanoantennas with a periodicity of Λ = 440 nm. Optical absorption profile inside the InAs layer when a 1550 nm TM-polarized optical excitation is incident on the nanoantennas (inset). **b,** Surface plasmon dispersion curve and the momentum provided by nanoantennas with a periodicity of Λ = 160 nm. Optical absorption profile inside the InAs layer when a 1550 nm TM-polarized optical excitation is incident on the nanoantennas (inset). Optical transmission spectrum to the InAs layer, optical absorption spectrum within a 100 nm depth in the InAs layer, and the overlap integral calculated as a function of depth in the substrate for both nanoantenna designs are shown in **c**, **d**, and **e** respectively. All of the optical simulations are performed using a finite-difference time-domain solver (Lumerical).

To quantify the overlap between the optical absorption and built-in electric field, an overlap integral function, $\mathrm{OI(x)}$, is defined as:

$$\mathrm{OI(x)} = \frac{\int_0^{x}\int_0^{w_a} E_{bi}(y',x') I_{abs}(x',y') dy' dx'}{\int_0^{\Lambda} I_{in}(y') dy'} \tag{1}$$

where E_{bi} is the built-in electric field shown in Fig. 2e color plots, I_{abs} is the absorbed optical beam intensity at a 1550 nm wavelength (Figs. 2.4a and b insets), I_{in} is the incident optical beam intensity on the nanoantenna array, and x is the depth in the InAs substrate. As expected, the calculated overlap integral values shown in Fig. 2.4e, are consistently higher for the nanoantenna design that supports surface plasmon waves.

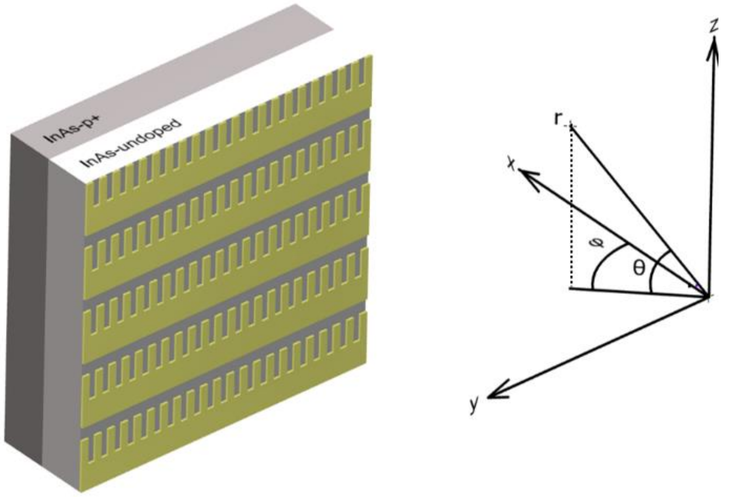

Fig. 2.5: Coordinate axis orientation used in the theoretical analysis

Geometry of the nanoantenna array in z direction is chosen to provide high-efficiency radiation over a broad terahertz frequency range when fed with the injected electrons from the InAs substrate. A three-dimensional optical simulation is first performed using a finite-difference time-domain solver (Lumerical) on one nanoantenna unit cell under a TM-polarized 1550 nm optical excitation and the carrier generation profile, $\mathrm{G(x, y, z)}$, is obtained from this simulation. Next, the continuity equation is solved for electron density, $n(x,y,z,t)$, under an impulse optical generation rate $G \cdot \delta(t)$:

$$\frac{\partial n}{\partial t} = \frac{1}{q}\nabla \cdot \vec{J}_n + G \cdot \delta(t) - \frac{n}{\tau} \tag{2}$$

where $\vec{J}_n$ is the electron current density in A/m^2, $\delta(t)$ is the Dirac-delta function, τ is the electron lifetime in seconds, and q is the electron charge in C. Next, Eq (2) is solved for both undoped InAs and p-type doped InAs regions. Following assumptions are made for electron transport in the undoped InAs region:

1. Electron current is dominated by the drift current in the x-direction.
2. Electrons are assumed to drift at the saturation velocity, i.e., $\vec{J}_n = q\vec{v}_e n$, $|v_e| = 10^5\ m/s$ [81], [82].
3. Since the carrier lifetime of the undoped InAs layer is much larger than the transit time of the photo-generated carriers inside the undoped InAs region that drift to the nanoantenna contact (~1 ps), a carrier lifetime of $\tau \to \infty$ is assumed in the undoped InAs region.

Under these assumptions, Equation (2) in the undoped InAs region is modified to:

$$\frac{\partial n}{\partial t} = v_e \frac{\partial n}{\partial x} + G \cdot \delta(t) \tag{3}$$

Following assumptions are made for electron transport in the p-doped InAs region:

1. Electron current is dominated by the diffusion current in the x-direction, i.e., $J_{n,x} = qD_n \frac{\partial n}{\partial x}$.

2. Diffusion constant of the p-type InAs layer is chosen as $D_n = 1.36 \times 10^{-4}\ m^2/s$, based on the experimental results reported in [83]. Brooks-Herring's model is used to account for the additional degradation in mobility due to the high doping density.
3. The carrier lifetime of the p-type InAs layer is chosen as 5 ps, based on the measurement results shown in Fig. 2.6

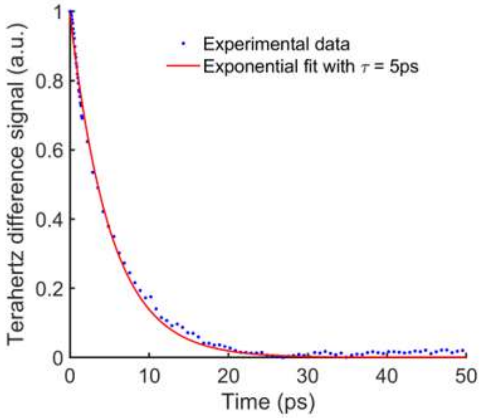

Fig. 2.6. Optical pump terahertz probe measurement of the p-type InAs ($p = 10^{19}\ cm^{-3}$) layer grown on a semi-insulating GaAs substrate.

Under these assumptions, Equation (2) in the p-type doped InAs region is modified to:

$$\frac{\partial n}{\partial t} = D_n \frac{\partial^2 n}{\partial x^2} + G \cdot \delta(t) - \frac{n}{\tau} \tag{4}$$

Considering current continuity at the interface between the undoped and p-doped InAs layers, Equations (3) and (4) are solved to obtain $n(x, y, z, t)$. The time-evolution of the carrier density, n.

Next, the density of the electron current injected to the nanoantenna at each surface point (y, z) is calculated as:

$$J_{injected}(0, y, z, t)\hat{x} = qv_e n(0, y, z, t)\hat{x} \tag{5}$$

To calculate the induced current on the nanoantennas, the nanoantenna area is first divided into discrete regions, i, with center locations of ($\mathrm{y_i}$, $\mathrm{z_i}$) and dimensions of $\Delta\mathrm{y}$ and Δz. The overall injected current at the ith discrete region is calculated as:

$$\tilde{\mathrm{I}}_{\mathrm{injected}}(\mathrm{y_i}, \mathrm{z_i}, \mathrm{f}) = \int_{\mathrm{y_i}-\frac{\Delta \mathrm{y}}{2}}^{\mathrm{y_i}+\frac{\Delta \mathrm{y}}{2}} \int_{\mathrm{z_i}-\frac{\Delta \mathrm{z}}{2}}^{\mathrm{z_i}+\frac{\Delta \mathrm{z}}{2}} \tilde{\mathrm{J}}_{\mathrm{injected}}(0, \mathrm{y}, \mathrm{z}, \mathrm{f})\mathrm{dydz} \tag{6}$$

$\tilde{\mathrm{J}}_{\mathrm{injected}}$ is the Fourier transform of the calculated time domain current, $\mathrm{J}_{\mathrm{injected}}$. The overall induced current on the nanoantennas is computed using a finite-element-method-based electromagnetic solver (ANSYS-HFSS). The calculated injected currents at all of the discrete regions, $\tilde{\mathrm{I}}_{\mathrm{injected}}(\mathrm{y_i}, \mathrm{z_i}, \mathrm{f})$, are included as multiple current sources across the nanoantenna area. One nanoantenna unit-cell is simulated and periodic boundary conditions are used in the y and z directions to account for the impact of the current injected to the adjacent nanoantennas while calculating the induced impulse response current on the nanoantenna, $\tilde{\mathrm{I}}_{\mathrm{impulse}}(\mathrm{z}, \mathrm{f})\hat{\mathrm{z}}$. Fig. 2.7a and 2.7b show the impulse response current of the nanoantenna array and its Fourier transform amplitude, respectively.

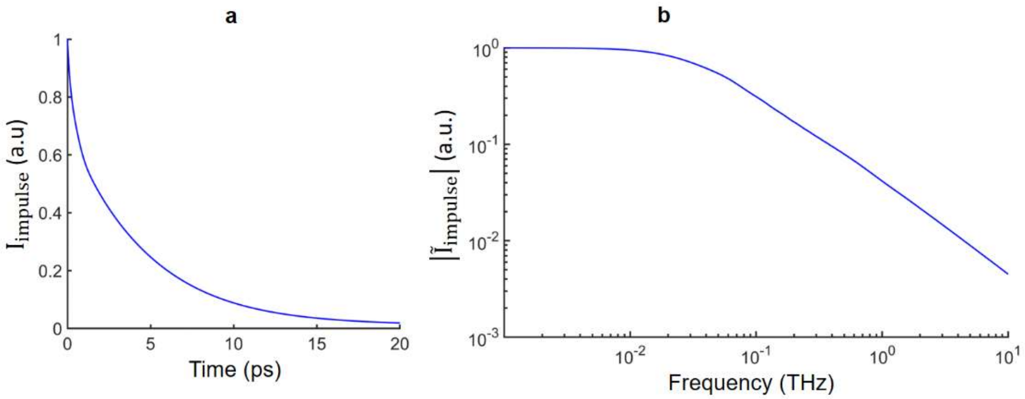

Fig. 2.7 Impulse response current of the nanoantenna array and its Fourier transform amplitude are shown in **a** and **b**, respectively.

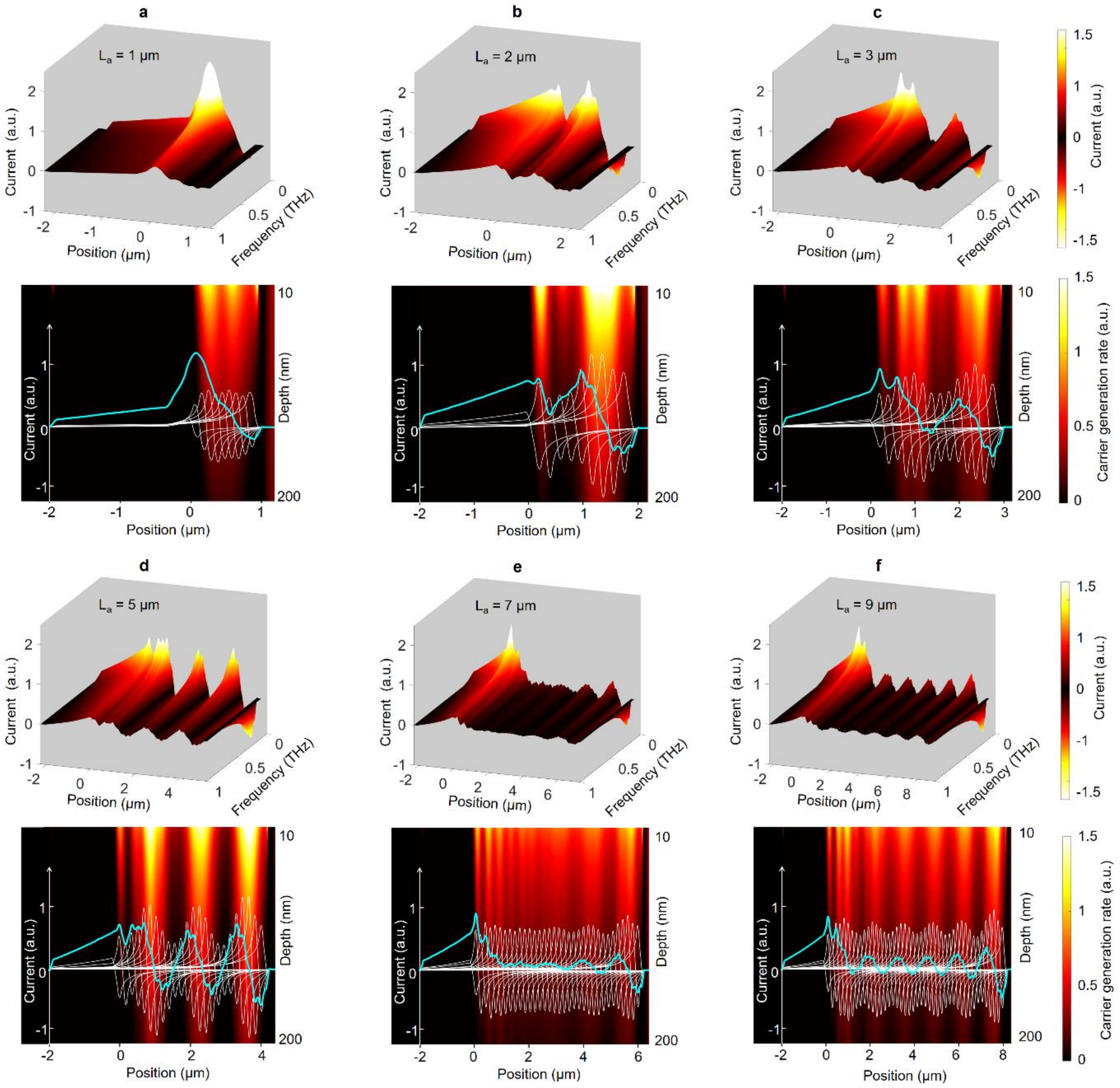

Fig. 2.8 a-f Top: The induced current on the nanoantennas as a function of frequency when the nanoantenna length (L_a) is varied from 1 μm to 9 μm. The ground line width (L_b) and the gap between the nanoantenna array rows (L_g) are chosen as 2 μm and 0.5 μm. The ground line is located between -2 μm and 0 positions and the nanoantenna is located between 0 and 1-9 μm positions along the z-axis. **a-f Bottom:** Decomposition of the total induced current on the nanoantennas (teal lines) to the individual contributions of the injected currents from different positions of the nanoantennas (white lines) at 0.2 THz. The background color maps show the electron generation profiles averaged over the nanoantenna width

Figures 2.8a-f (top) show the induced current on the nanoantennas for different nanoantenna lengths (L_a) varying between 1 μm and 9 μm as a function of frequency. The steady reduction in the current amplitudes at higher frequencies is due to the non-zero transit time of the photo-generated electrons in InAs to the nanoantennas.

Figures. 2.8 a-f (bottom) show the decomposition of the total induced current on the nanoantennas (teal lines) to the individual contributions of the injected currents from different positions of the nanoantennas (white lines) at 0.2 THz. The background color maps show the electron generation profiles computed using a Finite-difference time-domain electromagnetic solver (Lumerical), averaged over the nanoantenna width. As expected, the induced current at different nanoantenna location is proportional to the electron generation rate, which causes the ripples observed in the total induced currents. The current that is injected near the nanoantenna tip and the nanoantenna-ground line intersection has the highest contribution to the total induced current on the nanoantennas. As the current injection position is moved away from the nanoantenna tip and the nanoantenna-ground line intersection, it splits into two current components in opposite directions and with an approximately equal magnitude. This is because a fraction of the current that is injected to the adjacent nanoantennas flows to the neighboring nanoantennas and induces a current in the opposite direction. To better illustrate this phenomenon, we compare the induced current on a nanoantenna under three different scenarios: (1) when no neighboring nanoantenna is excited with an injected current (Fig. 2.9b); (2) when only the two neighboring nanoantennas are excited with an equal injected current (Fig. 2.9c); and (3) when six neighboring nanoantennas are excited with an equal injected current (Fig. 2.9d). As illustrated in Fig. 2.9b, when no neighboring nanoantenna is excited, the current flow is mostly oriented toward the ground line due to the impedance asymmetry created by the ground line. However, as the adjacent nanoantennas are excited (Figs. 2.9 b-d) a portion of their currents flows to the nanoantenna and produces a current flow in the opposite direction with an approximately equal magnitude. Furthermore, there is a rapid drop in the induced current closely after the current injection location. This is because the photo-generated electrons increase the substrate conductivity, which results in a fraction of the injected current leaking to the substrate, as illustrated in Fig. 2.8a. As the nanoantenna length is decreased from 9 µm (Fig. 2.8f) to 2 µm (Fig. 2.8b), the regions on the nanoantenna that do not contribute to the radiation are eliminated and the current density on the nanoantennas is increased, resulting in higher radiation powers. When the antenna length is reduced below 2 µm, the injected current to the nanoantenna is reduced because the ground lines shadow a major fraction of the optical beam, reducing the number of the photo-generated electrons in InAs (Fig. 2.8a).

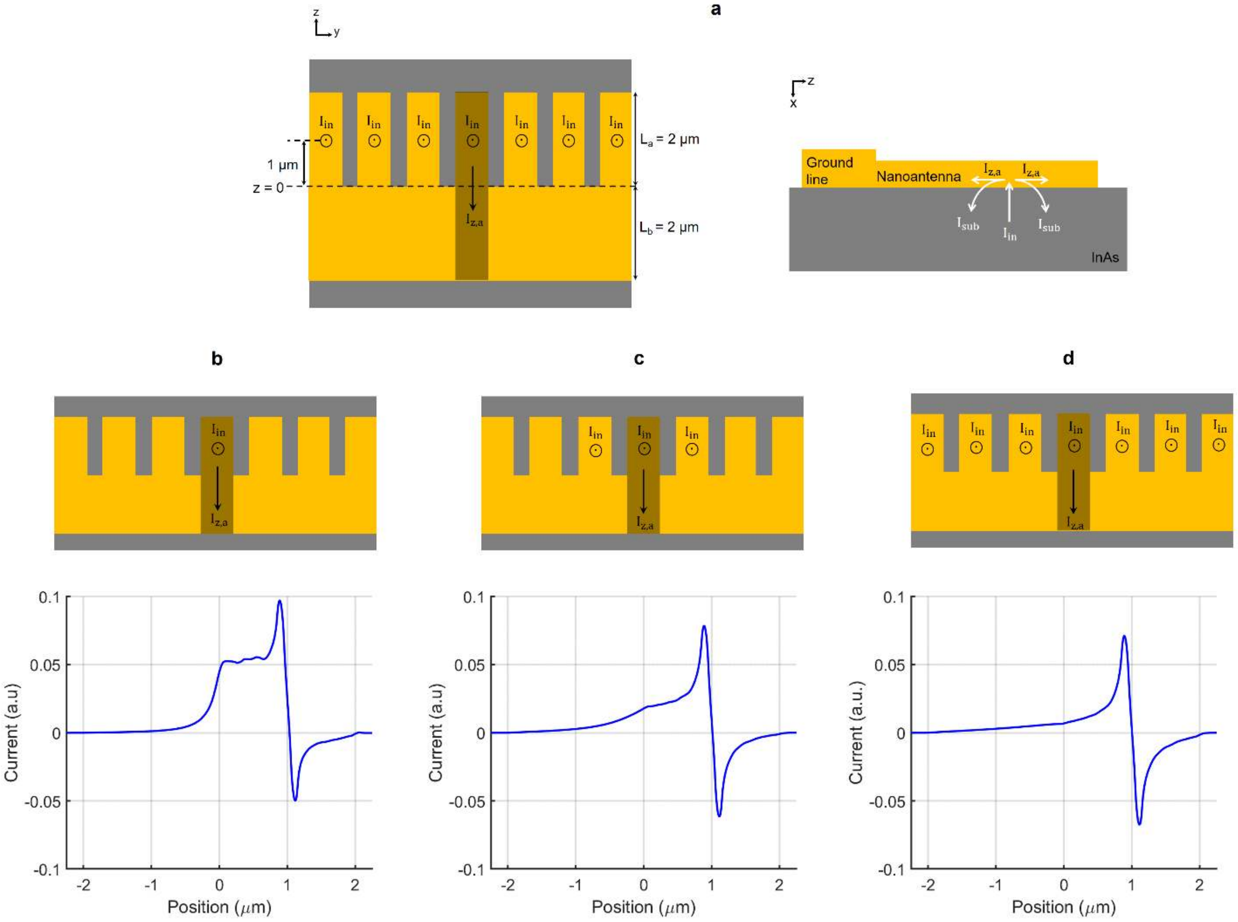

Fig. 2.9 a, Top view and side view of the simulated nanoantenna array to investigate the induced current on each nanoantenna. The induced current on the shaded nanoantenna when **b,** the neighboring nanoantennas are not excited, **c,** the two neighboring nanoantennas are excited, and **d,** six neighboring nanoantennas are excited.

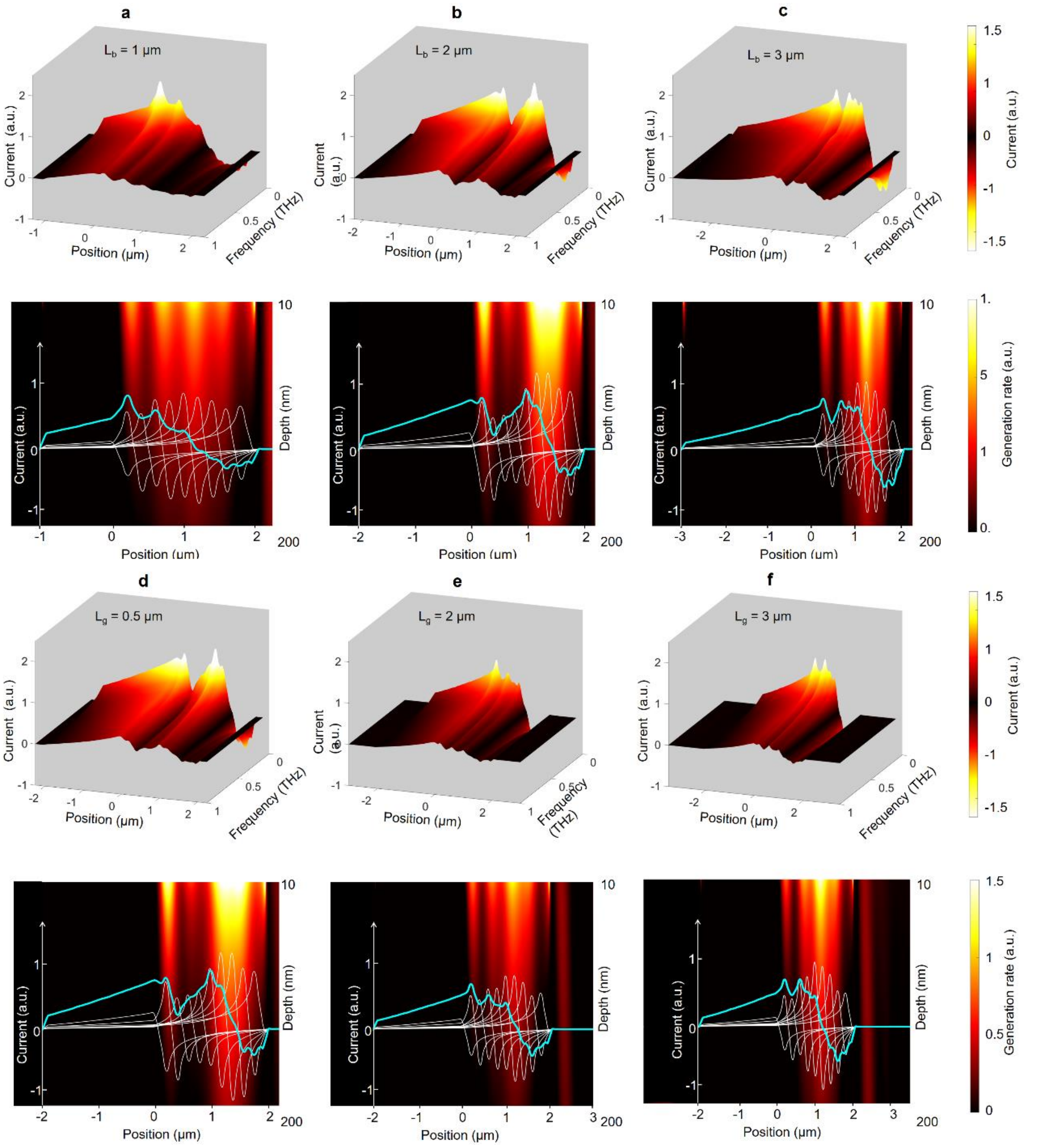

Fig. 2.10. a-c Top: The induced current on the nanoantennas as a function of frequency when the ground line width (L_b) is varied from 1 μm to 3 μm. The nanoantenna length (L_a) and the gap between the nanoantenna array rows (L_g) are chosen as 2 μm and 0.5 μm, respectively. The ground line junction with the nanoantenna is located at the 0 position and the nanoantenna is located between 0 and 2 μm positions along the z-axis. **d-f Top** The induced current on the nanoantennas as a function of frequency when the gap between the nanoantenna array rows (L_g) is varied from 0.5 μm to 3 μm. The nanoantenna length (L_a) and the ground line width (L_b) are chosen as 2 μm and 2 μm, respectively The ground line is located between -2 μm and 0 positions and the nanoantenna is located between 0 and 2 μm positions along the z-axis.**a-f Bottom**: Decomposition of the total induced current on the nanoantennas (teal lines) to the individual contributions of the injected currents from different positions of the nanoantennas (white lines) at 0.2 THz. The background color maps show the electron generation profiles averaged over the nanoantenna width.

Apart from the nanoantenna length, the ground line width (L_b) and the gap between the nanoantenna array rows (L_g) also have a significant impact on the radiation efficiency. Increasing the width of the ground lines provides a lower impedance ground path for the current flow through the nanoantennas, resulting in an increase in the induced current (see Fig. 2.10). However, increasing the ground line width beyond 2 μm reduces the injected current to the nanoantenna because the ground lines shadow a major fraction of the optical beam, reducing the number of the photo-generated electrons in InAs. Additionally, since the photo-generated electrons inside the gap between the nanoantenna array rows do not contribute to the radiation, this gap should be kept very small to maximize the fill factor of the radiating elements.

To calculate the radiated power from the nanoantenna array, the radiation field of a single nanoantenna, $E_i(r, \theta, \phi, f)$, is calculated first. Since the nanoantenna length is much smaller than the radiation wavelength and since most of the radiated power flows toward the semiconductor substrate, the vector potential can be written as [84]:

$$A_z(r, f) = \frac{\mu_0}{4\pi}\frac{e^{-jkr}}{r}\int_0^{L_a}\int_0^{W_a}\tilde{J}_{induced}(y', z', f)dy'dz' = \frac{\mu_0}{4\pi}\frac{e^{-jkr}}{r}S(L_a, W_a) \tag{7}$$

where $\tilde{J}_{induced}(y, z, f)$ is the induced surface current on the nanoantennas with an A/m unit, L_a and W_a are the length and width of each nanoantenna, respectively, $S(L_a, W_a)$ is the result of the integral, μ_0 is the permeability of the free space, $k = 2\pi f/c$ is the free space wavenumber, $r = \sqrt{x^2 + y^2 + z^2}$ is the observation point distance.

From the vector potential expression, the far-field radiated electric field for one nanoantenna can be written as [84]:

$$E_i(r,\theta,\phi,f) \approx j\eta_0 k\sin\theta \frac{e^{-jkr}}{4\pi r} S(L_a, W_a)\hat{\theta} \tag{8}$$

where η_0 is the wave impedance of the free space. Next, the radiation pattern of the nanoantenna array is calculated using the radiation pattern of one nanoantenna, $E_i(r,\theta,\phi,f)$ [84]:

$$E_{array}(r,\theta,\phi,f) = E_i(r,\theta,\phi,f) AF_y(\theta,\phi,f) AF_z(\theta,f) \tag{9}$$

where AF_y and AF_z are the array factor of the nanoantenna array in the y and z directions:

$$AF_y(\theta,\phi,f) = \frac{\sin\left(\frac{N_y\psi_y}{2}\right)}{\sin\left(\frac{\psi_y}{2}\right)}, \psi_y = p_y k\sin\phi\sin\theta \tag{10}$$

$$AF_z(\theta,f) = \frac{\sin\left(\frac{N_z\psi_z}{2}\right)}{\sin\left(\frac{\psi_z}{2}\right)}, \psi_z = p_z k\cos\theta \tag{11}$$

where p_y and p_z are the periodicity of the nanoantennas in the y and z directions, respectively, N_y and N_z are the number of nanoantennas in the y and z directions, respectively, and $k = 2\pi nf/c$ is the wavenumber at a given radiation wavelength ($n = n_{GaAs} = 3.6$). Finally, the radiated power from the nanoantenna array that propagates toward the semiconductor substrate is calculated as:

$$P(f) = \frac{1}{2\eta_0} \int_{-\pi/2}^{\pi/2} \int_{0}^{\pi} \left|E_{array}(\theta,\phi,f)\right|^2 r^2 \sin\theta d\theta d\phi \tag{12}$$

To better show the impact of the nanoantenna geometry, nanoantenna arrays with different nanoantenna lengths, ground line widths, and gaps sizes between the nanoantenna rows are fabricated with a total area of 1×1 mm^2 and their radiation power is characterized under the same femtosecond optical pulse illumination. As illustrated in Fig. 2.11 a-c, the measured terahertz radiation powers are in agreement with the theoretical predictions based on the induced current profiles on the nanoantennas.

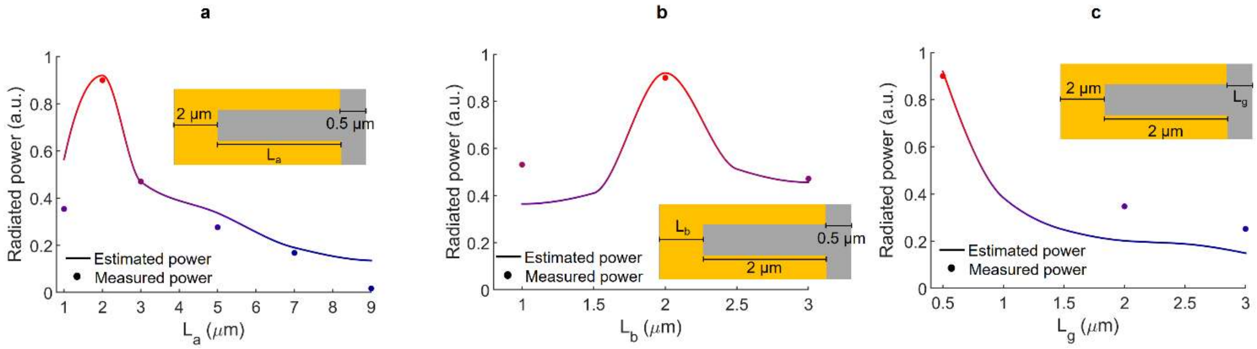

Fig. 2.11. Predicted and measured terahertz radiation power from fabricated nanoantenna arrays with different nanoantenna lengths, ground line widths, and gaps sizes between the nanoantenna rows are shown in **a, b,** and **c** respectively. All the fabricated nanoantenna arrays have a 1×1 mm^2 area and are characterized using the same optical pulses with 120 fs pulse width, 2.63 nJ pulse energy, and 76 MHz repetition rate.

Based on this analysis, the nanoantenna array with a 2 µm nanoantenna length, 2 µm ground line width, and 0.5 µm gap between the nanoantenna array rows, fabricated on a 100-nm-thick undoped InAs layer grown on a 500-nm-thick p-type (10^{19} cm^{-3}) is used to demonstrate the subsequent experimental results.

2.4. Results and Discussions

2.4.1. Terahertz Radiation Dependence to Optical Pump Power

. An optical parametric oscillator (OPO) pumped by a Ti:sapphire laser (Coherent Mira-HP) is used to pump the fabricated nanoantenna arrays. It provides optical pulses at a 1550 nm central wavelength, 76 MHz repetition rate and 120 fs pulsewidth. An ErAs:InGaAs-based photoconductive dipole antenna used as the terahertz detector [42]. The detector current is fed to

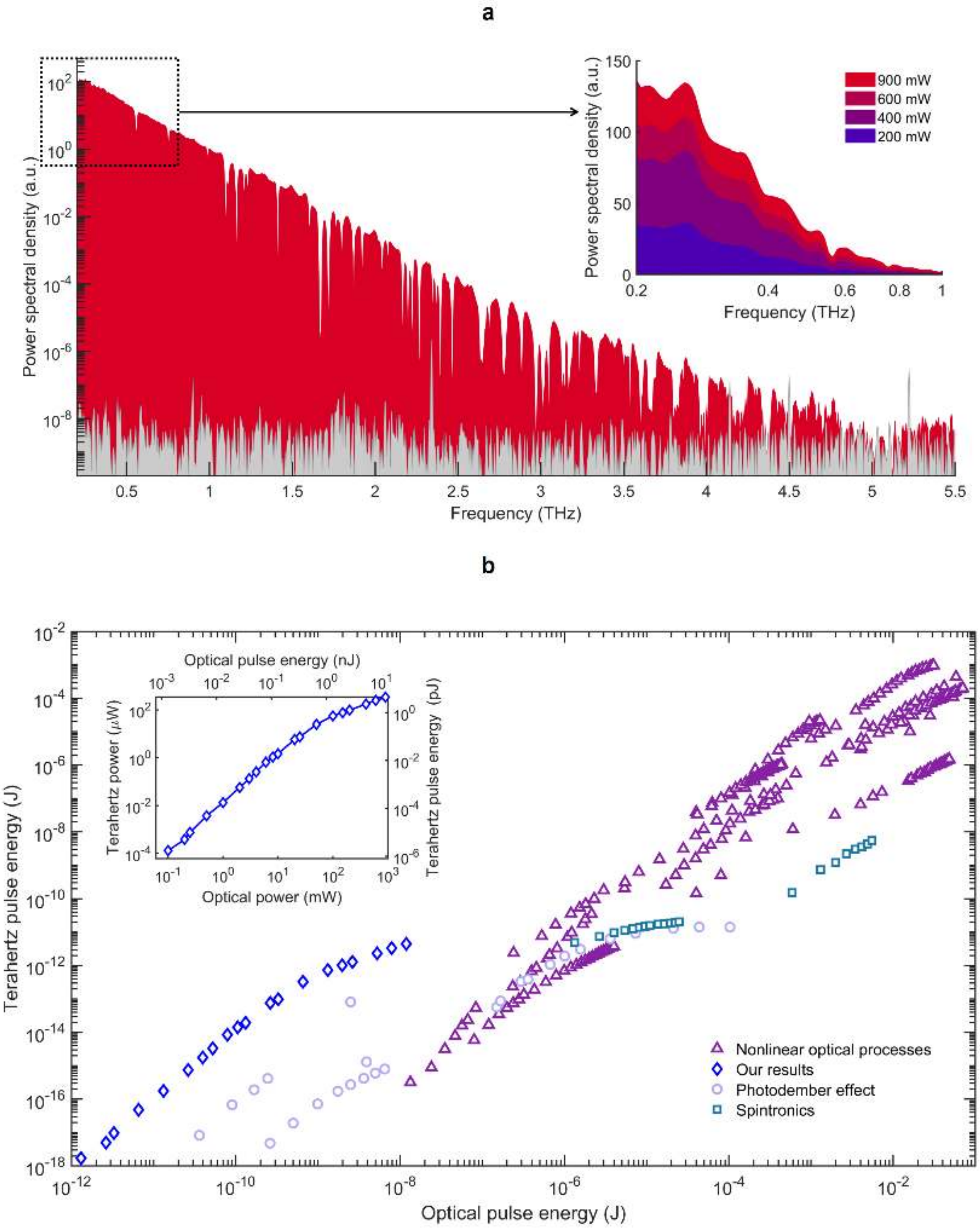

Fig. 2.12, a, The measured terahertz radiation spectrum (shown in red) along with the noise spectrum (shown in gray) when the nanoantenna array is excited by optical pulses with a 1550 nm center wavelength, 900 mW power, 120 fs pulsewidth, and 76 MHz repetition rate. 650 time-domain traces are captured and averaged to resolve this terahertz spectrum. Dependence of the radiation spectrum on the optical power level is shown in the inset. **b,** Measured terahertz pulse energy/power from the fabricated nanoantenna array as a function of the optical pulse energy/power (inset) in comparison with other passive optical-to-terahertz converters reported in the literature.

a transimpedance amplifier (FEMTO DHPCA amplifier with an amplifier gain of 10^6 V/A and a bandwidth of 1.8 MHz) followed by a lock-in amplifier (Zurich Instruments MFLI). Up to a 110 dB dynamic range and radiation up to 5 THz is achieved at a 900 mW optical pump power from the designed wavelength converter (Fig. 2.12a). Terahertz radiation power measurements are performed using a calibrated pyroelectric detector (Sensors und Lasertechnik THz-30 detector calibrated by Physikalisch-Technische Bundesanstalt, Germany). The measured terahertz pulse energy/power from the fabricated nanoantenna array as a function of the optical pulse energy/power (Fig. 2.12b inset) is compared with other passive optical-to-terahertz converters reported in the literature, which utilize nonlinear optical processes [18]–[21], [85]–[101], spintronics [28]–[31], and the photo-Dember effect[24]–[27]. The comparison indicates record-high efficiency of the plasmon-coupled surface states in passive wavelength conversion of nanojoule optical pulses to terahertz regime with efficiencies that exceed nonlinear optical methods by 4-orders of magnitude (Fig. 2.12b).

Comparison between the performance of the fabricated *passive* nanoantenna array with the reported *active* optical-to-terahertz converters (photoconductive terahertz sources) operating at 1550 nm wavelength [43], [54], [55], [57]–[60] is shown in Fig. 2.13. Considering the passive nature of the nanoantenna array, a comparison with other passive optical-to-terahertz converters provides a better assessment, which is shown in Fig. 2.12. However, the comparison with active optical-to-terahertz converters is shown here to point out the electrical requirements of the active optical-to-terahertz converters to radiate similar terahertz power levels. While the power efficiency of the passive nanoantenna array (bias voltage = 0, electrical power consumption = 0) is the same as its optical-to-terahertz conversion efficiency, the power efficiency of the active optical-to-terahertz converters (bias voltage ≠ 0, electrical power consumption ≠ 0) are much lower than their optical-to-terahertz conversion efficiency since considerable electrical current (mA-level) and bias voltage (100-200 V) are required to electrically pump these devices. The large electrical current and voltage levels required for pumping active optical-to-terahertz converters also degrade their reliability.

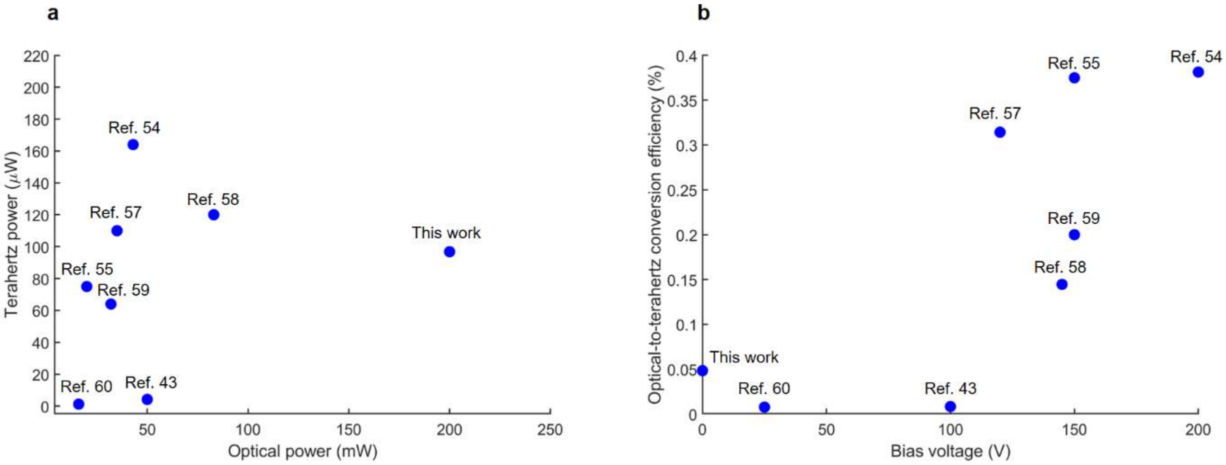

Fig. 2.13, Comparison of **a,** The radiated terahertz power as a function of optical power, **b,** The optical-to-terahertz conversion efficiency as a function of the bias voltage. between the fabricated passive nanoantenna array with the reported *active* optical-to-terahertz converters operating at 1550 nm wavelength.

Dependence of converted terahertz power to optical power is quadratic at optical pump powers below 10 mW (Fig. 2.14a), and linear at optical pump powers above 50 mW (Fig. 2.14b). Furthermore, a saturation behavior is observed at powers above 900 mW. The physical factor that determines the power dependence of the presented wavelength conversion scheme (quadratic, linear, or saturation) is the carrier screening effect. When the photo-generated carriers inside the semiconductor active area drift to the nanoantennas by the built-in electric field, the separated electron-hole pairs create an imbalance in charge density. This imbalance induces an electric field in the opposite direction relative to the built-in electric field. This screening field is proportional to the photo-generated carrier density in the substrate, as predicted by the Gauss's Law. Since the generated carrier density is proportional to the optical intensity incident on the nanoantenna array, the carrier screening effect is negligible at low optical power levels (screening field << built-in field). In this regime, the generated carrier density and induced current on the nanoantennas, hence, the radiated field have a linear dependence on the optical power level. Therefore, the radiated power from the nanoantenna array, which has a quadratic dependence on the radiated field has a

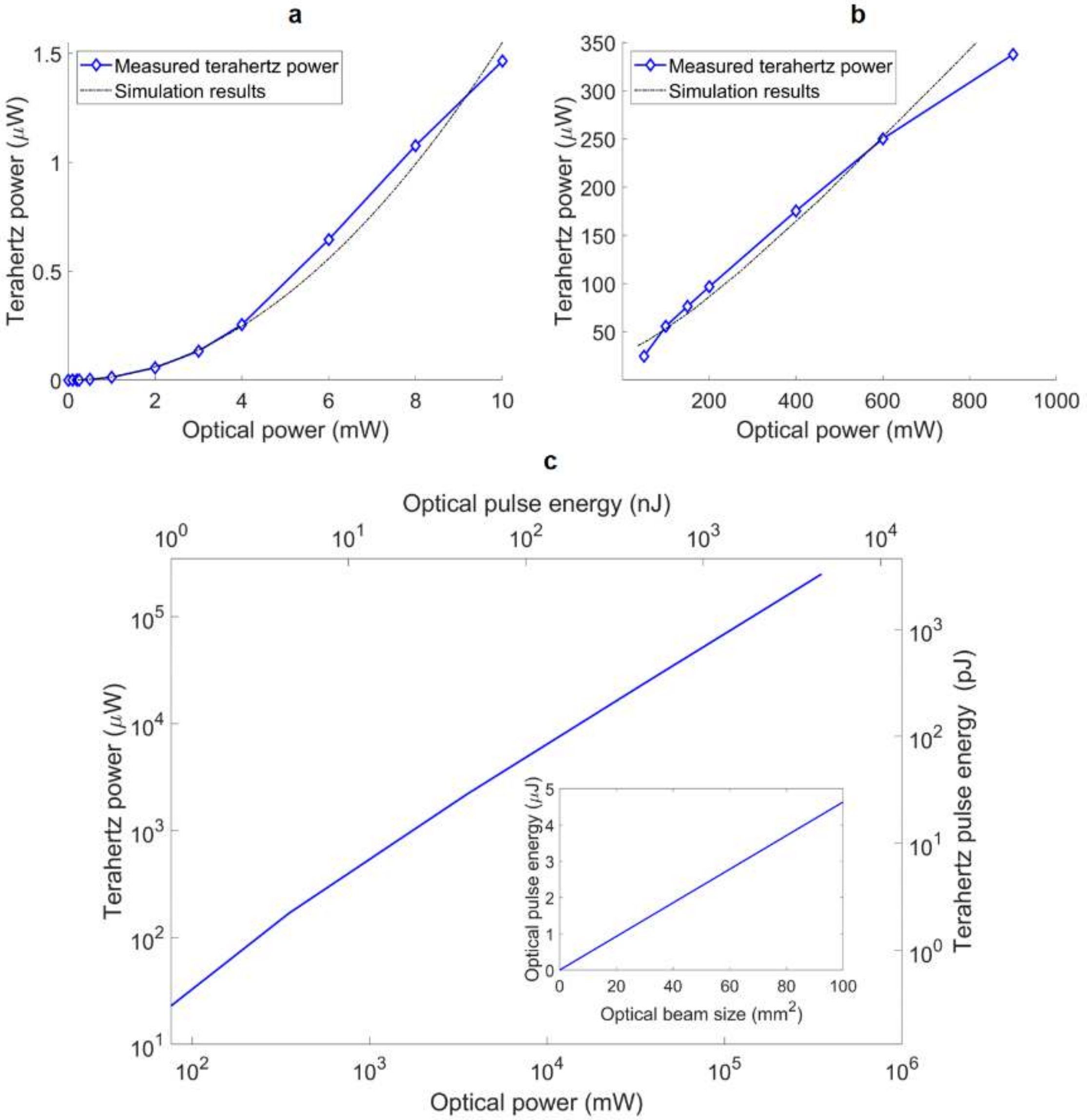

Fig. 2.14. Measured terahertz power at different optical pump powers in quadratic regime and linear regime is shown in **a** and **b** respectively**,** Dashed lines show the calculated converted power. **c**, The calculated total radiated power, $\int P(f)df$, indicating a linear dependence on the optical power level beyond 50 mW, when the optical beam size incident on the nanoantennas is linearly increased as a function of the optical power level (inset).

quadratic dependence on the optical power level in the low optical power regime as described by Eq. 12. As the screening field becomes comparable with the built-in electric field at higher optical powers, the carrier screening effect starts to limit the increase of the injected current from the substrate to the nanoantennas and the radiated power from the nanoantennas, changing the radiated power dependence on the optical power level from quadratic to linear and then saturation. To reduce the impact of the carrier screening effect on the wavelength conversion efficiency at high optical powers, the spot size of the optical beam incident on the nanoantenna arrays is increased so that the optical intensity is kept below the saturation regime at each power level. This beam size adjustment varies the number of the radiating nanoantennas while maintaining the same induced current on each nanoantenna and, thus, the same radiated field by each nanoantenna, $\mathrm{E_i}(\mathrm{r}, \theta, \phi, \mathrm{f})$. To predict the generated terahertz power in this regime the radiated field by the nanoantenna array is computed by Eqs. 9-11. By adjusting the beam size, the radiating nanoantenna array size in the y and z directions ($\mathrm{N_y}$ and $\mathrm{N_z}$) is changed in Eqs. 10 and 11. Finally, the radiated power at different terahertz frequencies is computed by calculating $\mathrm{P(f)}$ using Eq. 12.

2.4.2. Fiber-Coupled Optical-to-Terahertz Wavelength Converter

Fig. 2.15a shows a fabricated nanoantenna array on InAs that is simply glued at the tip of an optical fiber without using any intermediate optical component and can be pumped by a compact fiber laser. To demonstrate the fiber-coupled wavelength conversion performance shown in Fig. 2.15, the optical beam from the OPO is coupled to a polarization maintaining optical fiber (Thorlabs PM1550-XP) and the nanoantenna array is glued at the tip of the fiber. The optical pulsewidth incident on the nanoantenna array is increased to 150 fs due to the fiber dispersion. We experimentally demonstrate conversion of 3.68 nanojoule optical pulses with a 150 fs pulsewidth coupled to the fiber at a 1550 nm center wavelength to 1.78 picojoule terahertz pulses radiated from the nanoantenna array with more than a 4 THz bandwidth and 105 dB dynamic range (Fig. 2.15b).

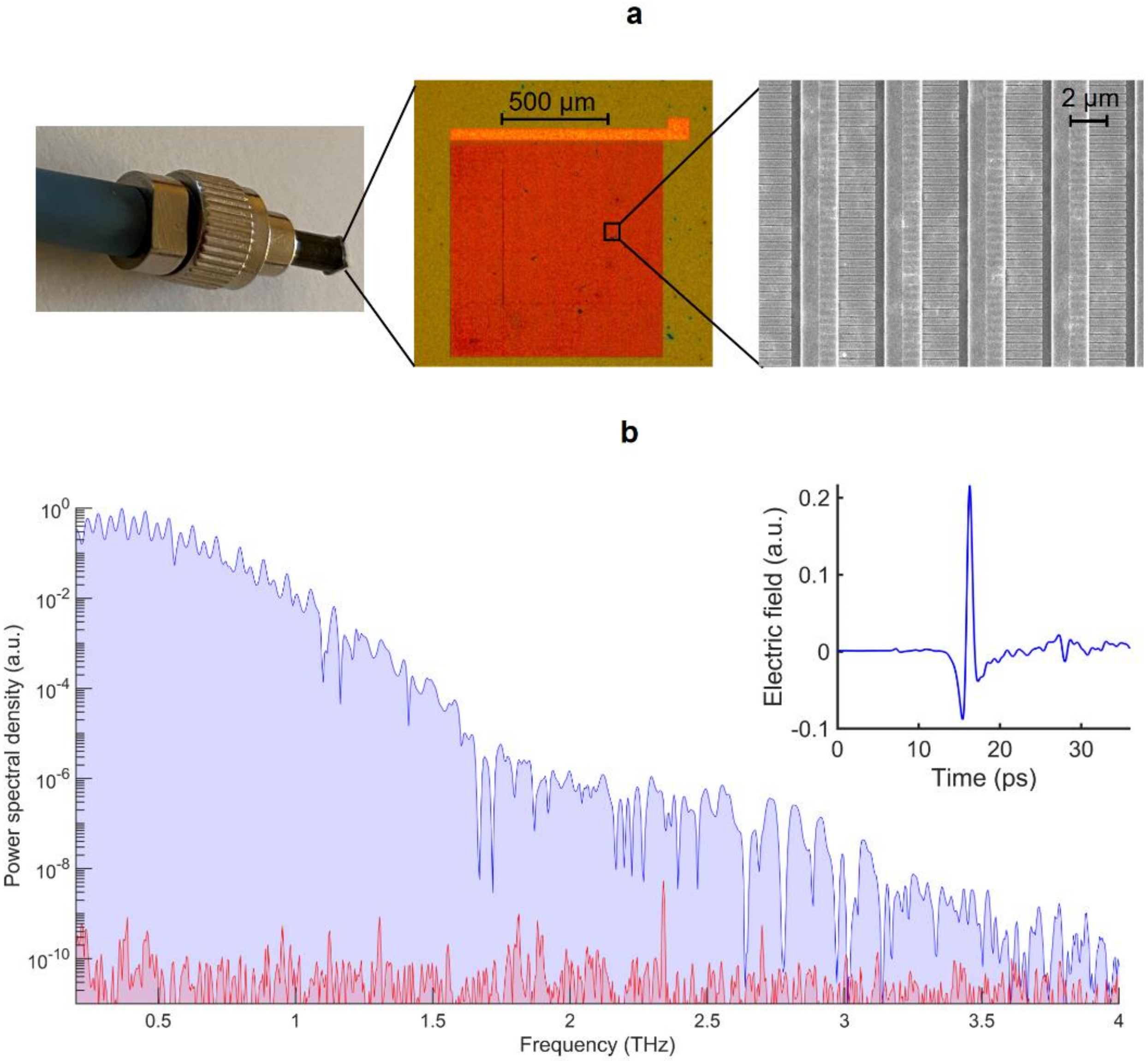

Fig. 2.15, a, Photograph, microscopy, and scanning electron microscopy images of a fabricated nanoantenna array on a substrate consisting of a 100-nm-thick undoped InAs layer grown on a 500-nm-thick InAs epilayer with a p-type doping of 10^{19} cm^{-3} grown on a semi-insulating GaAs substrate. **b,** Measured terahertz radiation (in blue) and noise (in red) spectra generated from the nanoantenna array when pumped by 3.68 nanojoule optical pulses at a 1550 nm center wavelength. The time-domain radiated terahertz pulse is shown in the inset. 3200 time-domain traces are captured and averaged to resolve this spectrum.

2.4.3. Optical Beam Size, Position, and Polarization Requirements

The measured terahertz radiation power from the nanoantenna array for different optical beam sizes and beam positions is shown in Fig. 2.16a. Beam size is defined as the beam diameter at which the optical intensity drops to $1/e^2$ (13.5%) of its peak value. The measurement results show less than a 25% reduction in the radiation power when the optical beam size is deviated from the optimum value (330 μm) by 50 μm. When the optical beam size is reduced relative to this optimum value, the wavelength conversion efficiency is reduced due to the carrier screening effect. When the optical beam size is increased relative to this optimum value, the wavelength conversion efficiency is reduced due to the destructive interference of the radiation from the relatively distant nanoantennas. The results also show less than a 25% reduction in the radiation power when the optical beam position is deviated from the optimum position (center of the nanoantenna array) by 250 μm. Therefore, wavelength conversion through plasmon-coupled surface states has a high tolerance for optical beam size variations and misalignment.

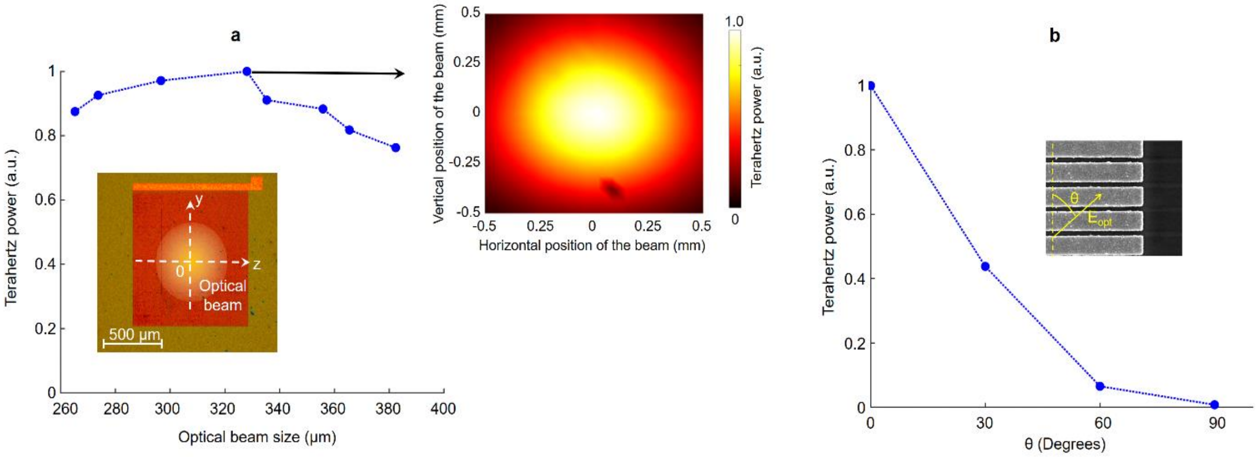

Fig. 2.16, a, The measured terahertz radiation power from the nanoantenna array for different optical beam sizes and beam positions. **b,** The measured terahertz radiation power from the nanoantenna array as a function of optical polarization.

The wavelength conversion efficiency drops when deviating from the optimum polarization for the excitation of surface plasmons (orthogonal to the nanoantennas) due to the reduction in the number of the photo-generated electrons at the semiconductor surface (Fig. 2.16b).

2.4.4. Continuous Wave Operation

The presented wavelength conversion scheme also operates in continuous-wave mode. The experimental setup to demonstrate continuous-wave operation is shown in Fig. 2.17a. The nanoantenna array is excited by two 1550 nm CW lasers (Santec TSL-510 and New Focus TLB-6730-P) with equal optical power levels. The radiation frequency is tuned by adjusting the beat frequency of the two lasers. In this experimental setup, the beat frequency is varied between 0.23 THz and 2.3 THz. The generated radiation from the nanoantenna array is routed to a harmonic mixer (VDI MixAMC with WR 1.5 and WR 2.2 waveguides) to down-convert it to an intermediate frequency (IF) signal in the GHz frequency range. The IF signal for each optical beat frequency is measured using an electrical spectrum analyzer (HP8592L), as shown in the Fig. 2.17a.

The measured radiation power from the nanoantenna array over the 0.23-2.3 THz frequency range using a pyroelectric detector is shown in Fig. 2.17b inset. The observed power roll-off as a function of frequency agrees with the roll-off predicted by the calculated impulse response. The deviations at low frequencies are due to the poor coupling of the radiation to the pyroelectric detector. The dips in the spectrum match the water vapor absorption lines [102], shown in red. The inset shows the dependence of the radiated power on the incident optical power at 0.35 THz. Unlike the pulsed operation mode, the radiated power follows a quadratic relation with the incident optical power.

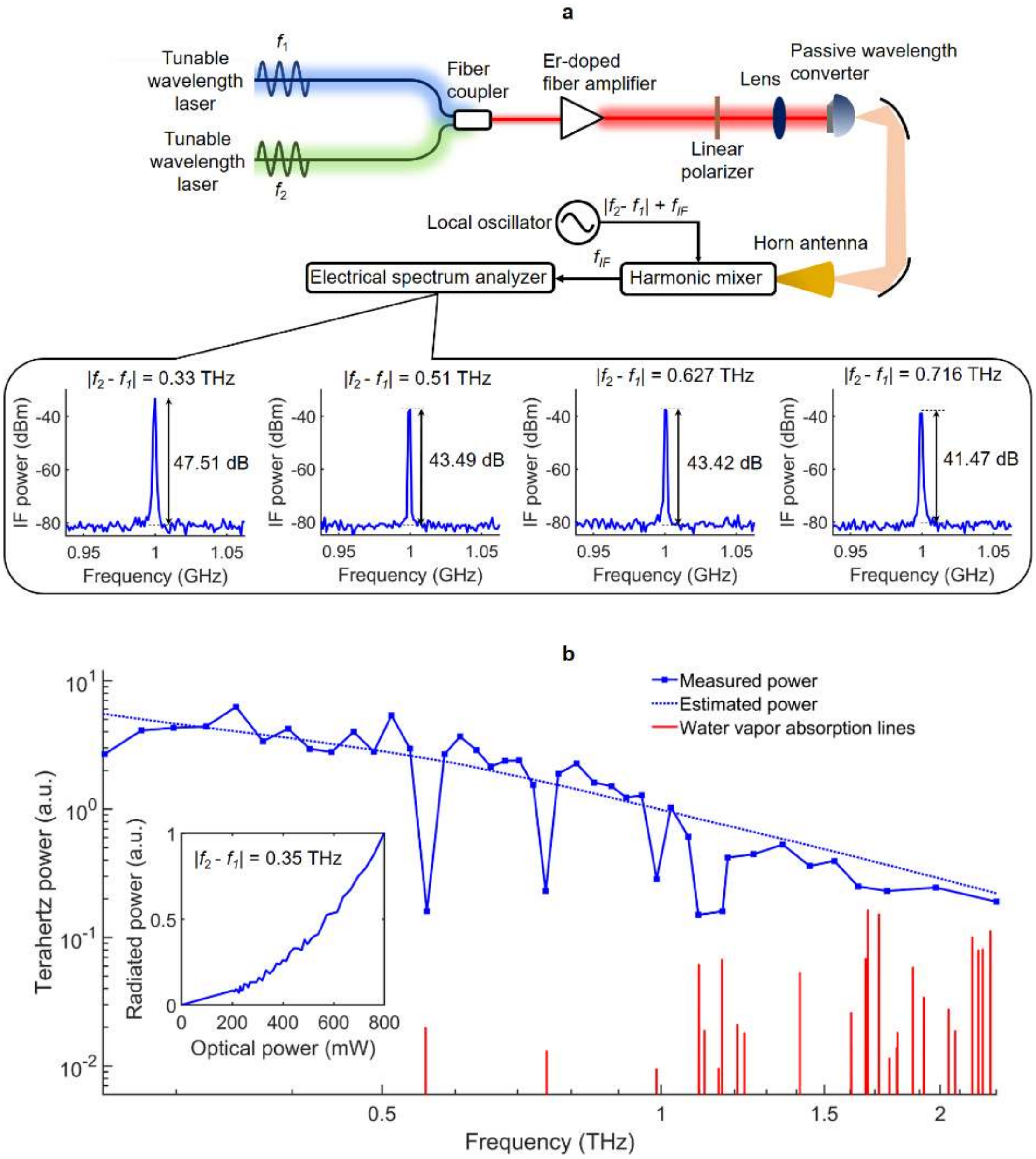

Fig. 2.17, a Top: Experimental setup used to measure CW radiation from the nanoantenna array. **a Bottom:** Measured IF signal for each optical beat frequency. **b,** The measured radiation power from the nanoantenna array over the 0.23-2.3 THz frequency range using a pyroelectric detector.

2.4.5. Operation under Smaller Optical Pulsewidth

The radiation bandwidth of the nanoantenna array can be extended by using a femtosecond laser with a shorter pulsewidth. Fig. 2.18 shows up to a 6.5 THz measured radiation bandwidth when the nanoantenna array is pumped with a femtosecond laser beam with a 23 fs pulsewidth. The measured full-width at half maximum (FWHM) pulse widths are 1.1 ps and 1.0 ps in the positive and negative cycles, respectively.

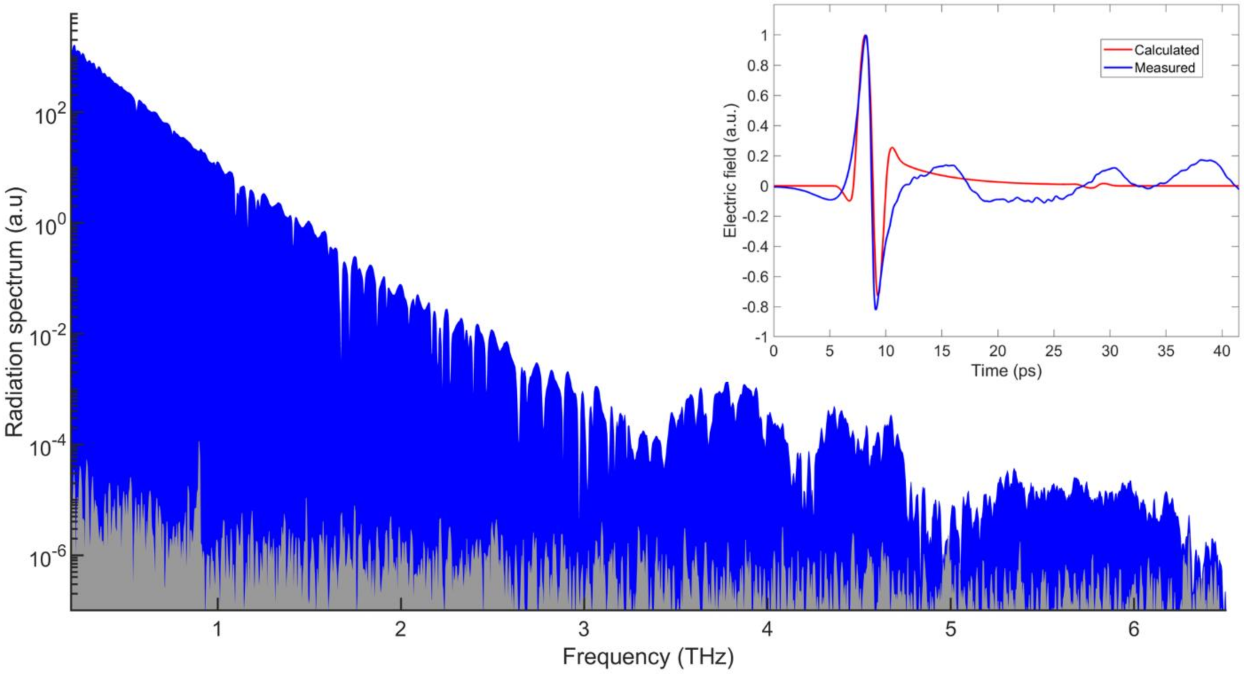

Fig. 2.18, The measured terahertz radiation spectrum (shown in blue) along with the noise spectrum (shown in gray) when the nanoantenna array is excited by optical pulses with a 1560 nm center wavelength, 100 mW power, and 23 fs pulsewidth. 1000 time-domain traces are captured and averaged to resolve this terahertz spectrum. Comparison between the calculated (red) and measured (blue) radiated field is shown in the inset.

The measured pulsewidth is then compared with the estimated pulsewidth. The estimated radiated pulse widths are calculated by convolving the impulse response current of the nanoantenna array (shown in Fig. 2.6) with the temporal profile of the femtosecond optical pulse to calculate the overall induced current on the nanoantennas. The frequency components of the induced current on the nanoantennas are obtained by taking the Fourier transform of the time-domain current. Next, the frequency-domain nanoantenna current is multiplied by the frequency response of the radiated field from the nanoantenna array. Finally, the time-domain radiated field is calculated by taking the inverse Fourier transform of the frequency-domain results. The calculated FWHM pulse widths of the positive and negative pulses are 1.1 ps and 0.8 ps, respectively, showing a close agreement between the calculated and measured data. The small broadening in the measured negative pulse and slow following oscillations are due to the low frequency oscillations induced in the output circuit of the photoconductive detector used for measuring the radiated field.

2.5. Methods

2.5.1. Semiconductor Growth

InAs layers are grown by molecular beam epitaxy (Veeco GEN-930) on semi-insulating GaAs (001) substrates. The growth is performed in an As-rich chamber at 400 °C. Be is used to dope the InAs to achieve a p-type doping concentration of 10^{19} cm^{-3}.

2.5.2. Device Fabrication

The nanoantenna arrays are first defined using electron-beam lithography (Vistec EBPG 5000+ES) followed by 3/97 nm Ti/Au evaporation (CHA solution electron beam evaporator) and lift-off. Ground lines are defined by electron-beam lithography followed by a 40/360 nm Ti/Au evaporation and lift-off. Finally, a 240-nm-thick Si_3N_4 anti-reflection coating is deposited using plasma enhanced chemical vapor deposition (STS Multiplex CVD).

Chapter 3: Plasmonics-Enhanced Photoconductive Terahertz Detector Pumped by Ytterbium-Doped Fiber Laser

3.1. Introduction

The ultrafast operation of a photoconductive detector can be achieved by reducing the transit time of the photocarriers to the output terminals. This approach eliminates the need for short-carrier-lifetime semiconductors and, consequently, increases the terahertz detection sensitivity by preventing the recombination of the photocarriers and enabling the use of high-mobility semiconductors. Such a short-carrier-lifetime-semiconductor-free photoconductive detector operating at an 800 nm pump wavelength was recently implemented by forming a plasmonic nanocavity around an undoped 170-nm-thick GaAs layer [53]. Here, a high-performance photoconductive terahertz detector is introduced that operates at ~1 µm optical pump wavelength range, at which high-power, low-cost, and compact Ytterbium (Yb)-doped femtosecond fiber lasers are commercially available. Despite their great promise, the sensitivity of previously-demonstrated photoconductive terahertz detectors operating at this wavelength range has been limited by the shortcomings of the short-carrier-lifetime semiconductors used for implementing these detectors, including low-temperature (LT) grown GaAs [103], LT-GaBiAs [104], [105], LT-InGaAs [36], [106], [107], LT-$In_{0.53}Al_{0.28}Ga_{0.20}As$ [108], or LT-$In_{0.53}Ga_{0.47}As$/ $In_{0.52}Al_{0.48}As$ superlattices [108], [109]. Instead of relying on a short-carrier-lifetime substrate, $In_{0.24}Ga_{0.76}As$/AlAs epilayers grown on a semi-insulating (SI) GaAs substrate are utilized. An array of plasmonic nanoantennas are used to induce terahertz electric field inside the substrate when illuminated by terahertz radiation. The plasmonic nanoantennas are designed to concentrate the optical pump beam very close to the nanoantenna tips, where the induced terahertz electric field is maximized, to ensure that most of the photo-generated carriers drift to the nanoantenna terminals in a sub-picosecond time scale. By providing a high spatial overlap between the photo-generated carrier and terahertz electric field profiles, a broad terahertz detection bandwidth exceeding 4 THz and more than a 95 dB SNR level is achieved without using a short-carrier-lifetime substrate, demonstrating more than a 10 dB sensitivity enhancement compared with previously-reported broadband photoconductive detectors operating at the 1 μm wavelength range.

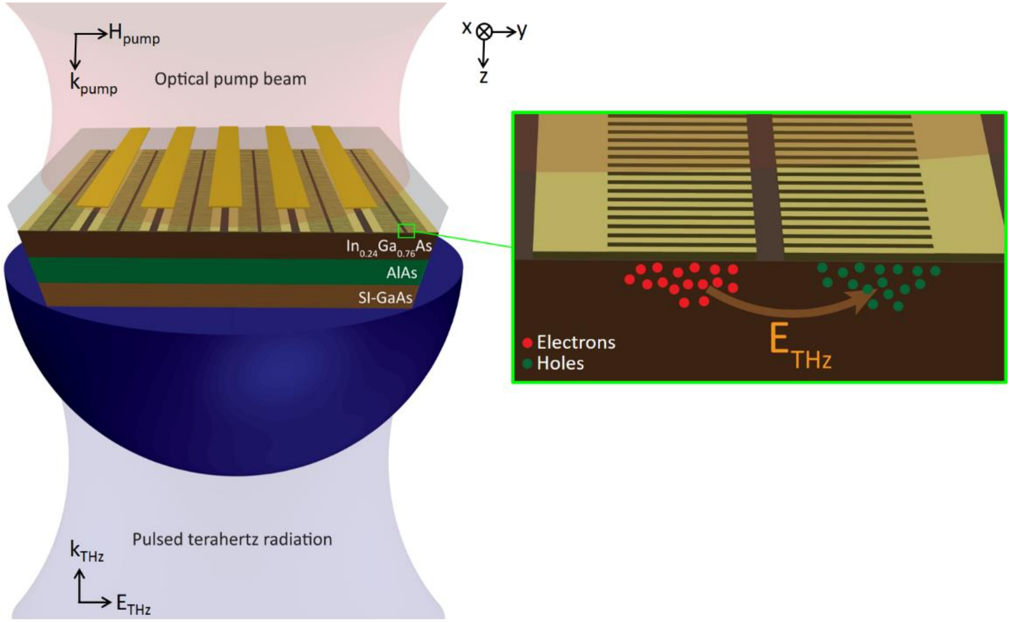

Fig. 3.1, Schematic of the designed plasmonic photoconductive terahertz detector

3.2. Design and Fabrication

Figure. 3.1 shows the schematic of the photoconductive terahertz detector, which consists of a two-dimensional array of plasmonic nanoantennas fabricated on undoped $In_{0.24}Ga_{0.76}As$/AlAs epilayers grown on an SI-GaAs substrate. The $In_{0.24}Ga_{0.76}As$ layer serves as the photo-absorbing active region. The mole fraction of indium is chosen as 0.24 to provide a cut-off wavelength larger than 1.1 μm [110]. Even though an InGaAs layer with a larger In fraction would provide higher optical absorption, the cut-off wavelength is chosen close to the operating wavelength to have high substrate resistivity and, thus, low Johnson-Nyquist noise current levels. Similarly, the AlAs layer serves as a high-resistivity buffer to suppress any Johnson-Nyquist noise current induced outside the photo-absorbing active region. The $In_{0.24}Ga_{0.76}As$ layer is grown undoped to offer high carrier mobility and dark resistance for high-sensitivity terahertz detection. While a thicker $In_{0.24}Ga_{0.76}As$ layer is expected to provide a larger number of photocarriers, the photocarriers generated deeper in the $In_{0.24}Ga_{0.76}As$ layer have a longer average transit time to the nanoantennas. The subsequent tradeoff between the terahertz detection bandwidth and sensitivity is analyzed by investigating two different thicknesses for the $In_{0.24}Ga_{0.76}As$ layer, 50 nm and 200 nm. Length of the nanoantennas is selected much smaller than terahertz wavelengths (4 μm) to provide a broad terahertz detection bandwidth [52]. The tip-to-tip gap between the nanoantenna terminals is chosen to induce a strong terahertz electric field, while providing a high spatial overlap between the terahertz electric field and photo-generated carrier profiles [52], [111]. Geometry of the nanoantennas, which are designed in the form of dipole gratings covered with a Si_3N_4 anti-reflection coating is chosen to enhance optical absorption inside the $In_{0.24}Ga_{0.76}As$ layer at the 1 μm pump wavelength range [111]. This enhancement is achieved through the excitation of surface plasmon waves, which increases the optical pump intensity and, thus, the photocarrier concentration at the interface between the $In_{0.24}Ga_{0.76}As$ layer and nanoantennas [46], [47], [50], [112]–[117]. An array of shadow metal stripes is deposited on the Si_3N_4 coating to prevent photocarrier generation at the gaps between the adjacent nanoantenna arrays. The shadow metals prevent photocurrent generation in the opposite direction to that of the nanoantennas.

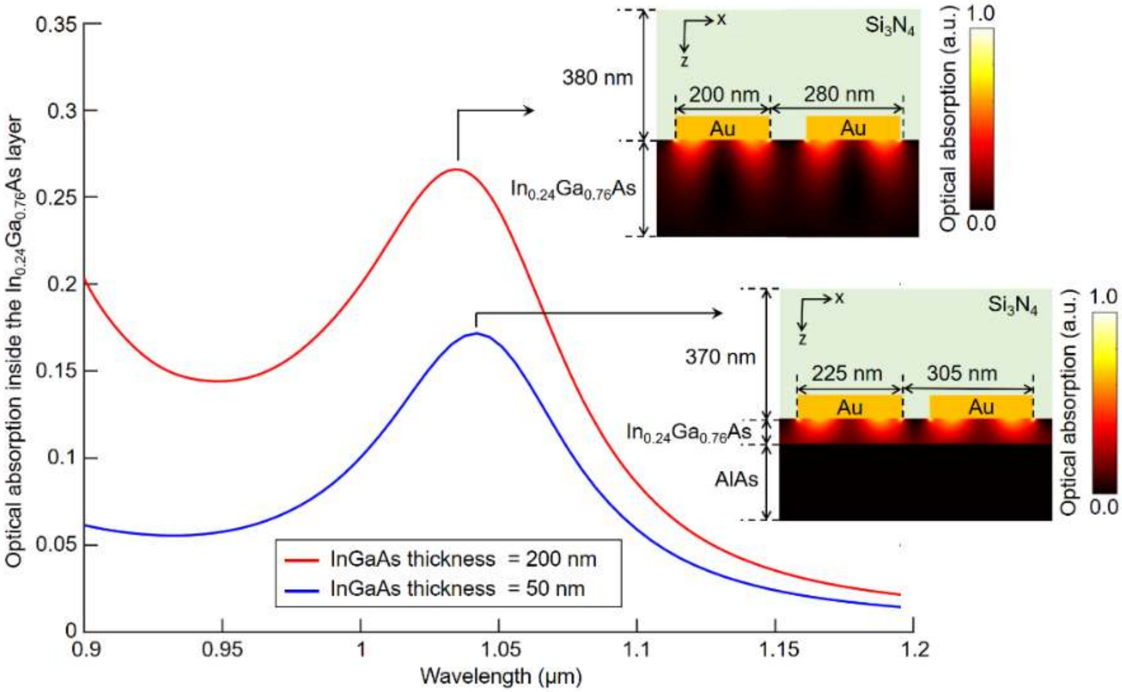

Fig. 3.2, Optical absorption spectra inside the $\mathrm{In_{0.24}Ga_{0.76}As}$ layer for the optimized nanoantenna geometries for different $\mathrm{In_{0.24}Ga_{0.76}As}$ thicknesses (left) and the color plot of the optical absorption profile inside the $\mathrm{In_{0.24}Ga_{0.76}As}$ layer at a 1.04 μm pump wavelength (right). Nanoantennas with a 225 nm width, 305 nm periodicity, and 3/77 nm Ti/Au thickness, covered with a 370-nm-thick $\mathrm{Si_3N_4}$ anti-reflection coating are designed for the detector fabricated on the substrates with a 50 nm $\mathrm{In_{0.24}Ga_{0.76}As}$ layer thicknesses. Nanoantennas with a 200 nm width, 280 nm periodicity, and 3/77 nm Ti/Au thickness, covered with a 380-nm-thick $\mathrm{Si_3N_4}$ anti-reflection coating are designed for the detector fabricated on the substrates with a 200 nm $\mathrm{In_{0.24}Ga_{0.76}As}$ layer thicknesses

A finite-difference time-domain (FDTD) method-based electromagnetic solver, Lumerical, is used to analyze the interaction between the optical pump beam and the designed plasmonic nanoantennas. Two nanoantenna geometries are optimized for the detectors fabricated on the substrates with 50 nm and 200 nm $\mathrm{In_{0.24}Ga_{0.76}As}$ layer thicknesses (Fig. 3.2 inset). The nanoantenna geometries are optimized by maximizing the optical absorption inside the $\mathrm{In_{0.24}Ga_{0.76}As}$ layer when a TM-polarized (*x*-polarized) optical beam is incident on the nanoantennas at a 1.04 μm wavelength. As illustrated in Fig. 3.2, the designed nanoantennas enable absorption of 15% and 25% of the incident optical pump photons at a 1.04 μm wavelength inside the 50-nm and 200-nm-thick $In_{0.24}Ga_{0.76}As$ layers under the nanoantennas, respectively, showing the tradeoff between the number of the photo-generated carriers and the average photocarrier transport time to the nanoantennas. Since the optical absorption is obtained through the excitation of surface plasmonic waves by an x-polarized optical pump beam, the optical absorption at the edge of the nanoantennas is not affected by the tip-to-tip gap size between the nanoantenna terminals (Fig. 3.3).

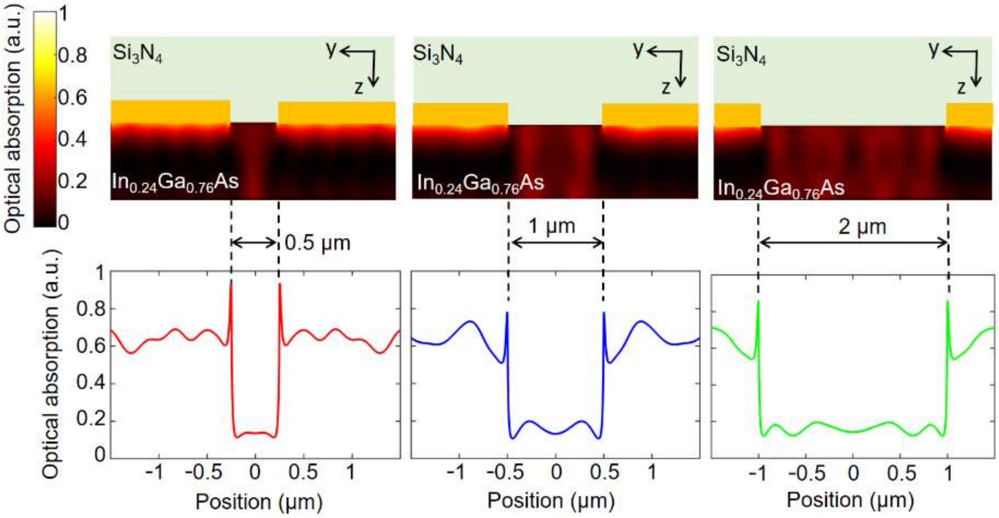

Fig. 3.3, Color map of the optical absorption inside the $In_{0.24}Ga_{0.76}As$ layer at a 1.04 μm wavelength (top) and the optical absorption at a 1 nm depth below the surface of the substrate (bottom) plotted at a yz-cross section passing through the middle of a nanoantenna for different tip-to-tip gap sizes.

However, the tip-to-tip gap size between the nanoantenna terminals has a significant impact on the intensity of the induced terahertz electric field at the nanoantenna edges, where the photocarrier concentration is maximized. Figure 4a shows the estimated electric field enhancement factor for a y-polarized terahertz radiation incident on the nanoantennas as a function of the tip-to-tip gap size between the nanoantenna terminals. The results show a substantial increase in the induced terahertz electric field as the tip-to-tip gap size is reduced from 2 μm to 1 μm, and 0.5 μm. Tip-to-tip gap sizes smaller than 0.5 μm are not considered in our analysis because they dramatically reduce optical absorption between the nanoantenna terminals due to the diffraction limit. The electric field enhancement factor is significantly enhanced in close proximity to the nanoantenna edges, where the photocarrier concentration is also enhanced [52]**.** The high spatial overlap between the induced terahertz electric field and the photocarrier concentration near the nanoantenna edges provides sub-picosecond transit times for the majority of the photo-generated carriers. Since the terahertz electric field is in parallel with the nanoantennas, the incident terahertz radiation can efficiently couple to the nanoantenna terminals if the effective radiation wavelength is much larger than the periodicity of the nanoantennas along the *y*-axis [52], [111]. Therefore, the induced electric field is reduced as the terahertz frequency is increased, as shown in Fig. 3. 4b.

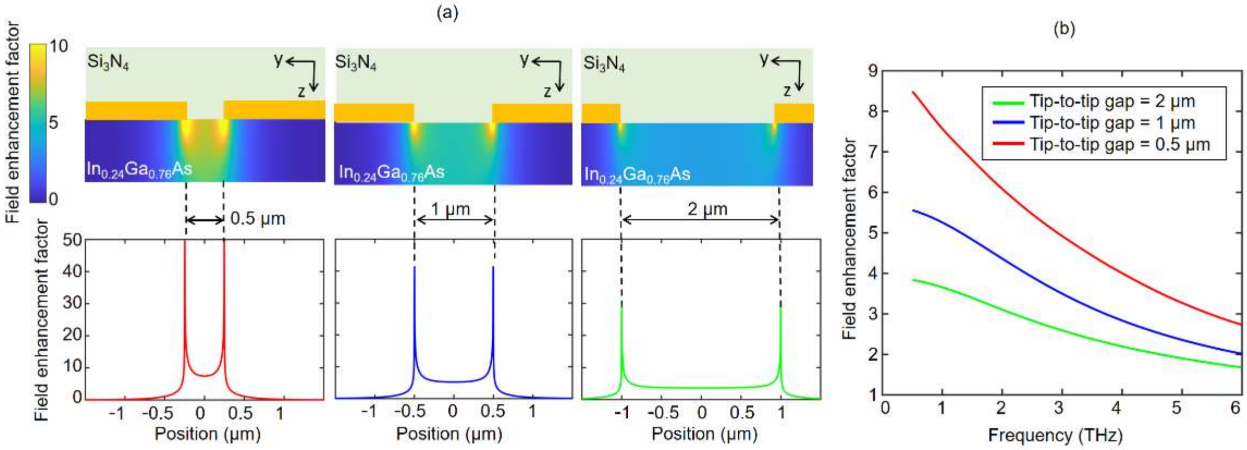

Fig. 3.4, (a) Color map of the electric field enhancement factor inside the $In_{0.24}Ga_{0.76}As$ layer at 1 THz (top) and the electric field enhancement factor at a 1 nm depth below the surface of the substrate (bottom) plotted at a *yz*-cross section passing through the middle of a nanoantenna for different tip-to-tip gap sizes. **(b)** The electric field enhancement factor in the middle of the nanoantenna tips at a 1 nm depth below the surface of the substrate as a function of frequency for different tip-to-tip gap sizes.

Detector prototypes with the designed nanoantennas are fabricated on 200/200 nm and 50/200 nm $In_{0.24}Ga_{0.76}As$/AlAs epilayers grown on two SI-GaAs substrates in a molecular beam epitaxy (MBE) chamber at 510 °C. Photoluminescence spectroscopy is performed after the growth to confirm that the cut-off wavelength of the grown substrates is above 1.1 µm Fig. 3.5(a). The roughness of the grown substrates is then analyzed using an atomic force microscope, to confirm that the substrate surface is smooth enough for the subsequent device fabrication steps (Fig. 3.5b). Then, the nanoantennas are patterned using electron-beam lithography followed by a 3/77 nm Ti/Au deposition and lift-off. Next, the nanoantenna connection lines and output pads are patterned via optical lithography, followed by a 20/180 nm Ti/Au evaporation and lift-off. The Si_3N_4 antireflection coating is deposited via plasma-enhanced chemical vapor deposition. Then, shadow metal stripes are patterned by optical lithography, followed by a 10/90 nm Ti/Au deposition and lift-off. Finally, the Si_3N_4 coating that covers the contact pads is cleared using reactive ion etching to open vias for electric connection.

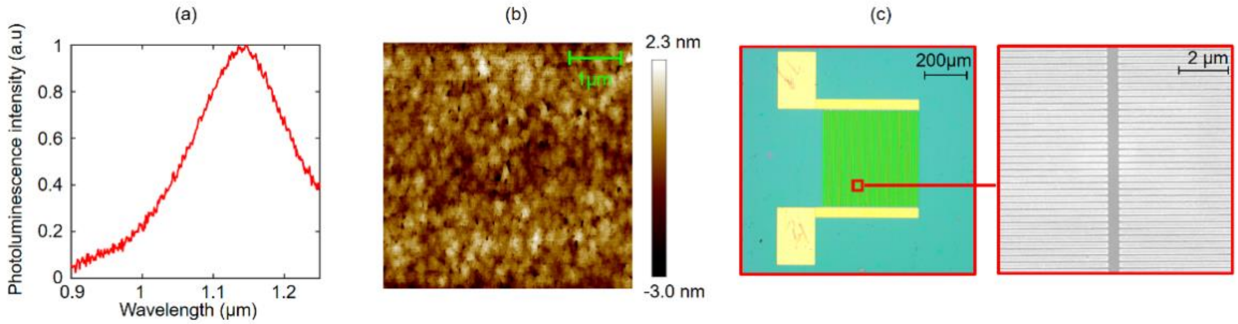

Fig. 3.5, (a) Photoluminescence measurements of a 200-nm-thick $In_{0.24}Ga_{0.76}As$ layer epitaxially grown on a 200-nm-thick AlAs layer on an SI-GaAs substrate. **(b)** Atomic force microscopy scan of the grown $In_{0.24}Ga_{0.76}As$/AlAs epilayer. **(c)** Microscopy image of the fabricated detector on this substrate and the scanning electron microscopy image of the plasmonic nanoantennas.

In order to investigate the impact of the geometrical parameters, plasmonic nanoantenna arrays with tip-to-tip gap sizes of 0.5 µm, 1 µm, 2 µm and array sizes of 0.5×0.5 mm^2 and 0.25×0.25 mm^2 are fabricated. Figure 3.5c shows the microscopy image of a fabricated detector prototype and the scanning electron microscopy image of the fabricated nanoantennas with a tip-to-tip gap size of 0.5 µm**.**

3.3. Experimental Results and Discussion

The fabricated photoconductive detectors are characterized in a THz-TDS setup with an Yb-doped fiber laser that generates 88-fs-wide pulses with an 80 MHz repetition rate and a 1.04 μm center wavelength. Performance of the detectors is characterized in response to terahertz pulses generated by a bias-free plasmonic photoconductive source pumped by the Yb-doped fiber laser. Polarization of the optical pump beam is set to be perpendicular to the nanoantennas (along *x*-axis) and polarization of the terahertz radiation is adjusted to be in parallel with the nanoantennas (along *y*-axis). An optical pump $1/e^2$ diameter of 300 μm is used for all of the characterization measurements. To investigate the impact of the tip-to-tip gap size between the nanoantenna terminals, the time-domain electric field profiles of the detected radiation by the detector prototypes with tip-to-tip gap sizes of 0.5 μm, 1 μm, and 2 μm are measured (Fig. 3.6a). All of the detectors used for these measurements are fabricated on a 200-nm-thick $In_{0.24}Ga_{0.76}As$ layer and have a 0.5×0.5 mm^2 active area. All of these measurements are performed at a 10 mW average optical pump power and a 6.8 μW average terahertz power. For each measurement, 10 time-domain traces are captured and averaged to reduce the background noise. As predicted by our theoretical analysis, the highest responsivity is achieved when using a 0.5 μm gap size, which offers the highest induced terahertz electric field to drift the photo-generated carriers. Figure 3.6d shows the detected radiation spectra by the detectors with tip-to-tip gap sizes of 0.5 μm, 1 μm, and 2 μm. Johnson-Nyquist noise is the dominant noise mechanism in the presented photoconductive detectors, which is determined by the average device resistance under optical pump illumination [32], [33], [39], [118]. Since the majority of the photo-generated carriers are tightly confined to the nanoantenna edges, the average device resistance is dominated by the concentration of these photocarriers. Since the photocarrier concentration near the nanoantenna edges is not considerably affected by the tip-to-tip gap size (Fig. 3.3), similar noise current levels are obtained for all three detectors with tip-to-tip gap sizes of 0.5 µm, 1 µm, and 2 µm. Overall, the detector with the tip-to-tip gap size of 0.5 µm offers the highest SNR level, as shown in Fig. 6d.

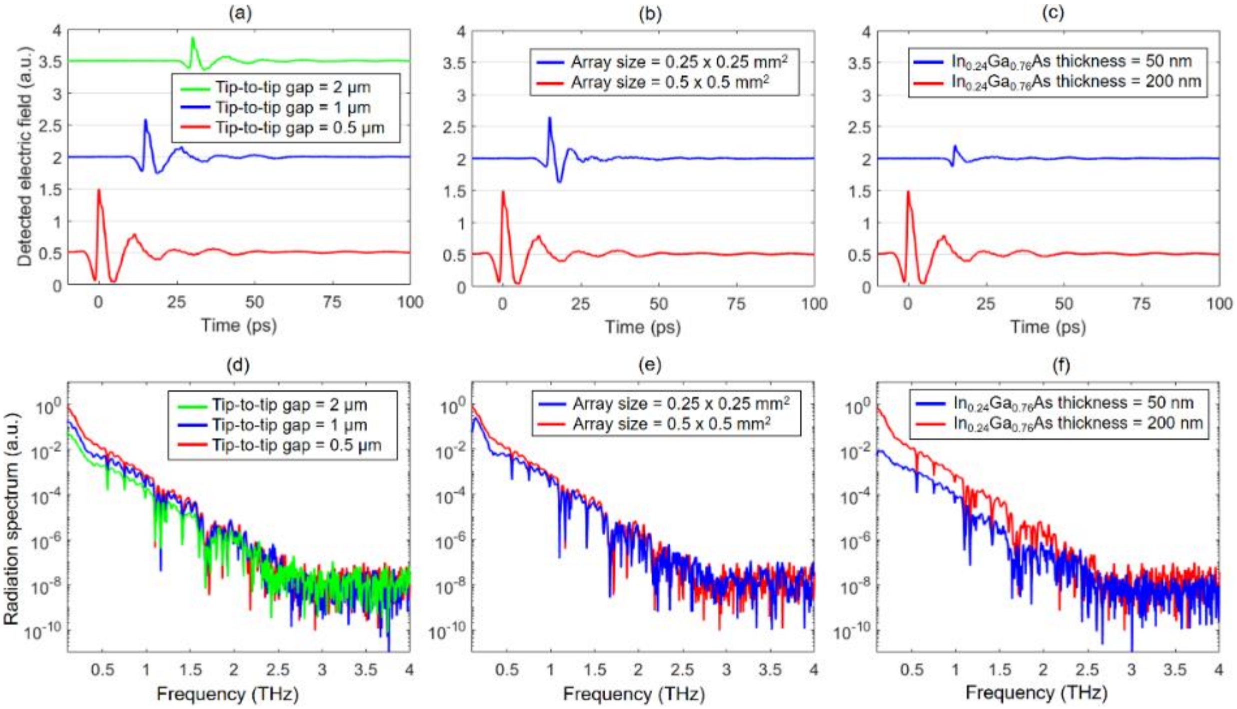

Fig. 3.6, Measured electric field as a function of **(a)** the tip-to-tip gap size between the nanoantenna terminals, **(b)** the nanoantenna array size, **(c)** the $In_{0.24}Ga_{0.76}As$ layer thickness and their corresponding radiation spectra are shown in **(d)**, **(e)**, and **(f)**, respectively.

The impact of the nanoantenna array size on the performance of the presented detector is also analyzed by comparing the performance of two detectors with 0.25×0.25 mm^2 and 0.5×0.5 mm^2 active areas. Both detectors are fabricated on a 200-nm-thick $In_{0.24}Ga_{0.76}As$ layer and have a tip-to-tip gap size of 0.5 µm. All of these measurements are performed at a 10 mW average optical pump power and a 6.8 µW average terahertz power. The optical pump spot size on the nanoantenna arrays is adjusted to maximize responsivity of each detector. For each measurement, 10 time-domain traces are captured and averaged to reduce the background noise. As illustrated in Fig.

3.6b, the detector with a larger array size offers higher responsivity because it can capture a larger fraction of the incident terahertz radiation. It should be noted that the spot size of the terahertz radiation incident of the nanoantenna arrays is diffraction limited. Therefore, the lower frequency components of the incident terahertz radiation have a larger spot size. As a result, the responsivity enhancement of the detector with a 0.5×0.5 mm^2 active area is more pronounced at lower frequencies, as shown in Fig. 3.6e. Under the same optical pump power, the same total number of photocarriers is generated in close proximity to the nanoantennas of both detectors, resulting in similar photocurrent and, thus, noise current levels in both devices. Overall, the detector with a 0.5×0.5 mm^2 active area offers higher SNR level, as shown in Fig. 3.6e. The impact of the $In_{0.24}Ga_{0.76}As$ layer thickness on the performance of the presented detector is also analyzed by comparing the performance of two detectors with 50 nm and 200 nm $In_{0.24}Ga_{0.76}As$ layer thicknesses. Both detectors have a 0.5×0.5 mm^2 active area and a tip-to-tip gap size of 0.5 μm. All of these measurements are performed at a 10 mW average optical pump power and a 6.8 μW average terahertz power. For each measurement, 10 time-domain traces are captured and averaged to reduce the background noise. Figure 3.6c shows that the detector fabricated on the 200-nm-thick $In_{0.24}Ga_{0.76}As$ layer provides higher responsivity because it absorbs a larger fraction of the optical pump photons, as illustrated in Fig. 3.2. Therefore, a larger number of photocarriers drift to the nanoantennas to contribute to terahertz detection. Since the photocarriers generated deeper in the $In_{0.24}Ga_{0.76}As$ layer experience longer transit times to the nanoantennas, the observed responsivity enhancement of the detector fabricated on the 200-nm-thick $In_{0.24}Ga_{0.76}As$ layer is more pronounced at lower terahertz frequencies (Fig. 3.6f). Both detectors show similar noise current levels, since they have the same number of photocarriers generated in close proximity to the nanoantennas. Overall, the detector with a 200-nm-thick $In_{0.24}Ga_{0.76}As$ layer offers higher SNR level, as shown in Fig. 3.6f.

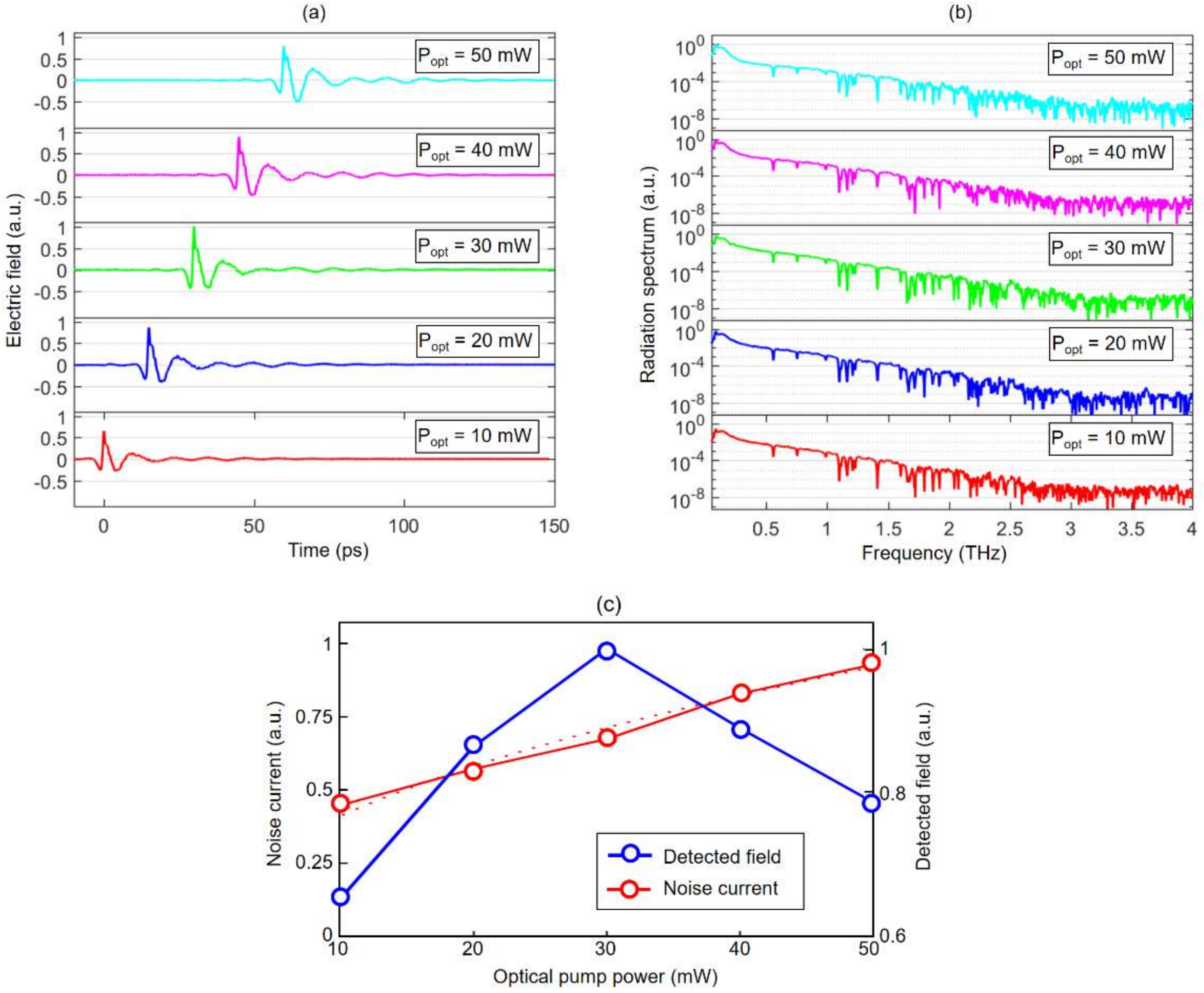

Fig. 3.7, Measured electric field profiles and their corresponding radiation spectra at different optical pump powers for the detector fabricated on a 200-nm-thick $In_{0.24}Ga_{0.76}As$ layer with a 0.5 μm tip-to-tip gap size and a 0.5×0.5 mm^2 active area are shown in **(a)** and **(b)**, respectively. Dependence of the peak time-domain electric field and the noise current level to the optical pump power is shown in **(c)**. The red dotted line shows the square root of the optical pump power.

In addition to the device geometry, the optical power level used for pumping the photoconductive terahertz detectors has a significant impact on their responsivity and noise performance. Figure 3.7a shows the time-domain electric field profiles of the detected terahertz radiation for the device fabricated on a 200-nm-thick $In_{0.24}Ga_{0.76}As$ layer with a 0.5 μm tip-to-tip gap size and a 0.5×0.5 mm^2 active area, at different optical pump power ranging from 10 mW to 50 mW. This device geometry is chosen because of the high SNR values it provides, as shown in Fig. 6. All of these measurements are performed at a 6.8 μW average terahertz power. For each measurement, 10 time-domain traces are captured and averaged to reduce the background noise. As expected, the detected electric field increases as the optical pump power is increased above 10 mW, since more photocarriers drift to the nanoantennas to contribute to terahertz detection. However, the detected electric field drops at optical powers above 30 mW because the increased number of photocarriers accumulating at the edge of the nanoantennas screen the induced terahertz electric field.

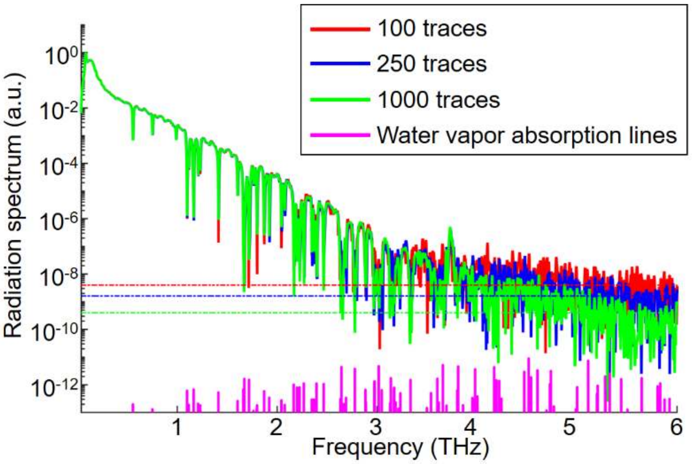

Fig. 3.8, Impact of increasing number of averaged time-domain traces in the resolved radiation spectrum. Dashed lines indicate the noise level of the acquired spectrums with different number of traces.

As mentioned before, Johnson-Nyquist noise is the dominant noise mechanism in the presented photoconductive detectors. Therefore, the average noise current is expected to be inversely proportional to the square root of the average device resistance under optical pump illumination. Since the average device resistance, dominated by the tightly confined photocarriers near the nanoantenna edges, is inversely proportional to the optical pump power, the average noise current is expected to be proportional to the square root of the optical pump power. This dependence is confirmed experimentally, as shown in Fig. 3.7c, where the dotted line shows the square root of the optical pump power. Overall, the highest SNR level is achieved at a 30 mW optical pump power.

The SNR level is increased further by increasing the number of the time-domain traces that are captured and averaged. The radiation spectra obtained with different number of traces are shown in Fig. 3.8. As expected, the noise level is reduced when the number of traces is increased. A terahertz detection bandwidth of more than 4 THz and a peak SNR level of 95 dB is provided by the designed detector when 1000 time-domain traces are captured and averaged, demonstrating a 10 dB SNR enhancement compared with previously reported broadband photoconductive detectors operating at the 1 μm optical pump wavelength range [36], [103]–[109]. The observed absorption dips in the spectra are due to the water vapor present in the ambient, which match the water vapor absorption lines reported in HITRAN database [102].

In summary, we present a photoconductive terahertz detector that operates at the 1 μm optical wavelength range at which high-power, low-cost and compact Yb-doped femtosecond fiber lasers are commercially available. The detector is equipped with an array of plasmonic nanoantennas that enables ultrafast device operation by reducing the transit time of the photo-generated carriers. As a result, short-carrier-lifetime substrates that reduce the responsivity of conventional photoconductive terahertz detectors are eliminated and higher SNR levels are achieved. The geometric parameters of the nanoantennas are selected to provide a high spatial overlap between the profiles of the photo-generated carriers and the induced terahertz electric field in close proximity to the nanoantenna terminals. By optimizing the nanoantenna geometry, peak SNR levels exceeding 95 dB and detection bandwidths exceeding 4 THz are achieved when using a 30 mW optical pump power. The demonstrated SNR is 10 dB higher than previously-reported broadband photoconductive detectors operating at the 1 μm optical pump wavelength range. It should be noted that the 95 dB SNR is achieved at a 6.8 μW terahertz radiation power and much higher SNR levels can be achieved under higher terahertz radiation power levels. In addition, the terahertz detection sensitivity can be further increased by embedding the photo-absorbing active region in a plasmonic nanocavity to increase the quantum efficiency. Therefore, the presented photoconductive terahertz detector architecture driven by Yb-doped femtosecond fiber lasers could be very effective for future THz-TDS system used in practical applications.

Chapter 4: Impact of Metal Adhesion Layers on the Performance of Plasmonic Photoconductive Terahertz Sources

4.1. Introduction

The metals used in plasmonic contact electrodes have a significant impact on the photoconductive source performance for various reasons. First, the electron-hole pairs generated in the semiconductor substrate should overcome the energy barrier at the metal–semiconductor junction to reach the terahertz radiating element. In addition, the utilized metal should offer strong optical field enhancement near the of the plasmonic contact electrodes. Moreover, the utilized metal must have satisfactory mechanical contact with the semiconductor substrate.

Au is extensively used for plasmonic contact electrodes because of the strong plasmonic enhancement factors it offers at near-infrared optical wavelengths. In addition, unlike many other high-conductivity metals (e.g., Ag), Au does not oxidize and offers reliable device operation. Moreover, the high electrical and thermal conductivities of Au are highly beneficial for operation at high optical pump powers. However, Au requires an adhesion layer to stick to the photoconductive substrate, and this layer plays a significant role in the electrical and optical characteristics of the device. Thus, it is important to use a suitable adhesion layer that provides satisfactory electrical and optical properties.

Here, the impact of the Au adhesion layer on the performance of plasmonic photoconductive sources fabricated on a GaAs substrate is analyzed. Electrical and optical characteristics of possible Au adhesion layers indicate that Cr is the most promising adhesion layer for plasmonic contact electrodes. As a proof-of-concept, we fabricate large-area plasmonic photoconductive sources with Cr/Au and Ti/Au plasmonic contact electrode gratings. We demonstrate that the use of a Cr adhesion layer instead of Ti, which is used in most of the existing plasmonic photoconductive sources [45]–[51], [112], [115]–[117], [119], offers up to an 80% enhancement in the generated terahertz powers. We attribute this improvement to the superior optical and electrical properties of Cr/Au contacts compared to Ti/Au. Record high terahertz power levels of up to 6.7 mW are achieved under a 700 mW optical pump power.

4.2. Device Design

To begin with, I analyze the impact of the Au adhesion layer on the electrical properties of the plasmonic photoconductive sources fabricated on a GaAs substrate. The large potential barrier between GaAs and Au introduces a Schottky contact at the Au-GaAs junction. As stated before, the photo-generated carriers in the semiconductor substrate should overcome the energy barrier at the metal–semiconductor junction to reach the terahertz radiating element. Various alloyed Au adhesion layers (e.g., AuGe/Ni, Pd/Ge, Ti/Pt) have been introduced to form an ohmic contact with GaAs to lower the energy barrier of the Au–GaAs junction [120]–[126]. The use of alloyed ohmic contacts has been effective in enhancing the radiation efficiency of conventional photoconductive terahertz sources [127], [128]. However, since these contacts require multiple metal layers beneath Au, they significantly reduce the plasmonic enhancement factors by increasing the distance between Au and GaAs substrate. Therefore, they are not appropriate for plasmonic photoconductive terahertz sources.

Among the alternative Au adhesion layers that form a Schottky contact with GaAs, Cr, Ti, and Al have very good adhesion to GaAs [129]. However, Al has a tendency to react with Au under high current densities and introduces a larger energy barrier at the GaAs interface compared to Cr and Ti [130], [131]. The theoretically estimated barrier heights at the ideal Ti-GaAs and Cr-GaAs interfaces, which are calculated from the metal work functions and GaAs electron affinity, predict a lower barrier height at the Ti-GaAs interface. In fact, Ti has been the most commonly used Au adhesion layer in the previously demonstrated plasmonic photoconductive terahertz sources [45]–[51], [112], [115]–[117], [119]. However, experimental results suggest a lower barrier height at the Cr-GaAs interface [130]–[132] due to the Fermi-level pinning by various interface states formed at the metal–semiconductor interfaces, as illustrated in Fig. 4.1**.**

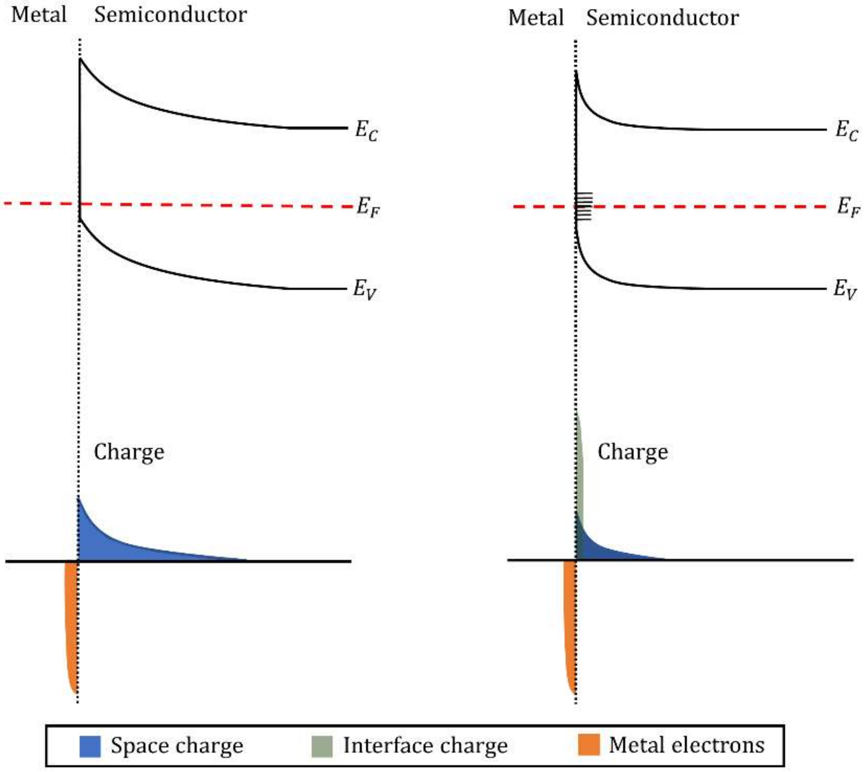
Metal
Semiconductor
E_C
E_F
E_V
Charge
Metal
Semiconductor
E_C
E_F
E_V
Charge
Space charge
Interface charge
Metal electrons

Fig. 4.1, Comparison between the energy band diagram of an ideal metal–semiconductor Schottky junction (a) and a metal–semiconductor Schottky junction with interface states (b).

In an ideal metal-semiconductor Schottky junction, free electrons in the semiconductor conduction band move toward the metal side, leaving behind positive charges (Fig. 4.1a). In this case, the profile of the positive charges in the semiconductor determines the semiconductor band bending and the barrier height. However, in practical situations, many interface states exist because of the so-called metal induced gap states and/or contact imperfections [125], [132]. These interface states act as a source of charge during the Fermi level alignment and establish a different equilibrium condition. When these interface states behave as donor states (Fig. 4.1b), a lower number of electrons is transferred from the semiconductor conduction band to the metal side. This reduces the semiconductor band bending and lowers the barrier height compared to an ideal metal-semiconductor junction[125]. Cr is believed to introduce additional As donor states at the Cr-GaAs interface [133], [134] that lower the barrier height. However, the As accumulation has not been observed for the Ti-GaAs interface, which results in larger barrier heights [134], [135].

The impact of Cr and Ti, as the Au adhesion layers of plasmonic contact electrodes, on the terahertz radiation performance of the plasmonic photoconductive sources is further investigated in this work. Two identical plasmonic photoconductive sources with Cr and Ti adhesion layers are fabricated on the same SI-GaAs substrate, and their terahertz radiation performance is analyzed under the same conditions. A large area plasmonic photoconductive source architecture with plasmonic contact electrode gratings is used for this investigation [50]. As illustrated in Fig. 4.2, the large area plasmonic photoconductive source consists of a two-dimensional array of plasmonic contact electrode gratings connected to the anode bias lines of the device. The plasmonic contact electrodes act as the terahertz radiating elements. To achieve high optical absorption inside the GaAs substrate, the plasmonic contact electrodes are covered using a Si_3N_4 anti-reflection coating. The geometry of the plasmonic contact electrode gratings (130 nm metal width, 100 nm metal gap, 5/45 nm Cr/Au and Ti/Au height, and 320 nm Si_3N_4 thickness) is chosen to concentrate a large portion of the incident optical pump beam close to the plasmonic contact electrodes at an optical wavelength of 780 nm [111]. To achieve broadband terahertz radiation, the length of the plasmonic contact electrodes is chosen to be much smaller than the terahertz wavelengths (5 µm). Every other gap between the anode and cathode bias lines is shadowed by a metal stripe deposited on the Si_3N_4 anti-reflection coating to block light transmission into the substrate. This prevents the generation of terahertz field in the opposite direction to the radiated field from the plasmonic contact electrodes.

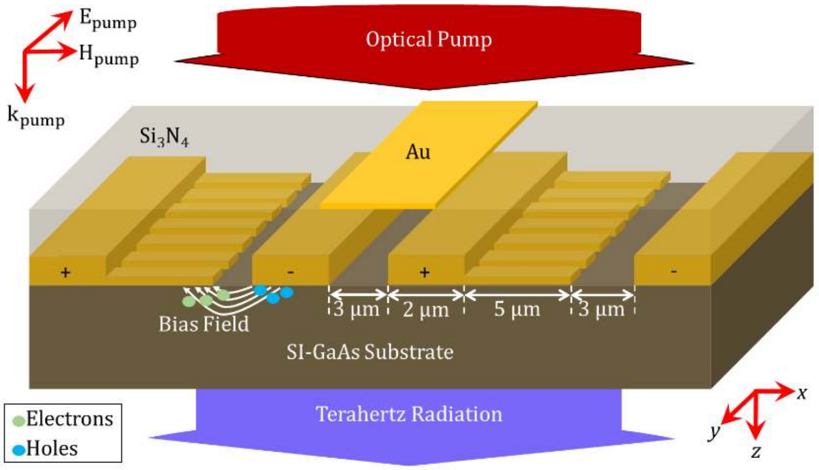

Fig. 4.2, Schematic diagram of the large-area plasmonic photoconductive terahertz source architecture used in our study.

A finite-element-method-based electromagnetic solver (COMSOL) is used to analyze the interaction of a TM-polarized optical pump beam with the Cr/Au and Ti/Au plasmonic contact electrodes. Figure 4.3a shows the optical transmission spectra through the Cr/Au and Ti/Au plasmonic contact electrodes into the GaAs substrate. While the maximum optical transmission through both plasmonic contact electrodes is achieved at an optical pump wavelength of 780 nm, a slightly higher optical transmission level is achieved through the use of the Cr/Au plasmonic contact electrode. The main reason for this difference is the smaller Cr skin depth at near-infrared wavelengths, which leads to a lower optical loss in the Cr adhesion layer compared to Ti. This effect is shown in Fig. 4.3b, and the optical loss within the two adhesion layers is compared at different wavelengths. The smaller Cr skin depth also leads to slightly higher plasmonic enhancement factors near the plasmonic contact electrodes. As illustrated in Fig. 4.3c, a higher optical absorption is achieved inside the GaAs substrate close to the Cr/Au plasmonic contact electrodes. This leads to more photocarriers that can reach the contacts in sub-picosecond time intervals to contribute to the terahertz radiation.

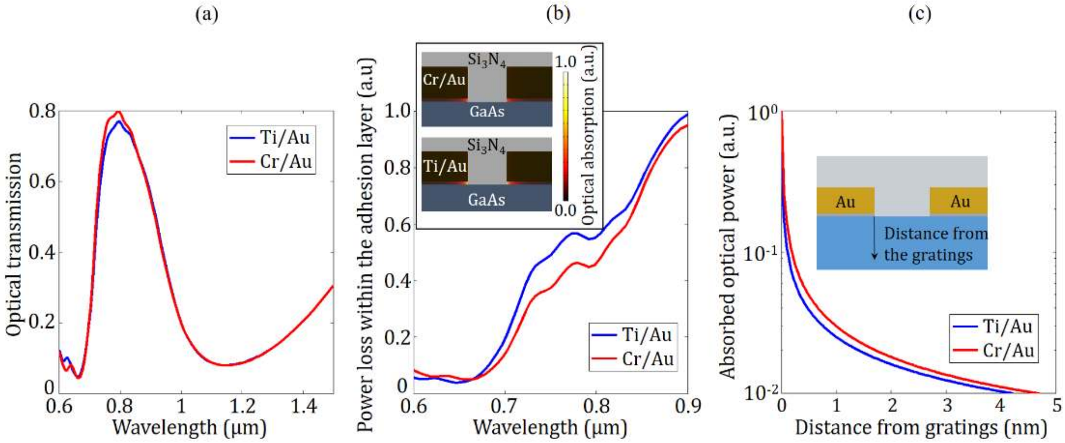

Fig. 4.3, (a), Optical transmission spectra of the Ti/Au and Cr/Au plasmonic gratings. **(b)** Optical power lost within the Ti and Cr layers in both cases. **(c),** Absorbed optical power near the gratings for both grating metallization schemes.

Because of the described reasons, more photocarriers are expected to be generated near the contact electrodes in the Cr/Au plasmonic sources than in the Ti/Au plasmonic sources. Moreover, these photocarriers will encounter a lower energy barrier when drifting to the terahertz radiating elements. Therefore, higher terahertz radiation power levels are expected from the Cr/Au plasmonic photoconductive sources.

To demonstrate the superiority of the Cr adhesion layer, identical plasmonic photoconductive sources with Cr/Au and Ti/Au plasmonic contact electrodes are fabricated on the same SI-GaAs substrate. Both sources have a 1 × 1 mm^2 active area. First, the designed plasmonic contact electrodes are patterned using electron-beam lithography, followed by 5/45 nm Ti/Au and Cr/Au deposition and liftoff. Next, the bias lines and contact pads are patterned using optical lithography followed by 60/540 nm Ti/Au deposition and liftoff. A 320 nm Si_3N_4 antireflection coating layer is deposited via plasma-enhanced chemical vapor deposition, and a 10/90 nm Ti/Au shadow metal layer is deposited on top of the Si_3N_4 layer. Finally, the Si_3N_4 on the contact pads are etched using reactive ion etching. Scanning electron microscopy (SEM) images of a fabricated device are shown in Fig. 4.4.

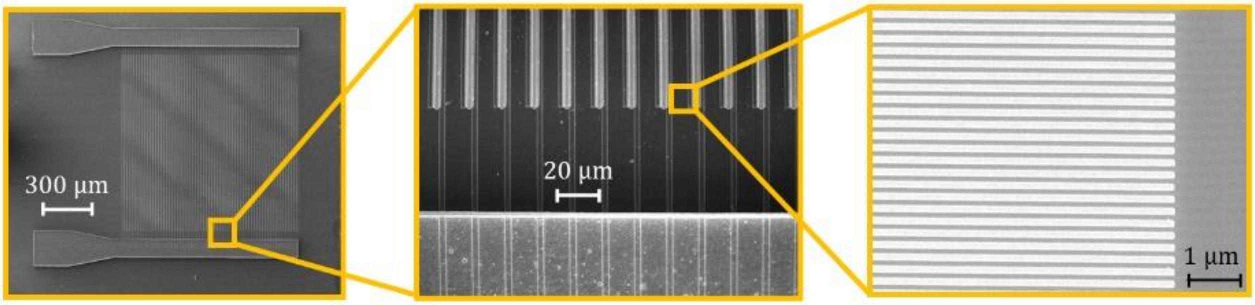

Fig. 4.4, Scanning electron microscopy images of a fabricated plasmonic photoconductive sources.

4.3. Experimental Results and Discussion

The radiation performance of the plasmonic photoconductive sources are characterized using a Ti:sapphire mode-locked laser that generates optical pulses at a 76 MHz repetition rate, 780 nm center wavelength, and 135 fs pulse width. The generated terahertz radiation is measured using a pyroelectric detector (THz30 from APE America) calibrated by Physikalisch-Technische Bundesanstalt (PTB), Germany. The measured photocurrent and radiation power of the sources with two different Au adhesion layers are shown in Fig. 4.5a and Fig. 4.5b, respectively. Higher photocurrent levels are induced when using Cr/Au plasmonic contact electrodes at bias voltages below 12 V. This is because of the lower energy barrier height at the Cr/GaAs interface and the stronger optical absorption in close proximity to the Cr/Au plasmonic contact electrodes. This trend changes at bias voltages above 12 V, where higher photocurrent levels are induced in the Ti/Au device. This change is attributed to excessive heating in the Ti/Au junction due to the high optical absorption within the Ti adhesion layer. This excessive heating increases the average device current, but it does not impact the ultrafast photocurrent that feeds the plasmonic contact electrodes considerably. Therefore, significantly higher terahertz radiation power levels are generated using Cr/Au plasmonic contact electrodes, even at bias voltages above 12 V.

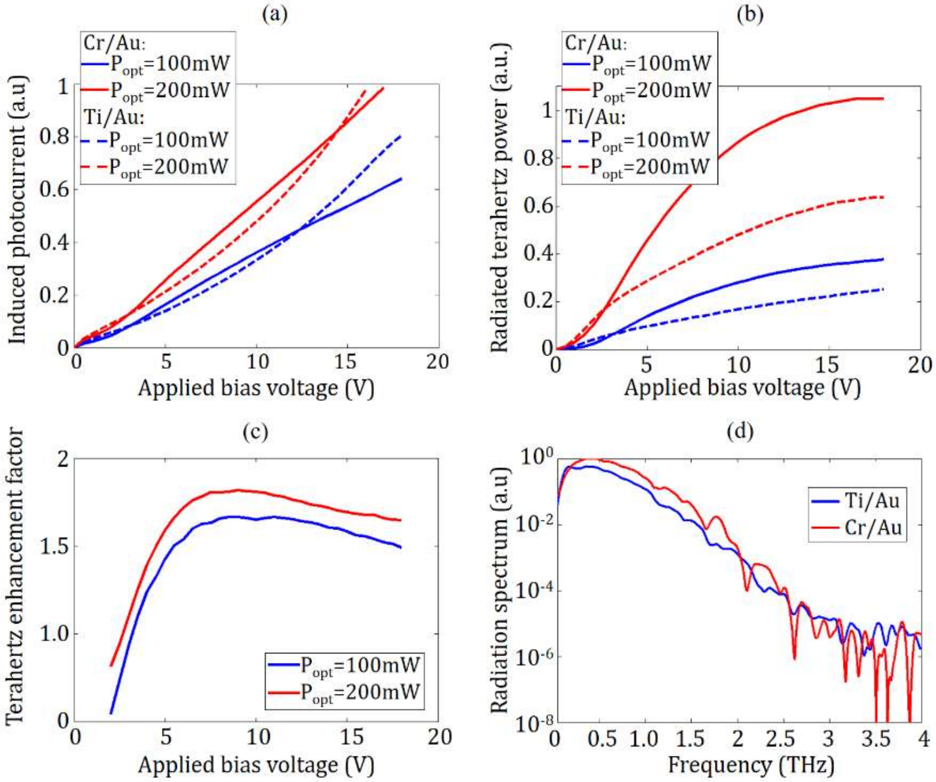

Fig. 4.5, The measured photocurrent **(a)** and radiation power **(b)** of the fabricated plasmonic photoconductive sources with different Au adhesion layers under different optical pump powers. **(c)** The ratio between the terahertz radiation power of the plasmonic photoconductive sources with Cr/Au and Ti/Au contact electrodes. **(d)** The measured radiation spectra of the fabricated plasmonic photoconductive sources with different Au adhesion layers at an optical pump power of 200 mW.

Figure 4.5c shows the ratio between the terahertz radiation power of the plasmonic photoconductive sources with Cr/Au and Ti/Au contact electrodes. The results show up to 80% enhancement in the terahertz radiation power when using the Cr/Au contact electrodes, compared to the Ti/Au contact electrodes used in the existing plasmonic photoconductive terahertz sources. The radiation spectra of the plasmonic photoconductive sources, which are measured using a time-domain terahertz spectroscopy setup, show that this power enhancement factor is maintained over the entire radiation frequency range of 0.1 - 4 THz (Fig. 4.5d).

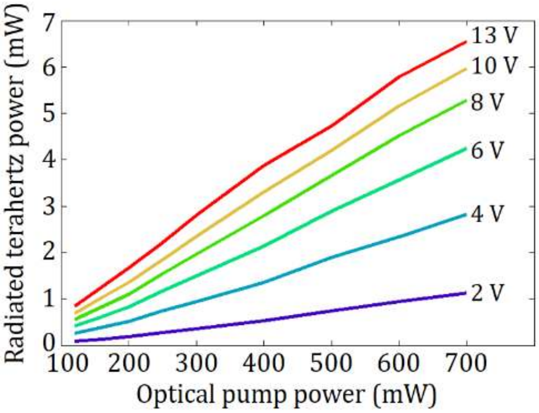

Fig. 4.6, The measured terahertz radiation power of the Cr/Au plasmonic photoconductive source under different optical pump powers and bias voltages.

Figure 4.6 shows the terahertz radiation power of the Cr/Au plasmonic photoconductive source under higher optical pump powers. Using a 700 mW optical pump, 6.7 mW of terahertz power is obtained, which is the highest radiated power reported from a photoconductive source.

In summary, the impact of the Au adhesion layer on the performance of plasmonic photoconductive sources is studied theoretically and experimentally. The results suggest that Cr is the most suitable adhesion layer with superior electrical and optical properties compared to Ti, which is used in the existing plasmonic photoconductive terahertz sources. The superior performance is anticipated because electrons encounter a lower energy barrier at the Cr/Au junction, and the pump photons experience a lower attenuation in the Cr layer. The measurement results show that the plasmonic photoconductive sources with Cr/Au contacts radiate up to 80% higher terahertz power levels, which is in agreement with the theoretical predictions. A record-high radiation power of up to 6.7 mW is achieved at a 700 mW optical pump power.

Chapter 5: Conclusion

This dissertation has aimed to introduce new functionalities of plasmonic nanoantennas for the generation and detection of terahertz waves. A significant part of this dissertation is devoted to the introduction of a novel passive optical-to-terahertz conversion technique through plasmon-coupled surface states. The huge enhancement in wavelength conversion efficiency offered by the plasmon-coupled surface states significantly reduces the required optical power budget, enabling operation in compact and miniaturized system platforms that are not possible for nonlinear optical systems. As an example, the demonstrated fiber-coupled nanoantenna chip sitting at a tip of a fiber (Fig. 2.15a) can be easily integrated with an endoscopy probe for in-vivo terahertz imaging and spectroscopy. To achieve the same terahertz power levels through nonlinear optical processes, 4-orders of magnitude higher optical power is required, which cannot be supported by optical fibers. In addition, plasmon-coupled surface states allow passive wavelength conversion through materials that do not support many of the nonlinear optical processes. For example, semiconductor lattices that possess axial symmetry (e.g. silicon and germanium) cannot provide second-order nonlinearity. However, wavelength conversion in these materials is possible by the use of plasmon-coupled surface states, opening up opportunities for new sensing, imaging, communication, and computation platforms compatible with standard integrated circuit technologies. Moreover, unlike the bulky and complex nonlinear optical setups that require high-energy lasers, tight optical focus, and/or tilted beam to provide high optical pump intensity and phase matching for efficient wavelength conversion, wavelength conversion through plasmon-coupled surface states does not require a complex optical setup and is not sensitive to optical focus and alignment, extending the scope of its potential use for many practical applications. Furthermore, plasmon-coupled surface states allow passive wavelength conversion using nanoantenna arrays, which can manipulate the spatial, spectral, and polarization state of the generated electromagnetic waves, which are not possible by other passive wavelength conversion techniques (nonlinear optical processes, spintronics, photo-Dember effect).

The wavelength conversion efficiency can be further enhanced by boosting the built-in electric field at the semiconductor surface and increasing the spatial overlap between the built-in electric field and photoabsorption profiles. Using alternative semiconductors with a larger number of surface states above the conduction band, introducing higher p-type doping levels, and incorporating a gradient composition semiconductor ($In_{1-x}Ga_xAs$ with x increasing as a function of depth in the substrate) would introduce a steeper band-bending at the semiconductor surface and, therefore, would further enhance the built-in electric field. In addition, by growing the semiconductor active layer on a distributed Bragg reflector and further optimization of the nanoantenna geometry, most of the excited surface plasmons would be trapped in the semiconductor active layer and, therefore, a much stronger spatial overlap between the built-in electric field and photoabsorption profiles can be achieved.

A high-sensitivity terahertz detector optimized for operation with high power Ytterbium (Yb)-doped femtosecond fiber lasers at ~1 µm wavelength range is also introduced in this dissertation. The presented detector is an integral component for developing high dynamic range THz-TDS systems operating at ~1 µm wavelength range.

Finally, the impact of the metal adhesion layer on the terahertz radiation power of plasmonic photoconductive terahertz sources is investigated. It is shown that choosing the correct metal adhesion layer with optimized electrical and optical properties can enhance the radiated terahertz power up to 80%.

Bibliography

[1] D. M. Mittleman, “Perspective: Terahertz science and technology,” *J. Appl. Phys.*, vol. 122, no. 23, (2017).

[2] A. W. M. Lee, S. Kumar, B. S. Williams, Q. Hu, and J. L. Reno, “Real-time imaging using a 4.3-THz quantum cascade laser and a 240×320 element focal-plane array,” *IEEE Photonics Technol. Lett.*, vol. 18, no. 13, pp. 1415–1417, (2006).

[3] N. Vieweg *et al.*, “Terahertz-time domain spectrometer with 90 dB peak dynamic range,” *J. Infrared, Millimeter, Terahertz Waves*, vol. 35, no. 10, pp. 823–832, (2014).

[4] M. Kato, S. R. Tripathi, K. Murate, K. Imayama, and K. Kawase, “Non-destructive drug inspection in covering materials using a terahertz spectral imaging system with injection-seeded terahertz parametric generation and detection,” *Opt. Express*, vol. 24, no. 6, pp. 6425–6432, (2016).

[5] K. Kawase, Y. Ogawa, and Y. Watanabe, “Non-destructive terahertz imaging of illicit drugs using spectral fingerprints,” *Optics Express,* vol. 11, no. 20, pp. 2549–2554, (2003).

[6] J. F. Federici *et al.*, “THz imaging and sensing for security applications - explosives, weapons and drugs,” *Semicond. Sci. Technol.*, vol. 20, p. S266, (2005).

[7] W. L. Chan *et al.*, “THz imaging and sensing for security applications - explosives, weapons and drugs,” *Appl. Phys. Lett.*, vol. 7, no. 1, pp. 1–4, (2007).

[8] R. M. Woodward *et al.*, “Terahertz pulse imaging of ex vivo basal cell carcinoma,” *J. Invest. Dermatol.*, vol. 120, no. 1, pp. 72–78, (2003).

[9] S. S. Dhillon *et al.*, "The 2017 terahertz science and technology roadmap," *J. Phys. D. Appl. Phys.*, vol. 50, no. 043001, (2017).

[10] D. N. Basov, R. D. Averitt, D. Van Der Marel, M. Dressel, and K. Haule, "Electrodynamics of correlated electron materials," *Rev. Mod. Phys.*, vol. 83, no. 2, pp. 471–541, (2011).

[11] N. Wang, S. Cakmakyapan, Y. J. Lin, H. Javadi, and M. Jarrahi, "Room-temperature heterodyne terahertz detection with quantum-level sensitivity," *Nat. Astron.*, vol. 3, pp. 977–982, (2019).

[12] P. Hartogh *et al.*, "Ocean-like water in the Jupiter-family comet 103P/Hartley 2," *Nature*, vol. 478, no. 7368, pp. 218–220, (2011).

[13] M. Van Exter and D. R. Grischkowsky, "Characterization of an Optoelectronic Terahertz Beam System," *IEEE Trans. Microw. Theory Tech.*, vol. 38, no. 11, pp. 1684–1691, (1990).

[14] P. R. Smith and D. H. Auston, "Subpicosecond Photoconducting Dipole Antennas," *IEEE J. Quantum Electron.*, vol. 24, no. 2, pp. 255–260, (1988).

[15] T. Yasui, E. Saneyoshi, and T. Araki, "Asynchronous optical sampling terahertz time-domain spectroscopy for ultrahigh spectral resolution and rapid data acquisition," *Appl. Phys. Lett.*, vol. 87, no. 6, pp. 1–3, (2005).

[16] M. Yahyapour *et al.*, "Fastest thickness measurements with a Terahertz time-domain system based on electronically controlled optical sampling," *Appl. Sci.*, vol. 9, no. 7, (2019).

[17] J. Takayanagi *et al.*, "High-resolution time-of-flight terahertz tomography using a femtosecond fiber laser," *Opt. Express*, vol. 17, no. 9, p. 7533, (2009).

[18] W. R. Huang *et al.*, "Highly efficient terahertz pulse generation by optical rectification in

stoichiometric and cryo-cooled congruent lithium niobate," *J. Mod. Opt.*, vol. 62, no. 18, pp. 1486–1493, (2015).

[19] J. A. Fülöp *et al.*, "Generation of sub-mJ terahertz pulses by optical rectification," *Opt. Lett.*, vol. 37, no. 4, pp. 557–559, (2012).

[20] C. P. Hauri, C. Ruchert, C. Vicario, and F. Ardana, "Strong-field single-cycle THz pulses generated in an organic crystal," *Appl. Phys. Lett.*, vol. 99, 161116 , (2011).

[21] C. Ruchert, C. Vicario, and C. P. Hauri, "Scaling submillimeter single-cycle transients toward megavolts per centimeter field strength via optical rectification in the organic crystal OH1," *Opt. Lett.*, vol. 37, no. 5, pp. 899–901, (2012).

[22] P. Gu, M. Tani, S. Kono, K. Sakai, and X. C. Zhang, "Study of terahertz radiation from InAs and InSb," *J. Appl. Phys.*, vol. 91, no. 9, pp. 5533–5537, (2002).

[23] K. Liu, J. Xu, T. Yuan, and X. C. Zhang, "Terahertz radiation from InAs induced by carrier diffusion and drift," *Phys. Rev. B*, vol. 73, no. 15, p. 155330, (2006).

[24] M. B. Johnston *et al.*, "Generation of high-power terahertz pulses in a prism," *Opt. Lett.*, vol. 27, no. 21, pp. 1935–1937, (2002).

[25] M. L. Smith, R. Mendis, R. E. M. Vickers, and R. A. Lewis, "Comparison of photoexcited p-InAs THz radiation source with conventional thermal radiation sources," *J. Appl. Phys.*, vol. 105, p. 063109, (2009).

[26] M. Reid and R. Fedosejevs, "Quantitative comparison of terahertz emission from (100) InAs surfaces and a GaAs large-aperture photoconductive switch at high fluences," *Appl. Opt.*, vol. 44, no. 1, pp. 149–153, (2005).

[27] G. Klatt *et al.*, “Photo-Dember terahertz emitter excited with an Er:fiber laser,” *Appl. Phys. Lett.*, vol. 98, p. 021114, (2011).

[28] T. Seifert *et al.*, “Efficient metallic spintronic emitters of ultrabroadband terahertz radiation,” *Nat. Photonics*, vol. 10, pp. 483–488, (2016).

[29] U. Nandi *et al.*, “Antenna-coupled spintronic terahertz emitters driven by a 1550 nm femtosecond laser oscillator,” *Appl. Phys. Lett.*, vol. 115, no. 2, p. 022405, (2019).

[30] T. Seifert *et al.*, “Ultrabroadband single-cycle terahertz pulses with peak fields of 300 kV cm-1 from a metallic spintronic emitter,” *Appl. Phys. Lett.*, vol. 110, no. 25, p. 252402, (2017).

[31] D. Yang *et al.*, “Powerful and Tunable THz Emitters Based on the Fe/Pt Magnetic Heterostructure,” *Adv. Opt. Mater.*, vol. 4, no. 12, pp. 1944–1949, (2016).

[32] E. Castro-Camus, L. Fu, J. Lloyd-Hughes, H. H. Tan, C. Jagadish, and M. B. Johnston, “Photoconductive response correction for detectors of terahertz radiation,” *J. Appl. Phys.*, vol. 104, no. 053113, (2008).

[33] X. C. Zhang, P. U. Jepsen, R. H. Jacobsen, and S. R. Keiding, “Generation and detection of terahertz pulses from biased semiconductor antennas,” *J. Opt. Soc. Am. B*, vol. 13, no. 11, p. 2424, (1996).

[34] S. Kono, M. Tani, P. Gu, and K. Sakai, “Detection of up to 20 THz with a low-temperature-grown GaAs photoconductive antenna gated with 15 fs light pulses,” *Appl. Phys. Lett.*, vol. 77, no. 25, pp. 4104–4106, (2000).

[35] X. Liu, A. Prasad, J. Nishio, E. R. Weber, Z. Liliental-Weber, and W. Walukiewicz, “Native

point defects in low-temperature- grown GaAs," vol. 67, p. 279, (1995).

[36] C. Baker *et al.*, "Terahertz pulsed imaging with 1.06 μm laser excitation," *Appl. Phys. Lett.*, vol. 83, p. 4113, (2003).

[37] A. Takazato, M. Kamakura, T. Matsui, J. Kitagawa, and Y. Kadoya, "Detection of terahertz waves using low-temperature-grown InGaAs with 1.56 μm pulse excitation," *Appl. Phys. Lett.*, vol. 90, p. 10119, (2007).

[38] R. J. B. B. Dietz *et al.*, "64 μW pulsed terahertz emission from growth optimized InGaAs/InAlAs heterostructures with separated photoconductive and trapping regions," *Appl. Phys. Lett.*, vol. 103, p. 061103, (2013).

[39] R. J. B. B. Dietz, B. Globisch, H. Roehle, D. Stanze, T. Göbel, and M. Schell, "Influence and adjustment of carrier lifetimes in InGaAs/InAlAs photoconductive pulsed terahertz detectors: 6 THz bandwidth and 90dB dynamic range," *Opt. Express*, vol. 22, no. 16, p. 19411, (2014).

[40] R. Salas *et al.*, "Growth and properties of rare-earth arsenide InGaAs nanocomposites for terahertz generation," *Appl. Phys. Lett.*, vol. 106, p. 081103, (2015).

[41] S. Preu, M. Mittendorff, H. Lu, H. B. Weber, S. Winnerl, and A. C. Gossard, "1550 nm ErAs:In(Al)GaAs large area photoconductive emitters," *Appl. Phys. Lett.*, vol. 101, p. 101105, (2012).

[42] U. Nandi, J. C. Norman, A. C. Gossard, H. Lu, and S. Preu, "1550-nm Driven ErAs:In(Al)GaAs Photoconductor-Based Terahertz Time Domain System with 6.5 THz Bandwidth," *J. Infrared, Millimeter, Terahertz Waves*, vol. 39, no. 4, pp. 340–348, (2018).

[43] C. D. Wood *et al.*, "Terahertz emission from metal-organic chemical vapor deposition grown Fe:InGaAs using 830 nm to 1.55 µm excitation," *Appl. Phys. Lett.*, vol. 96, p. 194104, (2010).

[44] M. Suzuki and M. Tonouchi, "Fe-implanted InGaAs terahertz emitters for 1.56 µm wavelength excitation," *Appl. Phys. Lett.*, vol. 86, p. 051104, (2005).

[45] C. W. Berry, M. R. Hashemi, S. Preu, H. Lu, A. C. Gossard, and M. Jarrahi, "High power terahertz generation using 1550nm plasmonic photomixers," *Appl. Phys. Lett.*, vol. 105, p. 011121, (2014).

[46] S. H. Yang, M. R. Hashemi, C. W. Berry, and M. Jarrahi, "7.5% Optical-to-terahertz conversion efficiency offered by photoconductive emitters with three-dimensional plasmonic contact electrodes," *IEEE Trans. Terahertz Sci. Technol.*, vol. 4, no. 5, pp. 575–581, (2014).

[47] C. W. Berry, N. Wang, M. R. Hashemi, M. Unlu, and M. Jarrahi, "Significant performance enhancement in photoconductive terahertz optoelectronics by incorporating plasmonic contact electrodes.," *Nat. Commun.*, vol. 4, p. 1622, (2013).

[48] S.-H. Yang *et al.*, "Tunable terahertz wave generation through a bimodal laser diode and plasmonic photomixer," *Opt. Express*, vol. 23, no. 24, p. 31206, (2015).

[49] N. T. Yardimci, S. Cakmakyapan, S. Hemmati, and M. Jarrahi, "A High-Power Broadband Terahertz Source Enabled by Three- Dimensional Light Confinement in a Plasmonic Nanocavity," *Sci. Rep.*, vol. 7, p. 4166, (2017).

[50] N. T. Yardimci, S. H. Yang, C. W. Berry, and M. Jarrahi, "High-power terahertz generation

using large-area plasmonic photoconductive emitters," *IEEE Trans. Terahertz Sci. Technol.*, vol. 5, no. 2, pp. 223–229, (2015).

[51] C. W. Berry, M. R. Hashemi, S. Preu, H. Lu, A. C. Gossard, and M. Jarrahi, "Plasmonics enhanced photomixing for generating quasi-continuous-wave frequency-tunable terahertz radiation," *Opt. Lett.*, vol. 39, no. 15, p. 4522, (2014).

[52] N. T. Yardimci and M. Jarrahi, "High Sensitivity Terahertz Detection through Large-Area Plasmonic Nano-Antenna Arrays," *Sci. Rep.*, vol. 7, p. 42667, (2017).

[53] N. T. Yardimci, D. Turan, S. Cakmakyapan, and M. Jarrahi, "A high-responsivity and broadband photoconductive terahertz detector based on a plasmonic nanocavity," *Appl. Phys. Lett.*, vol. 113, p. 251102, (2018).

[54] U. Nandi *et al.*, "ErAs : In(Al)GaAs photoconductor-based time domain system with 4.5 THz single shot bandwidth and emitted terahertz power of 164 µW," *Opt. Lett.*, vol. 45, no. 10, pp. 2812–2815, (2020).

[55] B. Globisch *et al.*, "Iron doped InGaAs: Competitive THz emitters and detectors fabricated from the same photoconductor," *J. Appl. Phys.*, vol. 121, no. 5, (2017).

[56] E. R. Brown, D. C. Driscoll, and A. C. Gossard, "State-of-the-art in 1.55 νm ultrafast InGaAs photoconductors, and the use of signal-processing techniques to extract the photocarrier lifetime," *Semicond. Sci. Technol.*, vol. 20, no. 7, (2005).

[57] B. Globisch *et al.*, "Absolute terahertz power measurement of a time-domain spectroscopy system," *Opt. Lett.*, vol. 40, no. 15, p. 3544, (2015).

[58] A. Mingardi, W.-D. Zhang, E. R. Brown, A. D. Feldman, T. E. Harvey, and R. P. Mirin,

"High power generation of THz from 1550-nm photoconductive emitters," *Opt. Express*, vol. 26, no. 11, p. 14472, (2018).

[59] R. J. B. Dietz *et al.*, "64 µw pulsed terahertz emission from growth optimized InGaAs/InAlAs heterostructures with separated photoconductive and trapping regions," *Appl. Phys. Lett.*, vol. 103, no. 6, pp. 1–5, (2013).

[60] H. Roehle *et al.*, "Next generation 15 µm terahertz antennas: mesa-structuring of InGaAs/InAlAs photoconductive layers," *Opt. Express*, vol. 18, no. 3, p. 2296, (2010).

[61] D. Turan, N. T. Yardimci, and M. Jarrahi, "Plasmonics-enhanced photoconductive terahertz detector pumped by Ytterbium-doped fiber laser," *Opt. Express*, vol. 28, no. 3, p. 3835, (2020).

[62] D. Turan, S. C. Corzo-Garcia, N. T. Yardimci, E. Castro-Camus, and M. Jarrahi, "Impact of the Metal Adhesion Layer on the Radiation Power of Plasmonic Photoconductive Terahertz Sources," *J. Infrared, Millimeter, Terahertz Waves*, vol. 38, no. 12, pp. 1448–1456, (2017).

[63] W. Mönch, "On the physics of metal-semiconductor interfaces," *Reports Prog. Phys.*, vol. 53, pp. 221–278, (1990).

[64] J. Tersoff, "Schottky barriers and semiconductor band structures," *Phys. Rev. B*, vol. 32, no. 10, pp. 6968–6971, (1985).

[65] L. F. J. Piper, T. D. Veal, M. J. Lowe, and C. F. McConville, "Electron depletion at InAs free surfaces: Doping-induced acceptorlike gap states," *Phys. Rev. B*, vol. 73, p. 195321, (2006).

[66] W. Mönch, *Semiconductor Surfaces and Interfaces*. Berlin Heidelberg: Springer-Verlag, (1993).

[67] R. Adomavičius, A. Urbanowicz, G. Molis, A. Krotkus, and E. Šatkovskis, "Terahertz emission from p-lnAs due to the instantaneous polarization," *Appl. Phys. Lett.*, vol. 85, no. 13, p. 2463, (2004).

[68] M. B. Johnston, D. M. Whittaker, A. Corchia, A. G. Davies, and E. H. Linfield, "Simulation of terahertz generation at semiconductor surfaces," *Phys. Rev. B*, vol. 65, no. 16, p. 165301, (2002).

[69] M. Tonouchi, "Simplified formulas for the generation of terahertz waves from semiconductor surfaces excited with a femtosecond laser," *J. Appl. Phys.*, vol. 127, no. 24, p. 245703, (2020).

[70] Y. J. Lu *et al.*, "Plasmonic nanolaser using epitaxially grown silver film," *Science*, vol. 337, pp. 450–454, (2012).

[71] R. A. Pala, J. White, E. Barnard, J. Liu, and M. L. Brongersma, "Design of plasmonic thin-film solar cells with broadband absorption enhancements," *Adv. Mater.*, vol. 21, pp. 3504–3509, (2009).

[72] E. Cubukcu, E. A. Kort, K. B. Crozier, and F. Capasso, "Plasmonic laser antenna," *Appl. Phys. Lett.*, vol. 89, p. 093120, (2006).

[73] H. A. Atwater and A. Polman, "Plasmonics for improved photovoltaic devices," *Nat. Mater.*, vol. 9, pp. 205–213, (2010).

[74] J. A. Schuller, E. S. Barnard, W. Cai, Y. C. Jun, J. S. White, and M. L. Brongersma,

"Plasmonics for extreme light concentration and manipulation," *Nat. Mater.*, vol. 9, pp. 193–204, (2010).

[75] M. L. Brongersma, N. J. Halas, and P. Nordlander, "Plasmon-induced hot carrier science and technology," *Nat. Nanotechnol.*, vol. 10, pp. 25–34, (2015).

[76] M. W. Knight, H. Sobhani, P. Nordlander, and N. J. Halas, "Photodetection with active optical antennas," *Science*, vol. 332, no. 6030, pp. 702–704, (2011).

[77] A. R. Rastinehad *et al.*, "Gold nanoshell-localized photothermal ablation of prostate tumors in a clinical pilot device study," *Proc. Natl. Acad. Sci. U. S. A.*, vol. 116, no. 37, pp. 18590–18596, (2019).

[78] U. Aslam, S. Chavez, and S. Linic, "Controlling energy flow in multimetallic nanostructures for plasmonic catalysis," *Nat. Nanotechnol.*, vol. 12, pp. 1000–1005, (2017).

[79] R. F. Oulton *et al.*, "Plasmon lasers at deep subwavelength scale," *Nature*, vol. 461, no. 7264, pp. 629–632, (2009).

[80] M. A. Noginov *et al.*, "Demonstration of a spaser-based nanolaser," *Nature*, vol. 460, pp. 1110–1112, (2009).

[81] G. Satyanadh, R. P. Joshi, N. Abedin, and U. Singh, "Monte Carlo calculation of electron drift characteristics and avalanche noise in bulk InAs," *J. Appl. Phys.*, vol. 91, no. 3, pp. 1331–1338, (2002).

[82] K. Brennan and K. Hess, "High field transport in GaAs, InP and InAs," *Solid State Electron.*, vol. 27, no. 4, pp. 347–357, (1984).

[83] S. Kalem, J. I. Chyi, H. Morkoç, R. Bean, and K. Zanio, "Growth and transport properties

of InAs epilayers on GaAs," *Appl. Phys. Lett.*, vol. 53, no. 17, pp. 1647–1649, (1988).

[84] C. Balanis, *Antenna Theory; Analysis and Design*, 3rd Ed. Hoboken, NJ: John Wiley & Sons Inc, (2005).

[85] A. G. Stepanov, L. Bonacina, S. V. Chekalin, and J.-P. Wolf, "Generation of 30 μJ single-cycle terahertz pulses at 100 Hz repetition rate by optical rectification," *Opt. Lett.*, vol. 33, no. 21, pp. 2497–2499, (2008).

[86] H. Hirori, A. Doi, F. Blanchard, and K. Tanaka, "Single-cycle terahertz pulses with amplitudes exceeding 1 MV/cm generated by optical rectification in $LiNbO_3$," *Appl. Phys. Lett.*, vol. 98, p. 091106, (2011).

[87] J. A. Fülöp *et al.*, "Efficient generation of THz pulses with 0.4 mJ energy," *Opt. Express*, vol. 22, no. 17, pp. 20155–20163, (2014).

[88] F. Blanchard *et al.*, "Effect of extreme pump pulse reshaping on intense terahertz emission in lithium niobate at multimilliJoule pump energies," *Opt. Lett.*, vol. 39, no. 15, pp. 4333–4336, (2014).

[89] C. Ruchert, C. Vicario, and C. P. Hauri, "Spatiotemporal focusing dynamics of intense supercontinuum THz pulses," *Phys. Rev. Lett.*, vol. 110, p. 123902, (2013).

[90] X. Wu *et al.*, "Highly efficient generation of 0.2 mJ terahertz pulses in lithium niobate at room temperature with sub-50 fs chirped Ti:sapphire laser pulses," *Opt. Express*, vol. 26, no. 6, pp. 7107–7116, (2018).

[91] C. Vicario, A. V. Ovchinnikov, S. I. Ashitkov, M. B. Agranat, and C. P. Hauri, "Generation of 0.9-mJ THz pulses in DSTMS pumped by a Cr:Mg2 SiO_4 laser," *Opt. Lett.*, vol. 39, no.

23, pp. 6632–6635, (2014).

[92] A. Rovere *et al.*, “Generation of high-field terahertz pulses in an HMQ-TMS organic crystal pumped by an ytterbium laser at 1030 nm,” *Opt. Express*, vol. 26, no. 3, p. 3, (2018).

[93] J. Lu *et al.*, “Efficient terahertz generation in highly nonlinear organic crystal HMB-TMS,” *Opt. Express*, vol. 26, no. 23, p. 23, (2018).

[94] A. G. Stepanov, J. Hebling, and J. Kuhl, “Efficient generation of subpicosecond terahertz radiation by phase-matched optical rectification using ultrashort laser pulses with tilted pulse fronts,” *Appl. Phys. Lett.*, vol. 83, p. 3000, (2003).

[95] A. G. Stepanov, J. Kuhl, I. Z. Kozma, E. Riedle, G. Almási, and J. Hebling, “Scaling up the energy of THz pulses created by optical rectification,” *Opt. Express*, vol. 13, no. 15, p. 15, (2005).

[96] F. D. J. Brunner, O.-P. Kwon, S.-J. Kwon, M. Jazbinšek, A. Schneider, and P. Günter, “A hydrogen-bonded organic nonlinear optical crystal for high-efficiency terahertz generation and detection,” *Opt. Express*, vol. 16, no. 21, pp. 16496–16508, (2008).

[97] M. C. Hoffmann, K.-L. Yeh, J. Hebling, and K. A. Nelson, “Efficient terahertz generation by optical rectification at 1035 nm,” *Opt. Express*, vol. 15, no. 18, pp. 11706–11713, (2007).

[98] K. L. Yeh, M. C. Hoffmann, J. Hebling, and K. A. Nelson, “Generation of 10 μJ ultrashort terahertz pulses by optical rectification,” *Appl. Phys. Lett.*, vol. 90, p. 171121, (2007).

[99] F. Blanchard *et al.*, “Generation of 1.5 μJ single-cycle terahertz pulses by optical rectification from a large aperture ZnTe crystal,” *Opt. Express*, vol. 15, no. 20, pp. 13212–13220, (2007).

[100] G. Chang, C. J. Divin, C. H. Liu, S. L. Williamson, A. Galvanauskas, and T. B. Norris, "Power scalable compact THz system based on an ultrafast Yb-doped fiber amplifier," *Opt. Express*, vol. 14, no. 17, pp. 7909–7913, (2006).

[101] M. Jewariya, M. Nagai, and K. Tanaka, "Enhancement of terahertz wave generation by cascaded χ^2 processes in $LiNbO_3$," *J. Opt. Soc. Am. B*, vol. 26, no. 9, pp. A101–A106, (2009).

[102] I. E. Gordon *et al.*, "The HITRAN2016 molecular spectroscopic database," *J. Quant. Spectrosc. Radiat. Transf.*, vol. 203, pp. 3–69, (2017).

[103] G. Matthäus *et al.*, "Surface-emitted THz generation using a compact ultrashort pulse fiber amplifier at 1060 nm," *Opt. Commun.*, vol. 261, pp. 114–117, (2006).

[104] V. Pačebutas *et al.*, "Terahertz time-domain-spectroscopy system based on femtosecond Yb:fiber laser and GaBiAs photoconducting components," *Appl. Phys. Lett.*, vol. 97, p. 031111, (2010).

[105] V. Pačebutas, A. Bičiūnas, K. Bertulis, and A. Krotkus, "Optoelectronic terahertz radiation system based on femtosecond 1um laser pulses and GaBiAs detector," *Electron. Lett.*, vol. 44, no. 19, (2008).

[106] M. S. Kong *et al.*, "Terahertz radiation using log-spiral-based low-temperature-grown InGaAs photoconductive antenna pumped by mode-locked Yb-doped fiber laser," *Opt. Express*, vol. 24, no. 7, pp. 10095–10100, (2016).

[107] G. Matthäus *et al.*, "Intracavity terahertz generation inside a high-energy ultrafast soliton fiber laser," *Appl. Phys. Lett.*, vol. 93, p. 261105, (2008).

[108] R. J. B. Dietz *et al.*, "Low temperature grown photoconductive antennas for pulsed 1060 nm excitation: Influence of excess energy on the electron relaxation," *J. Infrared, Millimeter, Terahertz Waves*, vol. 36, no. 1, pp. 60–71, (2015).

[109] R. J. B. Dietz *et al.*, "Low temperature grown Be-doped InGaAs/InAlAs photoconductive antennas excited at 1030 nm," *J. Infrared, Millimeter, Terahertz Waves*, vol. 34, no. 3–4, pp. 231–237, (2013).

[110] R. E. Nahory, M. A. Pollack, W. D. Johnston, and R. L. Barns, "Band gap versus composition and demonstration of Vegard's law for $In_{1-x}Ga_xAs_yP_{1-y}$ lattice matched to InP," *Appl. Phys. Lett.*, vol. 33, no. 7, pp. 659–661, (1978).

[111] B. Y. Hsieh and M. Jarrahi, "Analysis of periodic metallic nano-slits for efficient interaction of terahertz and optical waves at nano-scale dimensions," *J. Appl. Phys.*, vol. 109, no. 084326, (2011).

[112] N. T. Yardimci, H. Lu, and M. Jarrahi, "High power telecommunication-compatible photoconductive terahertz emitters based on plasmonic nano-antenna arrays," *Appl. Phys. Lett.*, vol. 109, p. 191103, (2016).

[113] N. T. Yardimci, R. Salas, E. M. Krivoy, H. P. Nair, S. R. Bank, and M. Jarrahi, "Impact of substrate characteristics on performance of large area plasmonic photoconductive emitters," *Opt. Express*, vol. 23, no. 25, pp. 32035–32043, (2015).

[114] N. T. Yardimci and M. Jarrahi, "Nanostructure-Enhanced Photoconductive Terahertz Emission and Detection," *Small*, vol. 14, no. 1802437, pp. 1–14, (2018).

[115] M. Jarrahi, "Advanced Photoconductive Terahertz Optoelectronics Based on Nano-

Antennas and Nano-Plasmonic Light Concentrators," *IEEE Trans. Terahertz Sci. Technol.*, vol. 5, no. 3, pp. 391–397, (2015).

[116] C. W. Berry, M. R. Hashemi, and M. Jarrahi, "Generation of high power pulsed terahertz radiation using a plasmonic photoconductive emitter array with logarithmic spiral antennas," *Appl. Phys. Lett.*, vol. 104, p. 081122, (2014).

[117] C. W. Berry and M. Jarrahi, "Terahertz generation using plasmonic photoconductive gratings," *New J. Phys.*, vol. 14, (2012).

[118] N. Wang and M. Jarrahi, "Noise analysis of photoconductive terahertz detectors," *J. Infrared, Millimeter, Terahertz Waves*, vol. 34, no. 9, pp. 519–528, (2013).

[119] S.-H. Yang and M. Jarrahi, "Spectral characteristics of terahertz radiation from plasmonic photomixers," *Opt. Express*, vol. 23, no. 22, p. 28522, (2015).

[120] A. G. Baca, F. Ren, J. C. Zolper, R. D. Briggs, and S. J. Pearton, "A survey of ohmic contacts to III-V compound semiconductors," *Thin Solid Films*, vol. 308–309, pp. 599–606, (1997).

[121] T. C. Shen, G. B. Gao, and H. Morkoc, "Recent developments in ohmic contacts for III–V compound semiconductors," *J. Vac. Sci. Technol. B Microelectron. Nanom. Struct.*, vol. 10, no. 5, p. 2113, (1992).

[122] V. L. Rideout, "A review of the theory, technology and applications of metal-semiconductor rectifiers," *Thin Solid Films*, vol. 48, no. 3, pp. 261–291, (1978).

[123] M. Murakami, "Development of ohmic contact materials for GaAs integrated circuits," *Mater. Sci. Reports*, vol. 5, no. 5, pp. 273–317, (1990).

[124] G. Y. Robinson and C. W. Wilmsen, *Physics and Chemistry of III-V Compound Semiconductor Interface*. (1985).

[125] E. H. Rhoderick and R. H. Williams, *Metal-Semiconductor Contacts*. (1988).

[126] L. C. Wang, “The Development of Solid Phase Regrowth on GaAs and its Applications,” in *Material Research Society Symposium*, (1994), vol. 319, pp. 93–104.

[127] N. Vieweg *et al.*, “Impact of the contact metallization on the performance of photoconductive THz antennas.,” *Opt. Express*, vol. 16, no. 24, pp. 19695–19705, (2008).

[128] W. Shi, L. Hou, and X. Wang, “High effective terahertz radiation from semi-insulating-GaAs photoconductive antennas with ohmic contact electrodes,” *J. Appl. Phys.*, vol. 110, no. 2, pp. 4–9, (2011).

[129] A. G. Baca and C. I. H. Ashby, *Fabrication of GaAs devices*. IET, (2005).

[130] J. R. Waldrop, “Schottky-barrier height of ideal metal contacts to GaAs,” *J. Vac. Sci. Technol. B*, vol. 2, no. 3, pp. 445–448, (1984).

[131] N. Newman, Z. Liliental-Weber, E. R. Weber, J. Washburn, and W. E. Spicer, “Schottky barrier instabilities due to contamination,” vol. 145, pp. 145–147, (1988).

[132] S.M.Sze and K. K. Ng, *Physics of Semiconductor Devices*, 3rd ed. (2006).

[133] Z. Liliental-Weber, N. Newman, J. Washburn, E. R. Weber, and W. E. Spicer, “Influence of interfacial contamination on the structure and barrier height of Cr/GaAs Schottky contacts,” *Appl. Phys. Lett.*, vol. 54, no. 4, pp. 356–358, (1989).

[134] E. Spicer, W, N. Newman, C. J. Spindt, Z. Liliental-Weber, and E. R. Weber, “““Pinning”” and Fermi level movement at GaAs surfaces and interfaces,” *J. Vac. Sci. Technol. A*, vol.

2084, (1990).

[135] C. E. McCants *et al.*, “Chemical and electrical properties at the annealed Ti/GaAs(110) interface,” *J. Vac. Sci. Technol. A Vacuum, Surfaces, Film.*, vol. 6, no. 3, p. 1466, (1988).